Physics – Uspekhi **55** (8) 741 – 772 (2012)

REVIEWS OF TOPICAL PROBLEMS PACS numbers: 95.55.Vj , 95.85.Bh, 96.50.S –

Radioastronomical measurement of ultrahigh-energy cosmic particle fluxes

A D Filonenko

DOI: 10.3367/UFNe.0182.201208a.0793

Contents

Abstract. The basic principles underlying the radio telescope measurement of ultrahigh-energy particle fluxes are reviewed. Experimental lunar regolith emission data are presented for the 10^{20} eV energy range. Some conclusions from theoretical work are discussed, as is the influence of a number of factors on the intensity of the radio pulse due to the cascade disk under the Moon's surface.

1. Introduction

Methods for the detection of cosmic particles have progressed by huge leaps since the discovery of cosmic radiation by Victor F. Hess (1912). Our understanding of the nature of this phenomenon has also undergone changes that are at least as important. Measuring the rate of discharge of an electrometer mounted on a balloon, Hess observed that the rate of neutralization of the charge increases with increasing the altitude. This was sufficient evidence that the presence of negative and positive ions at high altitudes in the atmosphere is not a consequence of natural radioactivity of the environment but is caused by processes of cosmic origin. The discovery of air showers by Pierre Auger in 1938 was another milestone on the way to understanding the nature of cosmic radiation. Among other things, Auger's discovery implied that particles with the energy sufficient to generate cascades of particles (air showers) penetrate Earth's atmosphere from the surrounding space; nowadays, these showers are known as extensive air showers (EASs). EASs are the cause of the high concentration of ions detected by Hess at altitudes of about 5 km.

Some time later, the first photomultipliers were invented, Cherenkov radiation was discovered, and Cherenkov detectors were designed. The first prototypes of modern EAS facilities were built when it became possible to quickly and reliably process information sent by electronic means from measuring devices. It was then established that the energy

A D Filonenko Dal' East-Ukrainian National University, kvartal Molodezhnyi 20a, 91034 Lugansk, Ukraine
Tel. (064) 250 08 26
E-mail: filonenko_ad@dsip.net

Received 9 September 2011, revised 18 February 2012
Uspekhi Fizicheskikh Nauk **182** (8) 793 – 827 (2012)
DOI: 10.3367/UFNr.0182.201208a.0793
Translated by V Kisin; edited by A M Semikhatov

spectrum of primary cosmic rays has a power-law character, $dN/dE \propto E^{-\gamma}$. And in 1958, Kulikov and Khristiansen found that the spectrum bends in the energy range 10^{15} eV [1], exhibiting the 'elbow' that still stimulates discussions.

In the 1960s, a large BAS setup was already functioning — the Volcano Ranch (New Mexico, USA), 12 km^2 in area; it detected an event with a record high energy, about 10^{20} eV [2]. Later, facilities at Haverah Park (University of Leeds, UK), Yakutsk (Shafer Institute of Space Physics and Aeronomy, SB RAS), Akeno (University of Tokyo, Japan), and some others started operations. These systems mostly used scintillation counters in addition to traditional Geiger–Müller counters. Ultimately, after several unsuccessful attempts, a fluorescence detector, Fly's Eye, was commissioned at the University of Utah (USA) in 1981. It was based on detecting light emitted by nitrogen atoms excited by electrons of a shower [3]. In contrast to Cherenkov radiation, the angular distribution of ionization radiation is isotropic, and hence tilted showers could also be studied. The name of the detector – Fly's Eye – stems from its structure resembling the faceted eye of insects. Very soon, the data collected by this facility reliably confirmed the previously discussed [4] feature of the energy spectrum, which became known as the 'ankle' [5]. This was another bend in the spectrum in the energy region $\sim 3 \times 10^{18}$ eV.

The results of theoretical and experimental work led to a deeply rooted opinion that the origin of cosmic rays with energies of at least $10^{18} - 10^{19}$ eV is extragalactic [6, 7]. Obviously, cosmic rays of maximum interest were those at energies above 10^{20} eV. First, acceleration models could not explain the presence of particles of such a high energy even under the most extreme conditions. Second, cosmic rays with energies above 10^{20} eV could be produced by a process generating a very powerful energy release at high energy density, a process whose internal mechanisms are not yet sufficiently known. Finally, charged particles (mostly protons) with such a high energy are only slightly deflected in magnetic fields, and therefore their direction of travel points to the probable source.

The need for modern astrophysics to measure particle fluxes with energies above 10^{20} eV resulted in the need to update the existing facilities, but it also generated an impetus for developing new detectors with an energy 'ceiling' an order of magnitude greater than in previous systems. It was this factor that stimulated a search for fundamentally new methods required to detect particles with ultrahigh energies (UHEs). In the 1990s, work was started on the Japanese experimental facility AGASA (Akeno Giant Air Shower Array), with an effective area of about 100 km^2 and more than a hundred scintillation counters distributed over this area. The fluorescence detector Fly's Eye also reached this level. The data on the energy spectrum in the range $10^{19} - 10^{20}$ eV appeared contradictory. The intriguing puzzle was connected with the wish to elucidate whether the Greisen–Zatsepin–Kuzmin cutoff (GZK) exists. The main idea of this cutoff is as follows.

In 1966, two papers were published almost simultaneously where the phenomenon called 'CMB cutoff' was derived theoretically [8]. It was shown that regardless of the magnitude of the space proton energy, this energy is inevitably reduced in collisions with the background photons over a path of ~ 50 Mps to the minimum value $E_{GZK} \approx 5 \times 10^{19}$ eV, which was subsequently called the GZK cutoff. This conclusion is based on the fact that the energy of the cosmic microwave background photons in the rest frame of the proton is the threshold in the reaction $p\gamma \to \Delta^* \to N\pi$.

Until recently, the reality of the GZK cutoff remained dubious. The results obtained at the most advanced experimental facilities, AGASA and HiRes (High Resolution Fly's Eye Experiment), were ambiguous. In the period from 1984 to 2006, the AGASA array failed to confirm the reality of the GZK threshold. The total exposure in the experiment over this period reached 1.6×10^3 km^2 sr year.

In 1993, Fly's Eye detected an event with the energy 3×10^{20} eV. However, after the setup was updated, a sufficiently large number of events were identified in the period from 1997 to 2006, to support the conclusion that the cosmic ray spectrum is quite compatible with the notion of a CMB cutoff in the range $E_{GZK} \approx 5 \times 10^{19}$ eV [9]. The total exposure of the Fly's Eye over this period reached $\sim 3 \times 10^3$ km^2 sr year. Figure 1 shows the energy spectra of cosmic rays measured in the experiments HiRes [10] and AGASA.

The AGASA data provided the stimulus for developing a number of models in which UHE cosmic rays were born somewhere in the vicinity of Earth and hence the proton had no time to lose energy in collisions with CMB photons. These are the so-called top-down models, which involve new physics to explain particle creation with energies above the GZK cutoff. In contrast to this, the high energy of the particles in bottom-up models is a consequence of acceleration in objects existing in the Universe.

The power-law spectrum of cosmic rays shows that they could acquire such high energies as a result of stochastic processes in magnetic fields, as Fermi first suggested. The initial energy could be obtained, for example, from supernova explosions. This mechanism of acceleration can explain the origin of cosmic rays with energies up to $10^{18} - 10^{19}$ eV. The supernova idea lies at the heart of the bottom-up models of particle acceleration. (More details about this can be found in reviews [11–16].) The situation changed drastically when the Pierre Auger Observatory started obtaining energy spectra.

The installation of this array was started in 2000 in Argentina (Mendoza province), and the research phase of the work began already in January 2004. It was concluded in November 2008. The array consists of 1600 Cherenkov water

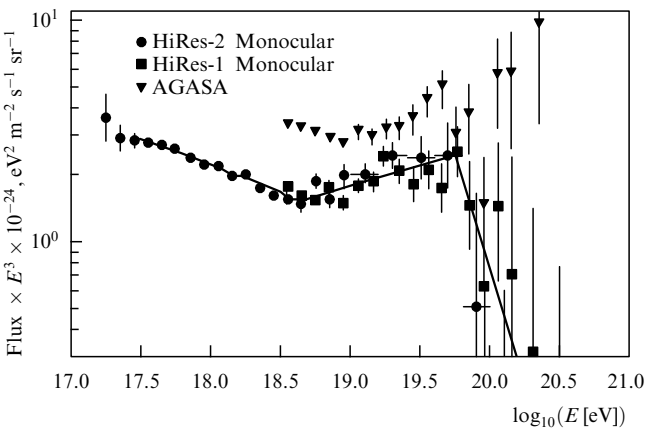

Figure 1. The energy spectra of cosmic particles according to the data of the AGASA and Fly's Eye experiments.

detectors spread over an area of 3000 km^2. Each tank 1.2 m in height and 3.5 m in diameter contains 12 t of pure water. The tanks communicate with the central station via microwave radio. Power to the electronics is provided by solar panels. The time of signal delivery from each tank is measured by GPS (Global Positioning System). The array is surrounded by four optical units of six fluorescence telescopes in each. The viewing angle of each telescope is 30° in the horizontal plane and 30° in the vertical plane [17].

The project combines a surface detector (water tanks) and a fluorescence detector. The hybrid design allows performing a highly accurate reconstruction of the geometry of a shower if at least one of the water detectors registers a single event simultaneously with the fluorescence detector. Such hybrid events are used to calibrate surface detectors, whose duty cycle approaches 100% (i.e., they work day and night). The results from the Auger Observatory fully confirm the existence of a GZK cutoff at $\sim 5 \times 10^{19}$ eV; the total exposure in the experiment reached 7×10^3 km^2 sr year [18].

Confirmation of the existence of the CMB cutoff indicates that the acceleration of cosmic particles in astrophysical sources is possible, and this practically eliminates the need to urgently search for exotic alternatives that avoid the GZK cutoff. This turning point also opens the way to search for astronomical sources of particles outside the Galaxy, while determining the direction of arrival of cosmic rays with energies close to the GZK cutoff. For example, correlation was reported by the Auger collaboration [19] between the arrival directions of cosmic rays with the energy above $\sim 6 \times 10^{19}$ eV and the coordinates of active galactic nuclei (AGN) (according to the data of AGN's Veron-Cetty catalog [20]) within a sphere of radius 75 Mps. In total, 27 events were investigated, with a view to search for correlations. The search was conducted with respect to the angular distance from the area of the observed events to an object in the catalog, with respect to the minimum energy and with respect to the redshift. The maximum correlation was found for the angle 3.1°, redshift < 0.018 (75 Mps), and energy $\geqslant 5.5 \times 10^{19}$eV. Using this data, the authors of [19] rejected the hypothesis of isotropic distribution of directions of UHE cosmic rays. The correlation that they discovered is compatible at a 99% confidence level with the hypothesis of extragalactic sources of UHE particles.

Models of processes by which particles somehow acquire the energy $> 10^{20}$ eV predict fluxes of cosmic rays depending on their energy. Obviously, not only is the experimental confirmation a proof of the validity of some hypothesis, but the agreement between the experimental and theoretical values of fluxes provides indirect support to the details of our understanding of astrophysical processes involved in the construction of the model. Many of the extreme processes in the Universe that result in high-density energy release, as well as astronomical objects associated with these processes, for instance, the active nuclei of galaxies, magnetars (neutron stars with a magnetic field $\sim 10^{11}$ T), and cosmic gamma-ray bursts (presumably resulting from mergers of neutron stars), are now well known. Nevertheless, we have not achieved a clear understanding of the nature of these phenomena and the mechanisms that lead to ultra-high-power energy releases. Consequently, confirming or refuting model hypotheses stimulates not only further research but also the development of new methods for detecting UHE particles.

2. Are there other possibilities of increasing the energy limit of detectors to a level higher than 10^{20} eV?

The situation we are now witnessing suggests the following question: what are the prospects for the study of UHE particles once the GZK cutoff has been confirmed? For example, a new wave of studies can be expected to soon enrich astrophysics with new data. All we need for that is to increase the 'aperture' of existing detectors or build new ones with the effective area increased by at least one order of magnitude, to complete the construction of the northern part of the Auger detector, and, finally, to implement projects of space-based detectors, e.g., OWL (Orbiting Wide-field Light-collectors) [21]. It is clear, however, that the prospects outlined in [22] will hardly advance astrophysics to energies significantly exceeding the GZK cutoff.

On the other hand, the top-down models have not been disproved, and, besides, it is hardly possible to explain all events with the energy above 10^{20} eV that accumulated over the entire history of cosmic ray research as experimental errors. Confirmation of the CMB cutoff only means that protons and heavy nuclei with the energy acquired outside the GZK sphere cannot bring the initial energy to us observers. It seems more natural to assume that the flux of UHE particles is much smaller than previously estimated [23], and their nature is still unknown.

This conclusion effectively means the following: if we stay with those technologies that led to the development of advanced detectors like AGASA, Fly's Eye, and the Auger Observatory, it is unlikely that we can achieve an effective area of about $10^6 - 10^7$ km^2 within the next 10–20 years without incurring enormous costs. This finding encourages the development of new methods that could greatly simplify the collection of information from a very large area.

One such idea suggests using the Moon as a target for UHE cosmic ray bombardment. A cascade shower in the lunar regolith is accompanied by a burst of coherent radio emission, which can be used to detect particles. This promising idea surfaced in the 1960s, i.e., more than 50 years ago, but so far it has failed to yield a technique for effectively measuring particle fluxes. Nevertheless, experimental studies continue with unflagging intensity, albeit with very few anticipated results to date. The idea of a radio detector, first suggested and tested in the 1960s, was very attractive owing to its simplicity and considerable promise. Consequently, before considering the current status of the radio astronomy method (which is the main goal of this review), we need to briefly describe its physical content and history, starting in the 1960s when Askaryan published two papers [24, 25] formulating an idea that still remains only partly implemented.

We know that practically all positrons and electrons of air showers result from the interaction between γ quanta and the nuclei of molecules in the air. Being created in a shower in pairs, electrons and positrons disappear via different channels. An electron remains in the shower until it loses almost all of its energy, while a positron is lost to the shower much sooner because it can annihilate with electrons of atoms in the atmosphere. This produces an excess of electrons in the cascade disk. Estimates [24] show an excess of electrons that amounts to about 10% of the total number of particles in the shower. The mean energy of such electrons corresponds to the Lorentz factor of the order of 100. Estimates of the intensity of the coherent Cherenkov radio emissions caused by an

excess of negative charge were made in [25]. According to these estimates, the emitted power appears to be quite sufficient for a reliable detection of RF pulses in the area within the Cherenkov cone on Earth's surface.

Some time later, in 1966, Kahn and Lerche [26] considered two more emission mechanisms using the separation of positrons and electrons of the shower in Earth's magnetic field. The energy spectrum reaches a maximum in the frequency range 30–50 MHz. Kahn and Lerche [26] compared theoretical estimates of the intensity of emission by the static dipole formed by spatially separated electrons and positrons with the intensity of emission by the current due to the transverse motion of negative and positive charges in the disk. They concluded that the geomagnetic mechanism causing the transverse current is dominant. The stimulating effect of papers [24–26] proved to be quite strong. Preliminary results of experimental work [27] became known almost immediately after the publication of [24–26].

A specific feature of experimental facilities for recording RF pulses was that the device for the formation of the so-called master signal was a compulsory element of every facility; it consisted, for example, of a bank of ionization or scintillation counters located on the ground near the antenna. These counters produced a pulse at the time of arrival of a cascade disk, whose velocity is practically identical to that of the radio signal. The signal from the radio receiver and the master signal are sent almost simultaneously by the electronic pulse shaping unit to the memory unit. This technique facilitates identification of the signal, which is especially important if the level of pulsed radio interference of atmospheric and technogenic origin is high.

The experimental setup in [27] was designed for studying showers with an energy of $10^{15}-10^{16}$ eV. The antenna of the experiment consisted of 72 half-wave oscillators with the eigenfrequency 44 MHz and bandwidth $\Delta\nu = 4$ MHz. To form a vertical radiation pattern, the array was placed at a height of $\lambda/8$ above the ground. The goal of the experiment was to test the theoretical estimates of the intensity of the Cherenkov mechanism of emission by excess electrons [24, 25]. The identification of this mechanism could be determined from the type of polarization of the radiation field.

The data obtained in [27] identified EAS as the source of RF pulses. Later, after updating the experiment, radio emission of a geomagnetic nature was recognized as being responsible for the predominant contribution. In subsequent years, various groups conducted research in two directions: searching for the yet unknown mechanisms of radio emission and learning the realistic capabilities of detectors based on measuring the Cherenkov or geomagnetic radiation.

These efforts failed to bring satisfying success. It was found that the signal intensity is only slightly higher than radio noise of artificial and natural origin and that the radiation pattern is actually constrained to the Cherenkov angle. The hope that several antennas would cover a larger area and therefore increase the detector aperture was thus effectively buried [28].

The search for new approaches to increasing the effective area of experimental units via extending the spatial radiation pattern of a cascade shower drew attention to the study of radio emission of δ-electrons. These are the electrons of the second or subsequent generations whose energy is still sufficient for ionizing neutral molecules in the atmosphere. δ-electrons are produced in inelastic collisions of shower particles with neutral molecules of the atmosphere (nitrogen and oxygen). The speed of these electrons is much lower than the speed of light and the energy spectrum of their emission is dominated by frequencies lower than in the Cherenkov radiation spectrum. At frequencies of the order of $1/\tau$, where τ is the time of shower propagation, the emission of δ-electrons can be considered quasicoherent. In essence, it is closer to bremsstrahlung if we consider a single electron [29, 30]. However, when the shower propagates through the atmosphere, the maximum of the energy spectrum lies at about 50–100 kHz, i.e., falls in the frequency range strongly affected by atmospheric and industrial interference. In addition, the intensity of the low-frequency coherent radiation of δ-electrons of an EAS in this frequency range is weaker by 2–3 orders of magnitude than the intensity of the Cherenkov and geomagnetic emissions, whose coherence is not disrupted at frequencies up to 30–50 MHz.

To avoid ambiguities in the rest of the paper, we need to comment on the mechanism of Cherenkov radiation by cascade showers. It is known that during the propagation of a shower, its electrons can lose energy and drop out of the cascade disk. At the same time, regardless of this, new electrons are produced as γ quanta interact with nuclei. In numerical calculations, the intensity was calculated by arithmetic summation of field intensities generated by individual electrons (see, e.g., [31]). This meant, in fact, that their initial phases are equal. To simplify the calculation, we assumed that the electron trajectory is a finite segment of a straight line, and the intensity of emission from individual tracks is proportional to their length. This approach to solving the problem allowed the use of a classical expression for the power of radiation from a single particle. However, this only applies when the observer is in close proximity to the actual trajectory of the electron and the wavelength of the radio waves in question is much shorter than this distance. This is the only case where a relatively short trajectory of the electron can be replaced by an infinite straight line. In Section 12, we analyze how this issue was solved in other cases, and in the rest of this paper, the expression "Cherenkov radiation of a shower due to excess electrons" is therefore understood as the radiation emitted by the current of excess electrons (this is Askaryan's interpretation in [24, 25]) and δ-electrons. As shown in [32], the motion of these particles can be treated as an integrated current and their contributions are nearly equal. More details of this work can be found in review [33].

The radiation intensity increases almost proportionally to the shower energy squared, and it is therefore expected that this mechanism will manifest itself most effectively in high-energy showers, especially in high-density media. In ground-based detectors, however, such a combination of conditions is not practically realizable. This quandary gave rise to the idea of the radio astronomy method in which the lunar surface would act as the target for particles. This possibility was first mentioned in [24, 25] and then examined in more detail in [34, 35].

3. Foundations of the radioastronomical technique

The Moon as a target for UHE particles is attractive not only because of the large area of the visible surface. The upper layer — the lunar regolith — does not contain moisture, and therefore its absorption of radio waves is almost nil, up to the

gigahertz range of frequencies, even at a depth of $\sim 10-20$ m. The lunar regolith consists of dust and small stones. The properties of this layer are known from the study of samples delivered to us from the Moon by the Apollo mission [36]: the average refractive index $n = 1.7$ and the mean length of attenuation of electromagnetic waves $\lambda_r = 9/(\nu\ [\text{GHz}])$. The following quantities are typically selected when considering the cascade processes: density of lunar regolith: 1.8 g cm^{-3}, radiation length: 22.6 g cm^{-2}, critical energy: 40 MeV, Moliére radius: 11.7 g cm^{-2} [37]. The most uncertain of the characteristics of the regolith is the attenuation length λ_r.

A particle can arrive from the vacuum at an angle $\Delta\theta$ to the surface of the Moon. According to geometrical optics and the well-known classical expression for the Cherenkov angle, $\cos\theta_{Ch} = 1/n$, a large fraction of the radiation (except, perhaps, in the case of a very low frequency) cannot pass across the interface due to the total internal reflection. In this connection, a case of considerable interest is that of particles arriving at the interface in the regolith-to-vacuum direction. However, only the neutrino can be such a particle. Because the GZK effect has been proved, we can assume that one of the sources of neutrinos is the decays of $\pi^{\pm}$ mesons produced in the interaction of cosmic high-energy protons with CMB radiation. Pulsars, supernova remnants, and nuclei of active galaxies can also act as sources of high-energy neutrinos. Ions accelerated in these objects are decelerated by the ambient medium and create neutral and charged pions, which decay and emit neutrinos. And finally, scenarios of the birth and evolution of the Universe are known in which neutrinos emerge from decays of so-called topological defects — relic particles with masses greater than 10^{20} eV.

Below, we describe the basics of the methodology of conducting experiments for determining the upper bounds on neutrino fluxes. Several experimental attempts are known, and their results were published in printed form or online [38–46]. Each of these papers uses one of the following starting notions to some extent.

(1) It is known that the effective cross section of the interaction of neutrinos with nucleons increases with increasing the energy. The effective range in the lunar regolith is $l_{eff} \sim 70$ km already for an energy of 10^{21} eV [47]. If the shape of the Moon is a perfect sphere, the angles $\Delta\theta$ between the surface and the particle trajectory on entrance and on emergence from it are equal. Of course, the probability of an event at the entrance is greater than at the exit point (i.e., a neutrino may not reach the exit point). Nevertheless, the entire effective range is of no interest for the reason mentioned above (this is not always so; see additional details in Section 12); an RF pulse from the cascade returns to the surface only if the distance between the surface of the Moon and the particle trajectory is less than 10–20 m. It is easy to see that for these values, $\Delta\theta \approx l_{eff}/2R_M \approx 1.15^{\circ}$, where $R_M = 1740$ km is the lunar radius.

(2) The power of an RF pulse increases with increasing the frequency in a wide range of frequencies, while the angular half-width of the radiation pattern becomes narrower. Therefore, there is an optimum range within which a substantial fraction of the radiation propagates across the lunar surface, while the pulse power is still considerable. It is assumed even now that the energy spectrum of the RF pulse falls off insignificantly with increasing the frequency up to ~ 10 GHz and that the frequency window favorable for detecting the pulse by a radio telescope is, taking the above into account, from about 2 to 3 GHz. But there exists a different standpoint, stemming from theoretical estimates; it is discussed in more detail in Section 12.

(3) Calculations show that for the observation frequency within 2–3 GHz, the angular 'thickness' of the Cherenkov cone in a homogeneous medium cannot exceed 2° (see Section 12.4). This means that approximately one half of the radiation pattern is outside the lunar surface, i.e., can reach the observer. This conclusion implies that only RF pulses caused by high-energy neutrinos are accessible to observation by ground-based radio telescopes. We need to remark, however, that the estimates used in [38–46] to establish the effective area of the detector were based on simple geometric arguments; it was found that they differ by an order of magnitude from the results obtained in terms of wave optics [48].

(4) The lunar surface is assumed to be so smooth that the nonuniformity of the interface becomes negligible. Model calculations assume that the layer of regolith 10 to 20 m in thickness underlying the lunar surface is uniform and has no appreciable effect on the propagation of RF pulses, except for attenuation due to absorption and effects caused by refraction. This assumption simplifies the estimation of the signal amplitude [38–46]. However, as is shown in Section 12.3, this effect can lead to almost complete disappearance of the signal across the antenna load even if the nonuniformity of the regolith is weak. Indeed, the lunar regolith is a product of crushing, mixing, and sintering of lunar rocks bombarded by meteorites and micrometeorites, and is therefore inhomogeneous in the sense of its state of aggregation, and the slightest changes in density, even at the level of 1%, would be catastrophic for the radio signal if the frequency of observation is in the range of 2 to 3 GHz [49].

(5) It is known that the Landau–Pomeranchuk–Migdal (LPM) effect plays a crucial role for the free path of high-energy particles in dense media; this effect consists of a sharp decrease in the cross section of the pair creation and bremsstrahlung processes. After the interaction with the nucleus, the neutrino energy is converted into the energy of leptons and hadrons. In the case of the electron neutrino (ν_e) or antineutrino ($\bar{\nu}_e$), the electron generated in a charge current initiates an electromagnetic shower, which, owing to the LPM effect, becomes so extended that radio detection becomes practically impossible. In the case of $\nu_\mu(\bar{\nu}_\mu)$ or $\nu_\tau(\bar{\nu}_\tau)$, the shower does not begin with leptons. Muons and τ-leptons first transfer their energy through electromagnetic [50] and photonuclear [51] interactions, and the shower starts only after this. But in this case, the energy of the shower is much lower than the energy of the initial particle and would not be detectable by a radio detector. It was therefore concluded that all showers except a hadron shower initiated by a neutrino, regardless of its flavor, are unimportant. Most of the energy of hadrons is converted in the long run into electromagnetic energy. Therefore, the Askaryan effect makes the Cherenkov emission usable for the detection of neutrinos with very high energies. Furthermore, it was shown in [52, 53] that the LPM effect lengthens the shower only slightly because, as a result of relativistic time dilation, the majority of π_0-mesons interact with the environment instead of decaying into photons, and their energy reduces to a level at which the LPM effect becomes negligible. A theoretical estimate of the power transferred to the hadronic shower is about 20%.

(6) After emerging from the lunar surface, the RF pulse reaches Earth's ionosphere, where it undergoes dispersion.

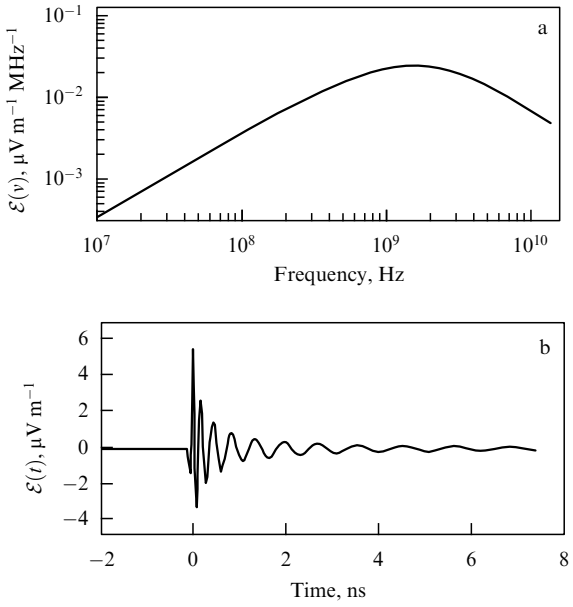

Figure 2. (a) The spectrum of the field strength of an RF pulse generated in the lunar regolith by a shower with the energy 10^{20} eV [53]. (b) The same pulse after passing through the terrestrial ionosphere.

For a shower with the energy $10^{21}-10^{22}$ eV, the Cherenkov RF pulse duration is no longer than 1 ns (if observed at the Cherenkov angle). This means that the energy spectrum of the shower is very wide, and the electromagnetic pulse is stretched in time after passing through the ionosphere. Figure 2a shows the spectrum of the field of an RF pulse induced in the lunar regolith by a cascade shower with an energy of 10^{20} eV. We see that the spectrum stretches, with only slight attenuation, up to frequencies of the order of 10 GHz. Figure 2b plots the same RF pulse as a function of time after passage through the ionospheric layer with the total electron content of 10^{17} cm^{-2} [39]. This picture is in good qualitative agreement with the notion of interaction between radiation and the ionosphere, but the quantitative conclusions raise doubts; the width of the emission spectrum of cascade showers is determined almost exclusively by the size of the source. We know that the characteristic size of the source (i.e., of the cascade disk) is $d \sim 12$ cm, and for the wavelength λ that satisfies the relation $dn \sin\theta_{\rm Ch} = \lambda = c/\nu n$ (n is the refractive index, $\theta_{\rm Ch}$ is the Cherenkov angle, and ν is the radiation frequency), the spectrum should fall off sharply at a frequency ~ 1 GHz. This is caused by the phenomenon of interference and corresponds to the superposition of two Fresnel zones emitting at the angle $\theta_{\rm Ch} \sim 54^\circ$. If we take the final size of the cascade disk into account [54], the analytic calculation using an approximate expression for the cascade function gives a spectrum that is fundamentally different from that in [39] (see Section 12.1).

(7) An RF pulse passing through the ionosphere experiences dispersion. High-frequency components of the spectrum reach the surface of Earth more quickly, which leads to a strong distortion of the signal. The initial bipolar RF pulse about 1 ns long takes a form resembling a damped pulse (Fig. 2b). The length of this RF pulse increases by a factor of tens or even hundreds, depending on the spectral composition. For this reason, a dispersion filter is included in the receiving unit of a radio telescope to reconstruct the initial shape of the pulse. It is obvious that the complete reconstruction of the primary pulse is impossible because the antenna of the telescope and the radio receiver have limited bandwidths. Furthermore, the relative time delay of the high-frequency and low-frequency parts of the spectrum in the dispersion filter can be regarded as a characteristic attribute of pulsed radio noise of terrestrial origin. The shape of pulses of local radio noise of atmospheric or terrestrial origin is greatly changed by passing through this filter, and hence can easily be eliminated from the analysis. The lengthening of the initial RF pulse after traversing the ionosphere was calculated in [39] as several nanoseconds (Fig. 2b). For the spectrum calculated in [54], the lengthening was nearly 200 ns [55]. Clearly, an incorrectly selected dispersion filter would make the RF pulse of the expected event 'invisible'.

4. Experimental study of Cherenkov RF pulses at the Parkes Observatory

After the publication of theoretical study [34], the first experimental attempt to detect an RF pulse using a radio telescope was the study of Cherenkov RF pulses with the 64-meter dish of the Parkes Radio Telescope Observatory. The experiment was conducted using the integrated antenna of Deep Space Communication in Canberra (Australia). The main objective of the work in [38] was to explore the Cherenkov radio emission induced by cascade showers caused by UHE neutrinos beneath the lunar surface. Radioastronomers expected radio signals about 1 ns long, subjected to dispersion in Earth's ionosphere. In general, the method followed the conclusion in [34]. The authors of [38] assume that the Cherenkov radio emission can reach the lunar surface from a depth of not more than 10 m and, because the apparent projection of the lunar surface is approximately 10^7 km^2, the total volume of the detector would be 10^{13} m^3, greatly exceeding the amount accessible to any terrestrial detectors. The number of events of the neutrino interaction with a detector of this volume should be at least 10^5 per year, or 1 event in 5 minutes. We can have an idea of how large this quantitative jump is by comparing this prediction with the frequency of events for energies $> 10^{20}$ eV on the Fly's Eye array (one particle per year) [5]. Observations used a low-noise radio receiver with the frequency band from 1175 to 1675 MHz. This means that the sensitivity threshold for the 64 m telescope is 450 Jy, while the radio flux at a frequency of 1400 MHz from neutrino events with the energy 10^{20} eV is expected to equal 4000 Jy [34]. The half-width of the radiation pattern of such an antenna in the selected range of frequencies is 13 arc min, i.e., only 20% of the lunar surface was efficiently used, while the rate of event repetition at energies $> 10^{20}$ eV dropped to 1 particle every 0.5 h.

To identify real events against the background of significantly stronger interference of terrestrial origin and radio receiver noise, distinctive attributes of polarization and dispersion in the terrestrial ionosphere were used. The Cherenkov radiation is linearly polarized and, because the antenna of the Parks observatory radio telescope has two orthogonal circular polarizations for each channel, it was expected that the amplitudes of radio signals in both polarization channels from the same event would be approximately equal. The signal from one of the polarizations was used to trigger the event registration, but both signals with different polarizations were set so as to perform verification by dispersion signature.

The experiment involved two radio receivers (radiometers), each of which selected one 100 MHz wide channel with circular polarization of one kind from the total bandwidth of 500 MHz. The signals of these channels were subjected to amplitude detection with the time constant less than 10 ns. Information about the total electron content in a unit-area column received from the Australian services of ionosphere forecast was used to establish the relative delay of the pulses in the separated radio channels ($\tau \sim 10$ ns). This delay was compensated by including an additional coaxial cable of the appropriate length between the higher-frequency detector and the oscilloscope. In this way, it was possible to detect terrestrial radio noise that did not travel through the ionosphere layer and arrived at the oscilloscope with the delay $\tau \sim 10$ ns with respect to the arrival time of the low-frequency radio channel. The oscilloscope was set to trigger the system at the instant when the input voltage (the signal from the two detectors) in both inputs increased within the time interval $7.5 < t < 20$ ns compared with the pre-set threshold value.

The threshold for system trigger by RF pulses was set at the level 8σ, where σ is the measured standard deviation of the detector output signal corresponding to the sensitivity limit of the Parks observatory telescope (450 Jy). The noise of each of the radiometers is statistically independent; the possibility for the noise in the two detectors to exceed the sensitivity limit of both detectors depends on the characteristics of the detectors. To adjust the level of the trigger signal, the repetition rate of radio noise pulses exceeding various threshold levels of each detector were measured and then compared with the frequency at which the trigger signal threshold was exceeded simultaneously in both detectors. In this way, it was possible to reduce the frequency of false triggers by statistical fluctuations by many orders of magnitude, while the increase in bandwidth from using two channels instead of one increased the sensitivity to low-level events by approximately a factor of $\sqrt{2}$.

Figure 3 plots the experimentally determined frequency of triggers as a function of the height of the selected threshold of the detector whose input was connected to the reference noise generator. The lower horizontal axis plots the values of the sensitivity threshold in units of the mean thermal noise level $T_{\rm sys}$ of the system. The upper horizontal axis plots the values of the equivalent threshold values of the flux of RF pulses in units of Jy. To catch events of the lowest energy when the frequency of false triggers was significantly higher than the frequency of true (i.e., lunar) events, it was necessary to set the lowest possible level of the trigger signal. For instance, Fig. 3 shows that for event registration at $E_\nu = 10^{20}$ eV in either of the two channels, it was necessary to set the trigger level to approximately 8σ. In the case of a single channel and the same frequency of false triggers, the threshold level has to be increased to approximately 13.5σ (or ≈ 6000 Jy).

The criteria for identifying a real event were set as follows:

(a) the event should be recorded at an instant synchronized with the detection system trigger;

(b) the event should carry a signature of being affected by the dispersion in the ionosphere, namely, the signal on the oscilloscope should become shorter after passing through the dispersion filter;

(c) the event should appear in both different-polarization channels and have identical signs of the impact of dispersion.

Pulses of terrestrial RF interference reflected from the Moon undergo a millisecond extension due to scattering by the rough lunar surface, and should not therefore trigger the

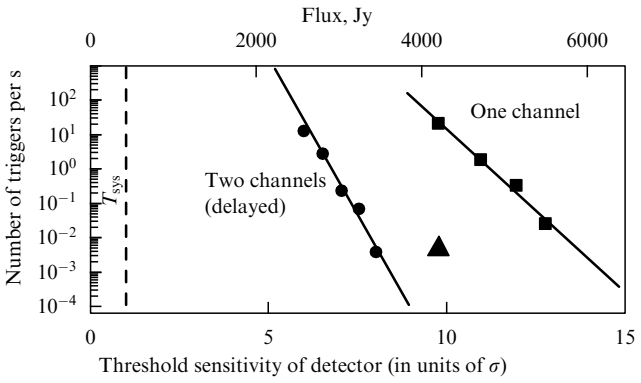

Figure 3. Frequency of raw triggers as a function of the height of the selected detector sensitivity threshold, given in units of standard deviations σ from the mean value in flux units (Jy). The triangle marks the value of the RF flux from the event $E_\nu = 10^{20}$ eV according to the data in [34].

system. The data of observations were selected from those collected during the night at full Moon when the Moon was above the telescope horizon in order to help reduce terrestrial interference. Although these assumptions were confirmed, many false starts triggered by car ignition circuits and other unidentified sources of pulsed radio interference were recorded.

Approximately 10 h of observation over three nights yielded about 700 events, of which at least 30% were confidently identified as terrestrial interference, typically appearing as a sequence of pulses. Among the other 500 events, none satisfied all the three identification criteria; about half of them belonged to false starts by random noise fluctuations and the rest seemed to be caused by weak terrestrial radio interference.

In their summary, the authors of [38] indicate that 24 real events should have been recorded in the course of the period of observation of the neutrino flux with an energy of 10^{20} eV. But because they found no events satisfying all three criteria, the authors of [38] concluded that the real neutrino flux with the energy $E_\nu \geqslant 10^{20}$ eV is at least an order of magnitude smaller than that predicted in [34].

5. First results of studying pulsed RF emission due to lunar events at the Goldstone Observatory (12 h of observation)

The main feature of the experiment in [39] on studying RF emission from lunar events conducted at the Goldstone Observatory (southern California, USA) consisted in the simultaneous operation of two antennas of the Deep Space Communications complex: 70 m (DSS-14) and 34 m (DSS-13) dishes separated by 21.7 km. This arrangement allowed reducing the number of false triggers associated with pulse noise by several orders of magnitude if the two antennas were used as a base for a coincidence circuit. The ideology of the experimental procedure was based on the results of several papers. An important role was played by paper [56], which presents the results of simulation of coherent Cherenkov radio emission in a dense medium and gives a detailed description of the electromagnetic pulse caused by the shower electrons with energies up to 10^{16} eV. Later, the range of energies in the simulation was extended [52, 57] to 10^{20} eV and the correction to the LPM effect was taken into account. The effects associated with the density of the lunar

regolith and with the geometric factor on the propagation of the RF pulse produced by the cascade shower are treated in [58, 59]. The results of this simulation strengthened the conclusions of previously published works (e.g., [34]) that lunar cascades should generate pulsed emission at cm wavelengths, which would be quite accessible for measurement. In fact, it was expected that the spectral curve of RF emission should reach a maximum at frequencies between 1 and 2 GHz and then stretch, slightly decreasing, to 10 GHz before strong signal attenuation sets in due to the loss of coherence as a result of the finite size of disks (Fig. 2a). Furthermore, laboratory measurements of the coherent Cherenkov and transition emissions from electron bunches with linear accelerators were performed [60, 61], which confirmed the quadratic dependence of the RF pulse amplitude on the number of electrons, as well as other important predictions about emission processes. These facts served as an additional incentive for conducting the experiment taking the results of previous measurements into account [38].

The first antenna (DSS-14), 70 m in diameter, was equipped with a receiver for two ranges: 1.6–1.7 GHz (range L) with a single polarization and 2.2–2.3 GHz (range S) with two kinds of polarization. In the case of two-location observations, DSS-14 was joined with DSS-13 — a 34 m antenna at a distance of 21.7 km to the southeast of DSS-14. The antennas were connected by a broadband analog fiber-optic communication line. The radiometer was structured as a superheterodyne receiver. The output signal of the antenna was fed to an amplifier with a limited bandwidth and then mixed in a heterodyne converter. Signals with the frequency 320 MHz, equal to the difference between the mixed frequencies, were extracted in the converter load, additionally amplified and passed through a 100 MHz bandpass filter.

In the single-antenna mode, the experimental setup had a trigger unit that demanded the time overlap of logic pulses from the S-range $\geqslant 5$ ns (in the interval 10–20 ns) at 2.2–2.3 GHz with left-hand circular (LC) and right-hand circular (RC) polarizations. Because Cherenkov RF pulses are linearly polarized, the signal amplitude is the same for the LC polarization (LCP) and the RC polarization (RCP). This type of coincidence is very effective for the cutoff of the interference from microwave telemetry systems (such as orbiting satellites) because the polarization of this noise is almost always circular. However, such a coincidence is sensitive to pulsed interference generated by electric sparking. In this case, radio pulses are also linearly polarized. Consequently, a system was developed for optimization of trigger circuits using an additional receiver and the L-range (1.6–1.7 GHz). When DSS-14 worked in the S-range, the L-range was used for scanning the area of the sky at the angular distance $\approx 0.5^\circ$ from the Moon. The nonzero response in both the L-range and the S-range indicated that the source of the RF pulse is not a neutrino event.

It was found that all false triggers due to terrestrial RF pulse noise are eliminated by using the L-range signal to block the entire system. This method has been tested several times, and the system was triggered by noise only once, under extreme observation conditions when the trigger frequency (with a threshold $> 4.5\sigma$ for both polarizations) without this blocking was 1.5 kHz. With the blocking turned on, the trigger rate due to RF interference dropped to < 0.01 Hz. Such conditions were not typical for the entire duration of observations. The mean rate of starting due to the RF interference was 1 trigger every several minutes. The effectiveness of this method has thus been convincingly demonstrated.

Each time the system was triggered, it memorized the amplitude and other parameters of signals in the S-range for the LC and RC polarizations and for the L-range with LC polarization (blocking channel). For an event to be identified as one of lunar origin, it was necessary to have:

(a) a constraint on the bandwidth in accordance with the expected duration of the Cherenkov pulse ~ 1 ns;

(b) only an insignificant time shift and difference between amplitudes in signals with different polarizations (RC and LC);

(c) no appreciable signal in the L-range;

(d) the amplitudes of the signals of two polarizations close to the expected values.

(e) In the case of observation in the dual antenna mode, an additional criterion was satisfied: the width-constrained signal had to be registered by the DSS-13 antenna within the time window compatible with the geometric delay corresponding to the propagation of the signal from the lunar surface to each of the two antennas.

The characteristic rate of data accumulation was 0.1 Hz for the single antenna operation and 0.01 Hz for two antennas. Most of these triggers accidentally coincided with thermal noise pulses in two polarizations, and hence the subsequent processing of the data included setting a threshold to exclude the possibility of accidental coincidences of noise pulses. According to this requirement, the triggering threshold for signals of the 70 m antenna (DSS-14) exceeded the 6σ level in the channels of both LC and RC polarizations. In addition, a triggering threshold $\geqslant 4\sigma$ was set up for the DSS-13 antenna channel. These requirements can be expressed as the energy threshold (taking the sensitivity of the telescope into account) $\Delta S = 2k_{\mathrm{B}} T_{\mathrm{sys}} A_{\mathrm{eff}}^{-1} (\Delta t \Delta \nu)^{-0.5}$ [$\mathrm{V\,m^{-2}\,Hz^{-1}}$], where T_{sys} is the noise temperature of the antenna, A_{eff} is its effective area, Δt is the time constant (signal acquisition time), and $\Delta \nu$ is the system bandwidth. For the system described above, the mean-square deviation of thermal noise at the 1σ level is 400 Jy, and the 6σ level corresponds to 2400 Jy. If all cascades are of hadronic origin at this energy, the mean neutrino energy must be five times the cascade energy, i.e., the actual threshold neutrino energy becomes 5×10^{19} eV.

Observations of the central area of the Moon were conducted for 4.8 h, of the area between the center and the limb for 5.6 h, and of the limb for 1.5 h. Eight hours of observation were in the two-antenna mode and four hours with a single antenna. The analysis of all recorded pulses detected no events that would simultaneously satisfy the above requirements a–e. The authors of [39] concluded that this observation imposes restrictions on the particle flux predicted by some models. For example, the model of topological defects predicted 12 events [62]. Furthermore, 3–4 events were expected to be caused by UHE cosmic rays [63], e.g., protons, which form the shower immediately below the surface. Nothing of the sort was discovered, however, and the authors of [39] concluded that this forecast should be revised for two reasons ignored in [63]. First, we need to account for the geometry of the cascade induced by cosmic rays and the associated phenomenon of total internal reflection in the lunar regolith. Second, we need to account for the role of the effective suppression zone of emission from cascades that very nearly skim the surface of the regolith. The authors of [39]

concluded that only narrow ridges or similar features should be effective in the generation of radio emission from UHE cosmic rays (but not from neutrinos).

6. Continued experimental study of RF emission due to neutrino cascades and cosmic rays at the Goldstone Observatory (30 h of observation)

The Askaryan effect [24, 25], which consists in the generation of excess electrons in cascade showers, can be given a physically simple and intuitive interpretation. Unfortunately, quantitative results of calculations inevitably raise doubts, and errors by an order of magnitude or larger play a crucial role in evaluating the effectiveness of the radioastronomical method. This argument stimulated the conduction of several series of laboratory measurements involving direct verification of the Askaryan effect [64, 65].

The transition radiation caused by the interaction of electrons accelerated to 15.2 MeV with aluminum foil was measured in [64]. To investigate the Cherenkov radiation, natural sand was used as a target. Direct proof of the formation of an excess of negative charges and the phenomenon of coherent Cherenkov radio emission due to this excess was first reported in [65]. A picosecond pulse of bremsstrahlung γ-quanta produced by the Stanford linear electron accelerator (SLAC) was sent into a target of 3.5 tons of sand. Electrons were accelerated to an energy of 28.5 GeV. The number of particles per bunch could be varied in the range $(0.1-1.0)\times10^{10}$. Each of the bremsstrahlung γ-quanta produced a small cascade shower in the sand and the energy of the total cascade deposited by the whole bunch reached 10^{19} eV. A series of range antennas from 0.3 to 6 GHz detected strong nanosecond RF pulses induced by the cascade shower in the sand [65]. According to the authors of [65], the measured polarization, coherence, field strength, and other parameters were consistent with the predictions in [24]. These facts encouraged researchers [39] to conduct a new series of measurements at the Goldstone Observatory, although, contrary to expectations, not a single event generated by a UHE particle was identified in the previous experiment.

Paper [66], which is a sequel to [39], presents the results of a 30-h experiment GLUE (Goldstone Lunar Ultra-high energy neutrino Experiment) at the Goldstone Observatory aimed at determining the upper bound on the flux of cosmic UHE neutrinos. Even though the introduction of the new method of triggering the detection unit by lunar events significantly reduced the terrestrial interference, once again no candidates for RF pulses of lunar origin were found.

By the mid-2000s, the project initiated in [39] gained the status of a permanent experiment and a schedule of regular observations was established. The results of measurements yielded a new upper bound on the diffuse neutrino flux with neutrino energies higher than 10^{20} eV. Later estimates [66] accounted for the fact that the lunar regolith through which a cascade propagates is a layer composed of small particles and smallish stones that presumably are products of collisions of meteors with the lunar surface. The regolith is composed of silicates and related minerals and contains several percent iron and titanium compounds and traces of meteoritic carbon. The average dielectric constant is $\varepsilon\approx3$, the density $\rho\approx1.7$ g cm^{-3}. These parameters increase slowly with depth. The measured value of the loss tangent at high frequencies is $\tan\delta\approx0.003$, and the expected field attenuation length at the frequency 2 GHz is $\alpha^{-1}=9$ m.

The following geometrical relations were taken into account in correcting the estimate of the upper bound on the neutrino flux. For an electron or muon neutrino with an energy of 10^{20} eV, the average interaction length $L_{\rm int}$ is 60 km [47, 67]. The interaction that causes a cascade at a depth of 10–20 m from the lunar surface is secondary, and the cascade energy is only 20% of the initial neutrino energy. The excess of negative charge in the electron–photon cascade results in a cone of Cherenkov radiation with an opening angle of 56° and angular 'thickness' of cone walls of the order of 1° (at the half-width of the diagram). Electromagnetic waves from the cascade undergo refraction at the vacuum–regolith interface. Because the Cherenkov angle is $\theta_{\rm Ch}=\arccos(1/n)$, the authors of [66] assume that the radiation emerges from the lunar surface only if the cascade propagates in the regolith-to-vacuum direction, and the angle between the transition and the surface of the Moon $\theta_{\rm up}$ is less than 1° for particles with an energy of 10^{20} eV, i.e., $\theta_{\rm up}\approx L_{\rm int}/2R_{\rm M}$. This requirement takes both the above geometrical relation and the total internal reflection at the interface of the two media into account. Figure 4 shows the directions of cascade propagation (CA), the direction of neutrino motion (AB), and the direction of radiation after refraction (DE), with $\mathrm{BC}=L_{\rm int}$, $\mathrm{AC}\ll\mathrm{BC}$, $\mathrm{OA}=\mathrm{OB}=R_{\rm M}$, and $\angle\mathrm{DCA}=\theta_{\rm Ch}$.

Although this experiment used the same antennas (the 70 m DSS-14 and the 34 m DSS-13, separated by 21.7 km), the system startup and discrimination of events became much more complicated. A detailed description of the system startup technique and of the event selection method are beyond the scope of this review, however. More essential for what follows is the choice of the expression for estimating the spectral field strength $\mathcal{E}_0(\nu, R)$ caused by a cascade with the total energy $E_{\rm t}$ [56, 63, 57]. Instead of the parameterization of field strength found previously [56],

$$R\left|\mathcal{E}(\omega,R,\theta_{\rm Ch})\right|=1.1\,\frac{\mathcal{E}_0}{1\ \mathrm{TeV}}\,\frac{\nu}{\nu_0}\,\frac{1}{1+0.4(\nu/\nu_0)^2}\ [\mathrm{V\,MHz^{-1}}], \tag{6.1}$$

where ω is the cyclic frequency, ν is the frequency of oscillations, $\nu_0\approx500$ MHz is the frequency of coherence violation in lunar regolith, and R is the distance to the source. An improved parameterization, in the form [65]

$$\mathcal{E}_0(\nu,R)=\frac{2.53\times10^{-7}}{R}\,\frac{E_{\rm t}}{1\ \mathrm{TeV}}\,\frac{\nu}{\nu_0}\times\left(\frac{1}{1+0.4(\nu/\nu_0)^{1.44}}\right)\ [\mathrm{V\,m^{-1}\,MHz^{-1}}], \tag{6.2}$$

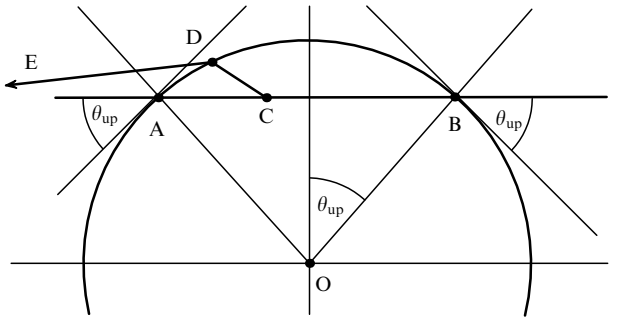

Figure 4. The direction of motion of a neutrino (AB) and of a cascade (CA) beneath the lunar surface. CD is the direction of emission and DE is the refracted ray.

Table 1. Differential limits for monoenergetic neutrino fluxes.

Energy, eV	10^{19}	3×10^{19}	10^{20}	3×10^{20}	10^{21}	3×10^{21}	10^{22}	3×10^{22}	10^{23}
$\log_{10}(E^2\,\mathrm{d}F/\mathrm{d}E\,[\mathrm{GeV\,cm^{-2}\,s^{-1}\,sr^{-1}}])$	−3.14	−3.66	−3.92	−3.91	−3.73	−3.42	−3.03	−2.66	−2.30

was introduced, in which $R\approx0.38\times10^9$ m and $v_0=2500$ MHz. For typical parameters in this experiment, we find $\mathcal{E}\approx0.5\times10^{-6}$ V m^{-1} for the frequency band at 70 MHz. The authors of [66] are of the opinion that expression (6.2) has been confirmed in accelerator experiments up to a factor of 2 [64, 65]. This expression allows determining the threshold energy of a cascade. For this, we need to take into account that the signal generates a voltage v_s across the terminals of the antenna, which is related to the field strength $\mathcal{E}_0$ as $v_s=h_e\mathcal{E}_0\Delta\nu$, where $h_e=2\sqrt{Z_a\eta A/Z_0}\cos\theta_p$ is the effective length of the antenna [68], Z_a is the radiation resistance, η and A are the efficiency of the antenna and its area, $Z_0=377\ \Omega$ is the impedance of free space, and θ_p is the angle depending on the polarization direction of the pulse relative to the polarization plane of the antenna. Furthermore, the Nyquist formula for the rms amplitude of thermal noise gives $v_n=\sqrt{4k_BT_{sys}Z_t\,\Delta\nu}$, where T_{sys} is the noise temperature of the antenna, approximately equal to the thermodynamic temperature of the lunar surface, and Z_t is the value of the equivalent resistance at the receiver input. If we take into account that $Z_a\approx Z_t$, the signal-to-noise ratio is $v_s/v_n=\mathcal{E}_0\sqrt{\eta A\Delta\nu/k_BT_{sys}Z_0}$.

For the minimum detectable field, $\mathcal{E}_0\to\mathcal{E}_{min}$. Then expression (6.2) gives the threshold energy of the cascade as

$$E_{thr}\approx4\left(\frac{\mathcal{E}_{min}}{1\ \mathrm{V\,m^{-1}\ MHz^{-1}}}\right)\left(\frac{R}{1\ \mathrm{m}}\right)\frac{v_0}{v}\times\left[1+0.4\left(\frac{v}{v_0}\right)^{1.44}\right]\mathrm{[EeV]}\,. \tag{6.3}$$

When the radio telescope focuses on the limb, $T_{sys}\approx110$ K. Furthermore, $\nu=2.2$ GHz, $\Delta\nu=70$ MHz, $\eta=0.8$, $A=4900$ m^2, and $\langle\cos\theta_p\rangle=0.7$. For these values, the minimum field strength is $\mathcal{E}_{min}\approx1.2\times10^{-8}$ V m^{-1} MHz^{-1}. For these parameters and $v_s/v_n=5$ (i.e., for the trigger level 5σ), the threshold energy is estimated as $E_{thr}=2.8\times10^{19}$eV.

If the effective volume (or the effective area) and the duty cycle of the detector are known, the model predictions for UHE space particle fluxes can be checked. Not a single pulse with a signature of lunar origin was identified in over 30 h of observations with the trigger threshold of 5σ. However, the flux pattern implied by the model of topological defects predicted several events over the time of observation. This discrepancy may indicate both shortcomings of the theoretical model and fundamental errors incorporated in the calculation of the threshold energy of a cosmic particle or of the effective area of the detector. The absence of events in a properly designed experiment serves to identify a model-independent upper bound on the flux of cosmic particles. If we know the differential flux of particles $\Phi(E)=\mathrm{d}N/\mathrm{d}E$ [m^{-2} s^{-1} sr^{-1}], then the total number of events N over a certain time of observation can be written as

$$N=\int\lambda(E)\,\Phi(E)\,\mathrm{d}E\,,$$

where $\lambda(E)$ is the function that gives the total exposure for each value of energy, i.e., the effective area of the detector times the 'live' observation time and $\Delta\Omega$ (the range of solid angles in which the particle is detectable, in other words, reaches the target in the required manner).

For the zero result of observations, the inequality $N\leqslant N_{up}\approx2.3$ [69] holds for the 90% confidence interval. If the differential spectrum is sufficiently smooth, we can set $\Phi(E)\leqslant N_{up}/E\,\lambda(E)$. This is precisely the model-independent bound on the differential flux in the case of observations finding zero events [69]. The authors of [66] found that such bounds can be established for certain neutrino energy values. Table 1 presents the maximum possible neutrino fluxes $\mathrm{d}F/\mathrm{d}E$ (on the scale $\log_{10}(E^2\,\mathrm{d}F/\mathrm{d}E)$) for selected values of the energy E in the range $10^{19}-10^{23}$ eV (F is the integral particle flux). The measured neutrino fluxes turned out to be lower than the values predicted by the model of topological defects (approximately 1 or 2 events).

7. Completion of the experimental study of RF emission due to neutrinos and cosmic rays at the Goldstone Observatory (120 h of observation)

The final series of observations at the Goldstone Observatory used the experimental technique described in [66], but the event selection and analysis system was substantially upgraded and improved [41].

Figure 5 gives a block diagram of the latest version of the experimental setup. Signals from the DSS-14 and DSS-13 antennas were fed to a low-noise linear amplifier (LNA) and then converted to a signal in the mixer with a frequency

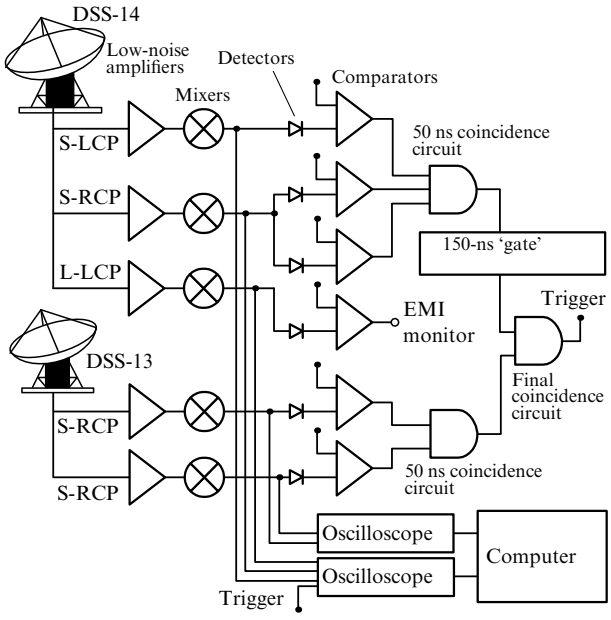

Figure 5. Block diagram of the detector of the Goldstone Observatory (project GLUE). S-LCP and S-RCP are the respective signals in range S with left-hand and right-hand circular polarizations L-LCP is the signal with left-hand circular polarization in range L. EMI monitor (EMI, Electromagnetic Interface) is a device for the visual display of information on electromagnetic interference.

difference of 300 MHz. The amplitude detector with the time constant 10 ns includes tunnel diodes required for the efficient conversion of signals to unipolar pulses. A comparator is used to compare the amplitudes of the incoming pulses with the threshold level. In addition, the signals were checked for coincidence (50 ns coincidence circuit) within 50 ns in one channel for each antenna. The coincidence of the amplitudes of the signals of the two circular polarizations in the DSS-14 antenna ensured that the signals were linearly polarized, and the coincidence of the amplitudes of the frequency-separated channels was an indication that the initial signal was a broadband one.

In order to not waste time analyzing and recording the false pulses allowed by the comparator, the DSS-14 electronics formed a time 'gate' up to 150 μs wide, which covered the possible geometric range of delays in the arrival of signals from the Moon to each antenna during a year. If the signal from the DSS-13 unit failed to arrive within this 'gate', all subsequent processing and analysis were canceled. In the case of a high noise level, the time window was automatically narrowed. If a signal from the DSS-13 arrived within this interval, the entire information of the two channels was recorded in 250 μs by digital oscilloscopes with a discretization sampling rate of 1 GS (Giga-sample) per second. The signals were then analyzed with a computer. The average trigger signal rate (mostly due to random coincidences from thermal noise) was not greater than 3×10^{-3} Hz. The average number of false triggers due to local radio noise over the entire experiment duration was a few percent of the total number, and the fraction of the 'live' observation time was close to 95%.

The accuracy of the geometric relations in the experiment plays an important role in the selection of radio signals of lunar origin. The relative delay between signals from two antennas is $\tau = c^{-1}B\cos\theta$, where θ is the angle between the baseline and the direction to the Moon. With the baseline length $B = 22.7$ km, the maximum delay time is $\tau_{\max} = \pm 73$ μs. The sought event can occur in any area of the lunar surface within the antenna beam. As a result, the possible spread of relative delays between antenna signals is 630 ns.

The angular width of the main lobe of the angular pattern of the 70 m antenna at the half-maximum width is approximately 10–15 arc minutes. In the observation of the Moon's limb, a part of the pattern covers a bit of the celestial sphere, and the noise temperature of the antenna differs from that in the case of observation of the central lunar area. In a number of estimates, the limb temperature was set at 70 K and the temperature at the center of the Moon at 160 K. Better measurements of the delay time of signals propagating along a fiber optic line (≈ 22.7 km long) yielded the value 136 μs. The results of the updated time and amplitude calibration were also taken into account.

Figure 6 shows a typical diagram of signals that initiated triggering of the detector. The signal power is normalized to the local average power over the time interval of 250 μs. Figures 6a, b plot the record of signals with left-hand and right-hand circular polarizations received by the DSS-14 antenna. A narrow pulse present in the signals of both polarizations is an indirect indication of the broadband spectrum of the initial pulse, but it also indicates a high degree of linearity of polarization. Figures 6c, d show signals in both channels of the DSS-13 antenna. A record of signals from the DSS-14 antenna in range L, used in the anti-

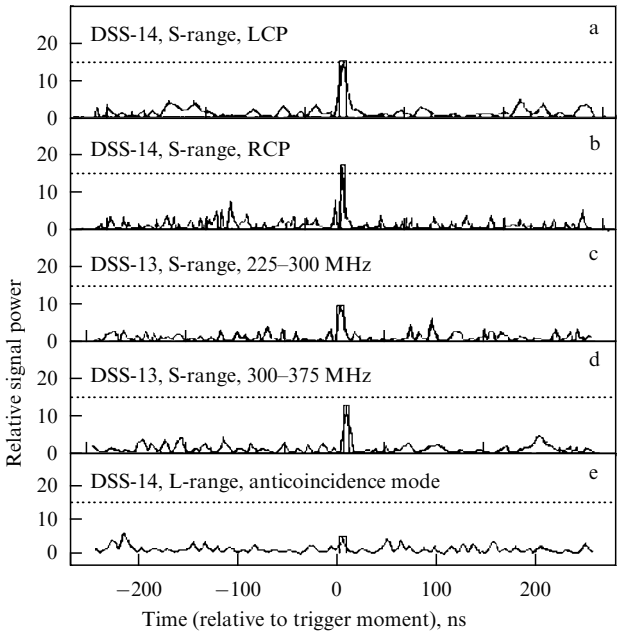

Figure 6. Typical record of a signal that triggered the detector of the Goldstone Observatory.

correlation mode, is shown in Fig. 6e. The radiation pattern of this beam is shifted outside the lunar limb by 0.5°. The reason why the RF pulse in Fig. 6e has no signs of lunar origin is the presence of a signal in the L-range and the fact that the relative delay between signals of two antennas is approximately 2×630 ns. In this case, the delay turned out to be 1.1 μs.

No events with signs of lunar origin were identified over 120 h of live observation time. However, the null result of this experiment (observation with a threshold level of 6σ for detection triggering) does allow setting model-independent constraints on the UHE neutrino flux. Among other things, the authors of [41] conclude that in view of the results of GLUE [41] and the data collected by FORTE (Fast On-orbit Recording of Transient Events) considered jointly [70], the quasimonoenergetic model of Z-bursts [2, 3] can be rejected or severely constrained. We know that this model explains the value, well known today, of the flux of cosmic rays (mostly protons) with energies above the GZK cutoff. According to this model, protons with this energy may result from the interaction of UHE neutrinos ν with cosmic background neutrinos $\bar{\nu}$, whose density is assumed to be sufficiently high. The resulting Z_0 boson decays into quarks, which then decay into protons or some other hadrons [71–73]. If the model parameters such as the neutrino mass, the energy spectra of the neutrinos, or the distance to the source vary, then the chain of interactions $\nu + \bar{\nu} \to Z^0$ can explain the value of the flux of cosmic rays known from experiments at the EAS facilities [74–78]. The neutrino energy required for this is $10^{23} - 10^{24}$ eV [79, 80].

The authors of [41] also believe that their results, together with those obtained in the experiment on the FORTE mission in the energy range $> 10^{22}$ eV, indicate strong restrictions on the model of formation of cosmic rays known as the model of 'cosmic topological defects'. This model is based on the theoretically predicted possibility of creating UHE particles under certain conditions in the early Universe. There are a number of mechanisms of formation of UHE cosmic particles

by topological defects [81]. As topological defects decay, the ultimate result is the formation of ordinary particles with the energy above the GZK cutoff.

8. Experimental study of radio emission by cascade showers beneath the lunar surface using the UTR-2 radio telescope

The advantages obtained by measuring radio emission from cascade showers at wavelengths comparable to the length of the cascade shower were often mentioned in [33]. The main advantage stems from the wide radiation pattern. Even for particles that intersect the interface at small angles, an essential part of the radiation pattern still emerges above the lunar surface. Estimates of the spectral intensity of the field of a cascade whose length is much smaller than the wavelength were obtained in [82, 83]. These estimates were sufficiently high to entertain hope of a realistic feasibility of identification of several high-energy events. To illustrate the possibility of such an experiment, we use the expression for the intensity of radio emission [84, 54]

$$W_{\rm r}(\omega)=\frac{{\rm d}E(\omega)}{{\rm d}\omega\,{\rm d}s}=\sqrt{\varepsilon}\,\frac{\varepsilon_0 c}{\pi}\,\omega^2\sin^2\theta\left|\mathbf{A}(\omega)\right|^2$$
$$=\frac{\mu_0}{c}\,n\left(\frac{0.31\exp(\alpha)\,z_0\eta e}{4\pi r}\right)^2\exp\left[-\frac{3\alpha}{2}\,\left(\frac{p\omega z_0}{c}\right)^2\right]\omega^2$$
$$\times\exp\left[-(k\rho_1\sin\theta)^2\right]\sin^2\theta\quad[\mathrm{J\ Hz^{-1}\,m^{-2}}]\,,\qquad(8.1)$$

where $\alpha=\ln E_0/E_{\rm cr}=33$ for the cascade energy $E_0=10^{22}$ eV, $E_{\rm cr}=0.4\times10^8$ eV is the critical energy of electrons in the lunar regolith, $z_0\approx0.14$ m is the avalanche unit of length, $p=1-\beta n\cos\theta$, $\beta=v/c$ is the relative speed, $n=1.7$ is the refractive index, $\rho_1=0.9\times(21\ [\mathrm{MeV}]/\ E_{\rm cr}\,[\mathrm{MeV}])\,z_0\approx0.06$ m is the rms radius of the cascade disk, $r=0.38\times10^9$ m is the distance to the Moon, $\eta=0.2$ is the fraction of excess electrons, $\mu_0=4\pi\times\ \times10^{-7}$ H m^{-1} is the magnetic constant, $c=3\times10^8$ m s^{-1}, θ is the angle of observation, and k is the magnitude of the wave vector.

Figure 7 plots the diagram of radiation intensity distribution (8.1) in the Cherenkov cone as a function of the emission angle at the observation frequency $\nu=30$MHz. The width at half maximum, equal to $\Delta\theta_{1/2}=64^\circ$, means in fact that at small angles between the particle trajectory and the lunar surface, the bulk of the emitted radiation does not experience total internal reflection at the regolith–vacuum interface.

To measure radio emission caused by a cascade shower beneath the lunar surface, the antenna of the radio telescope UTR-2 (Kharkov) was used [43, 85–87]. This antenna, designed to work in the frequency window 15–30 MHz, consists of 2040 broadband dipoles positioned on two arms at right angles (1440 along the meridian and 600 along the parallel). The UTR-2 beam orientation system is electric and discrete, and it allows pointing the beam at any point on the celestial sphere within a cone with the opening angle $\pm70^\circ$ relative to the vertical. Several beams can be formatted as needed for observations at different frequencies. A system of anticorrelations was used in these experiments to reduce the number of false starts due to radio interference of local and distant origins. To achieve this, one beam of the antenna was aligned with the lunar surface, while the other passed near the Moon at a distance of a few degrees. If the signals were received from both beams, this was interpreted as a terrestrial origin of the RF pulse. Each of the two beams was equipped with a dedicated unit of amplifiers and a unit for signal recording.

The functional diagram of one of the blocks of the telescope is shown in Fig. 8. Signal A_1 of one of the beams passed through a band filter (BF) (28–30 MHz) and was then fed to a high-frequency amplifier (HFA) and then to a quadratic amplitude detector assembled of tunnel diodes. After additional amplification in an IA (Impulse Amplifier) cascade, the signal amplitude was measured and a square pulse was formed for further analysis. The electronic key (EK) opened only if its input received no pulsed noise signal from industrial mains (50 Hz, 220 V) or from the half-wave dipole A_2. The RS and A blocks are auxiliary amplifiers. The coupling capacitance C and the input impedance R of the amplifier A were chosen so as to satisfy the condition $RC\approx2$ ms.

In passing through the ionosphere, an RF pulse greatly changes its shape. Figure 9 (a) shows the initial RF pulse observed at the Cherenkov angle, i.e., the pulse whose spectrum is given by formula (8.1), and Fig. 9 (c) shows the

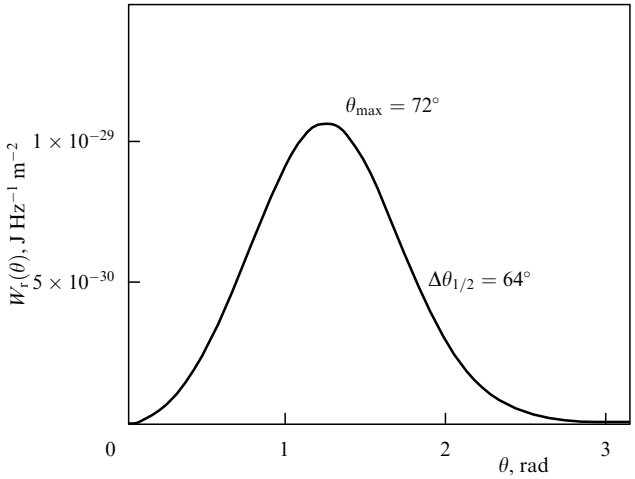

Figure 7. Diagram of radiation intensity distribution (8.1) across the 'thickness' of the Cherenkov cone as a function of the emission angle at the observation frequency $\nu=30$ MHz.

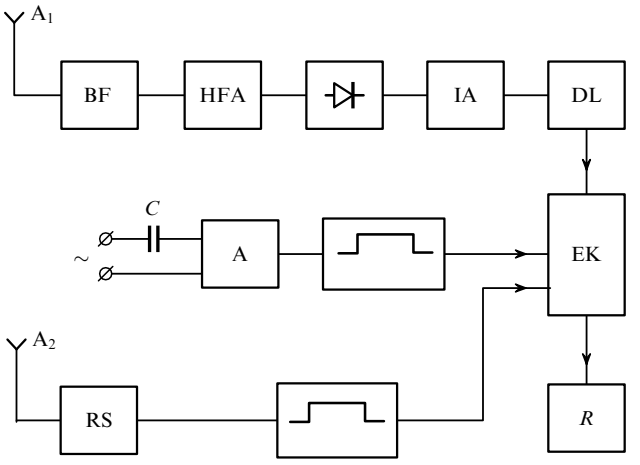

Figure 8. The functional block diagram of one of the electronic blocks of the detector based on the radio telescope UTR-2.

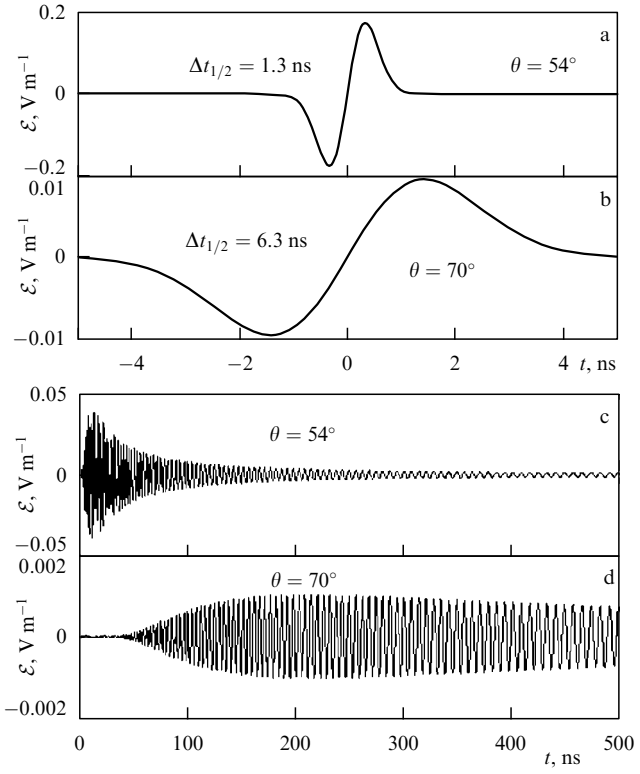

Figure 9. Shape of the initial RF pulses observed at the Cherenkov angle (a) and at an angle 70° (b). (c, d) The same RF pulses after passing through the terrestrial ionosphere.

RF pulse after passing through the ionosphere [55]. The duration of the initial pulse is about 1 ns when observed at the Cherenkov angle. The choice of the time constant of the amplitude detector was made in the following manner. Due to the dispersion of RF pulses in the ionosphere, the time needed to cover a path of length L at a fixed frequency ω is [88]

$$t = \frac{1}{c}\int_0^L \frac{\mathrm{d}x}{nc}\,, \tag{8.2}$$

where $n(r) = \sqrt{\varepsilon} \approx 1 - AN_\mathrm{e}(r)/\omega^2$, N_e is the electron concentration, and $A \approx 1.6 \times 10^3$ (m^3 s^{-2}). Then the relative delay Δt of signals corresponding to the boundaries of the 28–30 MHz range is

$$\Delta t = \frac{AN_1}{c}\left(\frac{1}{\omega_1} - \frac{1}{\omega_2}\right) \approx 2.2 \times 10^{-6}\ \mathrm{s},$$

where $N_1 \approx 5 \times 10^{16}$ m^{-2} is the characteristic value of the total electron content in a unit-area column of the ionosphere. Hence, it can be concluded that if the reception band of the unit is broadened by a factor n, then the signal amplitude increases by about the same factor, and the corresponding increase in the time constant by n reduces the noise level also by n. This compensates for the decrease in the signal amplitudes as the pulse becomes longer due to dispersion.

The sensitivity of the system can be estimated as follows. The power of radio noise $P(v, T)$ per unit frequency across the load of the antenna is determined using the Nyquist formula $U^2 = 4k_\mathrm{B}TR\Delta v$, where $U = (\overline{U^2})^{1/2}$ is the rms amplitude of the radio noise, R is the active equivalent resistance, and T and Δv are the temperature of the antenna and the frequency range. Therefore, the total energy flux for a coupled antenna (with the source resistance equal to the load resistance) is $k_\mathrm{B}T$. Because the beam of the active arm of the UTR-2 antenna is much larger than the angular size of the Moon, the antenna temperature T is determined by the equivalent temperature of the celestial sphere at a frequency of 30 MHz. We can approximately set $T \sim 5000$ K [89–91]. Then, with the effective area of the antenna $\approx 10^5$ m^2, the specific flux of radio noise is $P_1 = 7 \times 10^{-25}$ W m^{-2} Hz^{-1} (or 70 Jy). This means that for a reliable reception of signals (for the signal-to-noise ratio 3), the specific flux from the source should be ≈ 210 Jy.

On the other hand, Eqn (8.1) (see also Fig. 7) implies that the total amount of energy incident on 1 m^2 of area per unit frequency band over the entire duration of emission (at the location of the antennas) is $W_\mathrm{r} \approx 10^{-29}$ J m^{-2}. Given the time constant of the detector $\tau \approx 2$ μs, we calculate the radio flux intensity arriving from the source: $W_\mathrm{r}/\tau = 0.5 \times 10^{-23}$ W m^{-2} Hz^{-1} (500 Jy). This flux corresponds to the cascade shower energy 10^{22} eV (for $\alpha = 33$). We have already mentioned that 20% of the initial energy of a particle is transformed into the energy of the cascade shower. The actual flux is therefore only 100 Jy. Because the radio flux is approximately proportional to the square of the energy of the original particle, the threshold sensitivity of the radio detector with the UTR-2 antenna can be assumed equal to 2×10^{22} eV.

Observations at the described facility continued for 70 h in winter, mostly at night. The analysis of the recorded pulses pointed to their local origin. Despite the measures taken to block out such pulses, the level of false triggers they caused remained very high. For this reason, the next phase of the experiment was scheduled to run on two antennas of the Uranus system of interferometers, of which UTR-2 is an element.

9. Constraining the UHE neutrino flux based on the data of the Kalyazin Observatory radio telescope

Observations were conducted by the staff of the Pushchino Radio Astronomy Observatory of the Astro Space Center, Lebedev Physics Institute, RAS (PRAO AKTc FIAN) using the 64 m radio telescope based on the antenna of the Special Design Bureau of the Moscow Power Engineering Institute (OKB MEI) (Kalyazin Radio Astronomy Observatory of the FIAN Astro Space Center) in the frequency range from 0.6 to 8.3 GHz [43]. Two channels with mutually orthogonal circular polarizations (LCP and RCP) operated at the frequency of 1.4 GHz, while only one channel with right-hand circular polarization was used at 2.3 GHz. Test observations were carried out at the frequencies 0.6 GHz (LCP) and 4.8 Hz (RCP). For each of the frequencies, the angular width $\Delta\theta$ of the antenna radiation pattern and the bandwidth of the radio receiver path Δv were $\Delta\theta = 25'$, $\Delta v = 8$ MHz at the frequency 0.6 GHz; $\Delta\theta = 11'$, $\Delta v = 50$ MHz at the frequency 1.4 GHz; $\Delta\theta = 7'$, $\Delta v = 120$ MHz at the frequency 2.3 GHz; and $\Delta\theta = 3'$, $\Delta v = 50$ MHz at the frequency 4.8 GHz.

To record short pulses, the system used a trigger circuit with a time resolution of 2 ns based on the four-channel TDS-3034 oscilloscope (Fig. 10). The directions to the maxima of the radiation pattern at all frequencies coincided

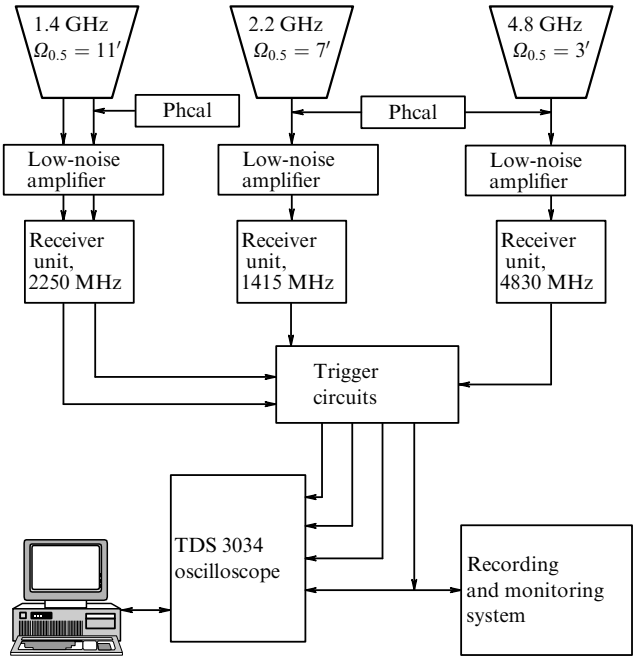

Figure 10. Functional diagram of the radio detector of the Kalyazin Radio Astronomy Observatory. Phcal is the pulse generator for phase calibration.

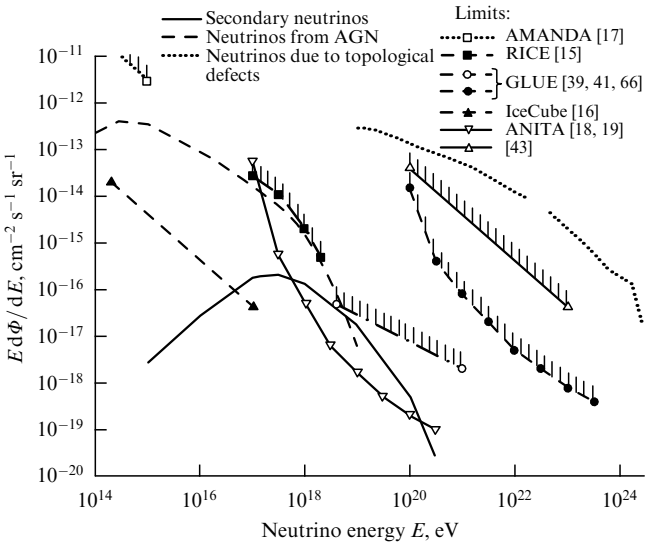

Figure 11. Theoretically predicted neutrino fluxes and the constraints on them experimentally obtained at the Kalyazin Radio Astronomy Observatory. AMANDA — Antarctic Muon And Neutrino Detector Array, RICE — Radio Ice Cherenkov Experiment, IceCube — Ice Cube Neutrino Observatory.

and were aimed at a point on the Moon separated from its center by 14′. The trigger circuit was mounted in the radiometer channel with a frequency of 2.3 GHz. The trigger threshold corresponded to the flux density 13,500 Jy. The relative difference between the propagation time of signals in the receiver units was measured using picosecond pulses fed to the input of low-noise amplifiers (LNAs). The events recorded in the course of observations were analyzed with a view to determine:

(a) the presence or absence of a pulse in one of the channels in the range of 1.4 GHz and its delay relative to the pulse trigger in the trigger channel (2.3 GHz);

(b) clustering of false triggers caused by periodic interferences;

(c) the shape of the pulse in each of the two channels;

(d) differences between pulses in the two channels (LCP and RCP) at a frequency of 1.4 GHz (because the expected useful signal should be linearly polarized, and there should be no differences between pulses).

Many aspects concerning the methodology of this experiment are discussed in [92]. The live observation time was 31.3 h. About 15,000 triggers were processed and no events were found among them that would simultaneously satisfy conditions a–d. Modeling the geometry of interactions of neutrinos in the lunar regolith yielded the upper bound on the UHE neutrino flux. To obtain a more rigorous result than the one in [69], the authors of [92] hypothesized that the slope of the energy spectrum of neutrinos in the relevant energy range has a certain constant value. The exponent of the power-law spectrum in the energy range $10^{20}-10^{23}$ eV was chosen to be -2. Figure 11 plots the theoretically predicted neutrino fluxes and experimentally obtained bounds on these fluxes. The authors of [43] claim, in particular, that the results presented in their paper allow ruling out the spectrum predicted by the model of topological defects at a 95% confidence level.

10. Measurement of UHE neutrino flux at the Westerbork Observatory (Project NuMoon)

10.1 First 10 hours of observation

The latest data obtained at the Pierre Auger Observatory confirmed the presence of a steep decline in the spectrum of cosmic rays at the energy of the GZK cutoff [93, 94]. Above the threshold energy 6×10^{19} eV, cosmic rays can interact with CMB photons, expending their energy on creation of pions at the distance about 10–20 Mps from the source. Pions decay creating UHE neutrinos via the weak interaction. Observation of these neutrinos is of great interest because their flight direction points to sources located at distances greater than 10 Mps, unlike the direction of motion of charged particles, which are deflected in galactic (extragalactic) magnetic fields. Furthermore, cosmic rays from distant sources do not propagate beyond the GZK sphere (10–20 Mps), and hence information about the spectrum of cosmic rays in the source is conserved in the flux of GZK neutrinos arriving from great distances. These facts became decisive in the ideological concept of the NuMoon project [45].

The authors of [45] insist that those who designed experiments like GLUE chose an unreasonably high frequency for observations (2.2 GHz). The only advantage of this choice is, according to parameterization (10.1), the maximized power of the RF pulse. For lower frequencies, the angular width of the radiation pattern is much larger, which is a stronger factor. For an RF pulse to emerge on the lunar surface, the initial particle must necessarily hit the lunar limb and be incident at an angle such that the radio emission does not undergo total internal reflection at the regolith–vacuum interface; in this case, it emerges on the lunar surface without having suffered strong attenuation. It is fairly easy to show, using the principles of geometrical optics, that the entire lunar surface virtually acts as a target if the angular width of the 3D distribution of radio emission is large. It is

assumed in [45] that when the wavelength is of the order of the shower length (several meters), the radiation distribution becomes almost isotropic, and it must be possible to detect RF pulses emitted from virtually anywhere on the Moon. Starting with these assumptions, the authors of [45] concluded that the optimum frequency window for the NuMoon experiment was about 150 MHz.

Project NuMoon explores Cherenkov radio emission pulses caused by cascades of particles with energies above 10^{20} eV [44, 45, 95, 96]. With the results of 100 h of observations, experimenters expect to set new upper bounds on the neutrino flux. The theory and the experimental technique, as well as the results of observations over the first 10 h, are presented in [45]. The Westerbork Synthesis Radio Telescope (WSRT) at the Westerbork Observatory consists of 14 parabolic antennas placed along an east–west line 2.7 km long. Observations were performed in the frequency range 115–180 MHz. The digital analyzer PuMa (Pulsar Machine) II, specifically designed for WSRT for the observation of rotating neutron stars or weak radio sources [97, 98], was used in NuMoon for recording and processing information in this wide range. PuMa II can record and analyze signals in a frequency band up to 160 MHz wide, divided into eight sub-bands (each 20 MHz wide). To conduct lunar observations, two beams were formed, with four radio bands each. The band centers corresponded to the frequencies 123, 137, 151, and 165 MHz. The beams were focused on different areas of the Moon and covered about one third of its surface. This increased the effective area of observations and allowed creating a system of anticorrelations to start the event selection and detection system. A true RF pulse (i.e., a pulse of lunar origin) should be observed in one beam only. In each range, a temporal sequence of data was recorded in several memory clusters with a 40 MHz discretization frequency.

About 1% of the data were left after the first phase of pulse analysis and were transferred to permanent storage. This procedure included the following steps.

(1) The raw data were written into blocks of 20,000 cells and the records were Fourier transformed in order to identify narrow-band radio noise (signals with a continuous carrier frequency). From this array, 200 spectra were stored and normalized to mean values. The narrow lines of radio noise with amplitudes exceeding the average value by a factor of 1.5 and greater were removed.

(2) Pulses of lunar origin undergo dispersion in the terrestrial ionosphere. Therefore, dispersion-caused distortions of radio signals were corrected by taking the total electron content (TEC) of the ionosphere into account. Once radio noise is eliminated from the frequency spectrum, post-dispersion signals of lunar origin can be identified. Therefore, before performing the inverse Fourier transformation and reconstructing pulses in the time domain, a frequency-dependent phase shift was made based on the data of the total electron content in the unit-area vertical column of the ionosphere and the data on the angle of lunar elevation.

(3) It was expected that the sought pulses should have a width narrower than the size of the memory cell (25 ns). In reality, the pulse was spread over several cells, depending on its characteristics. Errors in the value of the TEC used to eliminate pulse distortion due to dispersion extended the pulse even more. For the further analysis, the quantity P_5 was found as the sum of amplitudes over five memory cells and two polarizations, normalized to the mean value of this sum:

$$P_5 = \frac{\sum\limits_{5\,\text{cells}} (P_x + P_y)}{\left\langle \sum\limits_{5\,\text{cells}} (P_x + P_y) \right\rangle},$$

where averaging was performed on 20,000 cells. The indices x and y correspond to signals with mutually perpendicular polarizations.

(4) The maximum was considered established if the value of P_5 was equal to 2.5 in all four frequency bands. A certain difference due to the ionosphere dispersion, between the times of arrival of the peaks at different frequency ranges was regarded as acceptable.

(5) Information from each run in which suitable pulses were found was stored for further processing.

This analysis was performed separately for each of the two beams, but if the pulse was detected in one of the beams only, the input data was stored for both beams and all sub-bands. In order to reconstruct the cut-out radio noise, information about the frequencies of spectral lines was also stored. At the second phase of processing, the removal operation was applied directly to the data itself: pulses wider than eight memory cells and those that were part of a series of consecutive pulses were removed.

To establish triggering thresholds and the effective aperture of the detector, the authors of Project NuMoon used the known theoretical results [56, 57, 95, 99]. We give some of the expressions from [45] for comparison with the results of other theoretical papers. The intensity $F(\theta, \nu, E_s)$ of radio emission by a hadron shower with energy E_s in the lunar regolith is parameterized as [56, 57, 95, 99]

$$F(\theta,\nu,E_s) = 3.86\times10^4 \exp(-Z^2)\left(\frac{\sin\theta}{\sin\theta_{Ch}}\right)^2\left(\frac{E_s}{10^{20}\ \text{eV}}\right)^2 \times\left(\frac{d_{Moon}}{d}\right)^2\left\{\frac{\nu}{\nu_0\left[1+(\nu/\nu_0)^{1.44}\right]}\right\}^2\frac{\Delta\nu}{100\ \text{GHz}}\ [\text{Jy}],$$

$$Z = \left(\cos\theta - \frac{1}{n}\right)\frac{n}{\sqrt{n^2-1}}\frac{180}{\pi\Delta_{Ch}}, \qquad (10.1)$$

where $\Delta\nu$ is the bandwidth of the radio receiver circuit, ν is the central frequency, $\nu_0 = 2.5$ GHz, $d_{Moon} = 0.38\times10^9$ m is the distance to the Moon, and d is the distance from the observer. The Cherenkov angle θ_{Ch} is determined from the ratio $\cos\theta_{Ch} = 1/n$, where $n = 1.8$ is the refractive index of the lunar regolith and θ is the angle between the direction of observation and the shower axis. The final size of the shower and some other factors broaden the edge of the Cherenkov cone to the angular size

$$\Delta_{Ch} = 4.32^\circ\frac{1}{\nu\,[\text{GHz}]}\frac{L\,[10^{20}\ \text{eV}]}{L(E_s)}, \qquad (10.2)$$

where L is the shower length depending on its energy; according to [100], $L(x) = 12.7+2x/3$, $x = \log_{10}(E\,[\text{eV}]/10^{20})$.

Observations were conducted for 10 h 40 min with a single beam corresponding to the coverage of one third of the surface of the Moon, with the central frequency 140 MHz and bandwidth 65 MHz. The bounds on the neutrino flux were recalculated taking into account that no real events were found. This short time was sufficient for refining the upper

bound obtained from the data gathered by the FORTE satellite during almost two years of orbiting Earth. The authors of [45] express the opinion that the upper bound obtained as a result of 100 h of observation will eliminate a number of models associated with topological defects.

The authors of Project NuMoon hoped to conduct the next stage of the experiment in the future, using the radio telescope LOFAR (LOw Frequency ARray) (Netherlands), which was expected to start operations in 2011. LOFAR is a network of low-frequency omnidirectional radio antennas interconnected by a fiber optic line. LOFAR includes two types of antennas operating at different frequencies: a low-frequency (LF) antenna covers the 30–80 MHz band and a high-frequency (HF) antenna covers the 110–240 MHz range. The HF antenna can be used for lunar observations.

Currently, LOFAR consists of 35 stations, each of which contains 48 LF antennas and 96 HF antennas. Half of the stations are located within a 2×2 km^2 square. The total effective area of the antennas is 0.05 km^2. Multiple beams can be formed so as to cover the entire lunar surface with a sensitivity that will be almost 25 times higher than that of the WSRT complex.

10.2 Upper bounds on the flux of UHE neutrinos obtained after 48 hours of observation

The experimental procedure was slightly changed after 10 hours of observation with the WSRT radio telescope. In view of the large number of false trigger pulses, the triggering and event selection criteria were somewhat modified [101, 102]. Prior to recording, the continuously incoming data are split into time blocks, each 0.1 s long. Each block is divided into 200 tracks composed of 20,000 time samples. After cutting out radio noise and removing distortions due to dispersion, and restoring the natural dependence of signals on time via the inverse Fourier transformation, the quantity P_5 is found using the new algorithm:

$$P_5 = \frac{\sum\limits_{5\ \text{samples}} P_x}{\left\langle \sum\limits_{5\ \text{samples}} P_x \right\rangle} + \frac{\sum\limits_{5\ \text{samples}} P_y}{\left\langle \sum\limits_{5\ \text{samples}} P_y \right\rangle}, \tag{10.3}$$

where the average is taken for the entire track. The data undergoes further analysis if $P_5 > 5$. The meaning of this threshold can be understood from (10.3). Because σ^2 is defined as the mean signal power over a certain time interval (we assume for simplicity that it is identical for x and y polarizations), the triggering condition can be written as the inequality

$$\sum_{5\ \text{samples}} P_x + \sum_{5\ \text{samples}} P_y > 25\sigma^2,$$

which expresses the fact that the total power in ten storage cells (five with the x polarization and five with the y polarization) must be greater than $25\sigma^2$, while the mean power is only $10\sigma^2$.

Because a radio signal of lunar origin inevitably travels through the ionosphere, the time shift in HF and LF bands must be

$$\Delta t = 1.34 \times 10^9\ \text{STEC} \left(\frac{1}{\nu_1^2} - \frac{1}{\nu_2^2} \right),$$

where STEC (slant total electron content) is the total electron content in units of 10^{16} m^{-2} and depends on the time of day and elevation angle. This delay in the channels must be zero for terrestrial radio noise. Table 2 in [101] gives more detailed information on the triggering speed and effectiveness of the analysis criteria. The last three columns respectively list the total number of registered pulses, the number of stored pulses for which $S > 23$, and the number of starts in which chaotic

Table 2.

Date	Duration of observation, h	STEC (lower/upper values)	Total number of pulses	Number of pulses with $S > 23$	Number of triggers with $S \geqslant 23$
9 June 2007*	4.7**	11.8/16.6	200,427	49,679	8,943
21 September 2007	2.0	15.6/19.5	668,917	26,812	13,128
13 January 2008	1.3**	18.0/24.3	119,032	6,951	6,001
7 June 2008*	4.25	11.7/17.5	1,961,907	170,672	21,752
8 June 2008*	5.0	9.8/11.3	1,313,378	80,140	12,815
24 August 2008	5.0	3.5/7.5	792,979	36,314	4,029
29 August 2008	3.0	6.5/7.0	563,692	45,214	3,331
29 August 2008	2.0	8.0/8.3	602,049	29,554	4,317
29 August 2008*	4.8	6.5/9.7	1,719,443	96,998	7,425
2 September 2008	5.0	12.8/15.3	880,508	51,329	18,937
16 September 2008	3.75	5.5/11.0	233,192	23,733	6,616
16 September 2008	5.0	5.9/7.2	163,819	20,138	4,841
21 September 2008	4.5	3/3/4.8	244,276	27,388	3,451
21 September 2008*	5.0	4.0/12.8	1,282,457	76,573	9,728
28 September 2008	3.7	10.5/12.0	65,725	67,910	10,345
28 September 2008	3.8	11.6/13.7	622,598	47,580	11,958
14 October 2008	4.5	5.9/9.9	566,611	58,127	6,531
14 October 2008	4.5	5.9/7.4	217,113	30,346	4,165
11 November 2008	3.7	3.5/7.4	941,369	27,160	2,624
Total***	51.1	3.3/24.3	6,681,880	430,646	100,274

* Excluded from analysis due to the exceptional number of raw triggers.
** Only single beam data available.
*** Not counting excluded runs.

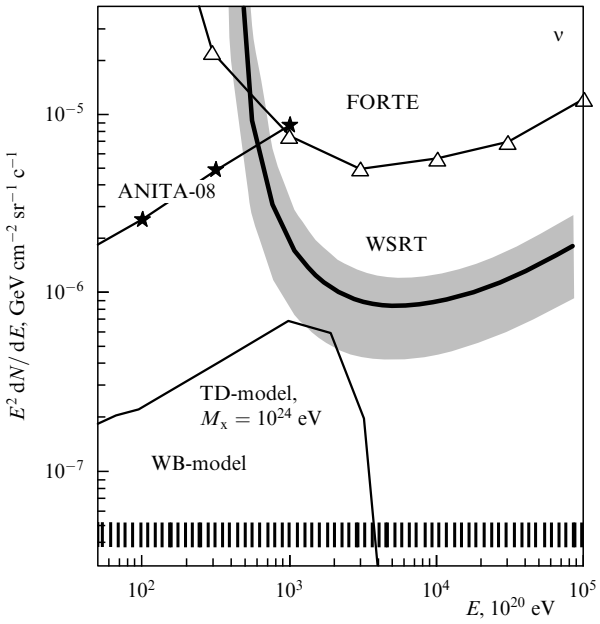

Figure 12. Constraints on neutrino fluxes obtained at the WSRT facility after 48 h of observation.

noise exceeded the estimate $S = 23$. The value of S was found as the sum of the maximum values of P_5 over all four frequency bands:

$$S = \sum_{i=1}^{4} P_{5i}^{\max}. \tag{10.4}$$

Observations during 47.6 h detected no triggers by pulses with the threshold intensity $S_{\text{th}} = 77$ [see (10.4)]. The absence of pulses implies the possibility of setting new upper bounds on the flux of UHE neutrinos. To perform such calculations, we need to know the attenuation of RF pulses in the lunar regolith, the changes in the amplitude and radiation pattern on crossing the interface, and the relation between these changes and the angle of incidence of the neutrino. Using the model in [99], the authors of [101, 102] found constraints on the neutrino fluxes of various energies at a 90% confidence level (Fig. 12). The constraints determined previously were based on the data of the FORTE [69] and ANITA [103] experiments. Figure 12 shows that the WSRT data improved the limits on the particle flux in the energy range $10^{23} - 10^{25}$ eV by almost an order of magnitude. The dark band corresponds to systematic errors caused by the roughness of the lunar surface, the uncertainty of critical energy in the lunar regolith, the uncertainty in the refractive index, etc.

Shown at the bottom of Fig. 12 are the constraints predicted by the Waxman–Bahcall (WB) model [104] and the top-down (TD) model [105] for exotic particles with the mass $M_{\text{X}} = 10^{24}$ eV.

10.3 New upper bounds on the flux of charged particles established by the NuMoon experiment

One of the main features of the methodology in measuring the fluxes of UHE space particles by the WSRT facility is the selection of very low frequencies (115–180 MHz) for the experiment. This LF range permits evaluating the flux of particles causing cascades directly beneath the lunar surface at the location where particles cross the vacuum–regolith interface. These are mostly protons and α-particles. In this case, calculation of the total exposure yielded new results. As mentioned in Section 10.1, the method used in this project was based on the assumption that in observations at low frequencies (115–180 MHz), events of a lunar origin can be detected not only on the lunar limb but also virtually anywhere on the Moon. This section is based on publication [106], which treats specific features of such cascades and establishes constraints on the flux of charged particles. It cannot be ruled out that the facts cited here may cause questions and doubts of the reader. In view of this, Section 12 outlines an alternative point of view on some of the aspects mentioned here.

The authors of [106] ask whether the formation length of radiation due to the excess of electrons in the cascade disk is sufficiently large, and what is to be expected if the shower depth is much shorter than the radiation formation length. In [106], the authors assumed that this problem is irrelevant in the case of a cascade caused by neutrinos, because this cascade invariably occurs far from the surface.

The concept of the length of the (zone of) formation of radiation introduced by Frank [107] consists in the following. Let the observer be placed at some distance from a monochromatic source of radiation with angular frequency ω, moving along a straight line. The distance l' that the source has to cover during the time that the phase changes by π at the observation point is known as the radiation formation length. This length, depending on the observation angle and relative source velocity $\beta = v/c$, is given by $l' = \pi v/\omega(1 - \beta n \cos\theta)$. Practically any source moving along a straight line covers a finite path. The formation length may happen to be longer or shorter than the path, and it can therefore be used to evaluate the radiation intensity. Using this analysis, the authors of [106] concluded that the concept of a formation zone is not applicable to the motion of charged particles in dielectrics.

The second question posed in [106] concerns the depth of the shower: what is the effect produced by a dielectric layer (the regolith) between the interface and the cascade? In the particular case of a horizontal shower, the authors of [106] found an analytic solution of the wave equation for a point-like charge that moves uniformly along a finite segment of the path. It was found that at the error level of 1.5% and shower depth varying from 1 cm to 1 km, this parameter has no effect on the radiation pattern and the intensity (if we neglect absorption in the medium). Using these results, they calculated the upper bound on a flux of charged UHE particles. In the absence of pulses with the typical attributes of lunar origin over the entire time of observation, the model-independent procedure described in [69, 73] can be used, yielding an energy-independent upper bound on the flux of space particles at a 90% confidence level.

Figure 13 plots the upper bounds on the flux of cosmic rays (i.e., charged particles) implied by observations at the WSRT facility [101]. The calculated bounds (curve *1*) were found to be considerably higher than those derived on the basis of the data of the Pierre Auger Observatory (PAO) [108]. The dotted curve *2* shows the model-independent differential PAO-based upper bound. A comparison shows that the limit obtained with the WSRT is lower at higher energies. Curve *3* corresponds to a polynomial extension $E^{-4.3}$ of the PAO results [108]. The broad dark band illustrates the uncertainty in the exponent. Figure 13 also plots the limits that can be anticipated in the near future from the new-generation radio telescopes LOFAR and SKA (Square Kilometer Array).

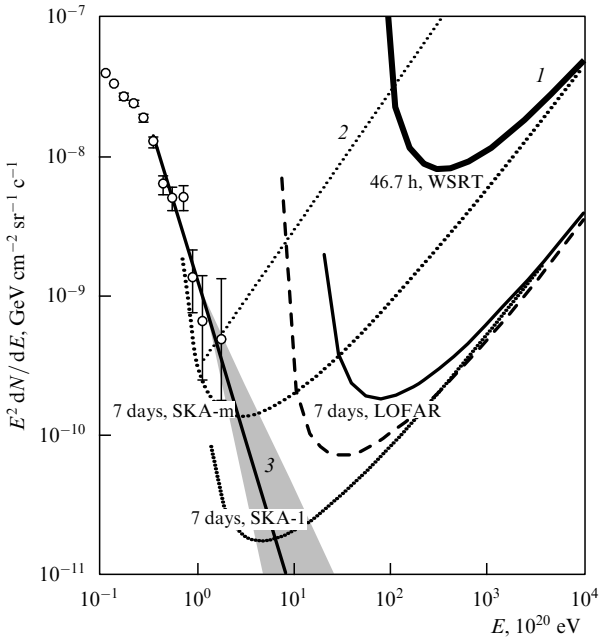

Figure 13. New upper bounds on the flux of charged particles established by the NuMoon experiment.

11. Search for UHE neutrinos in the RESUN experiment

Papers [109, 110] present the results of observations of the lunar surface using the antenna of the radio astronomical complex EVLA (Expanded Very Large Array) (New Mexico, USA). The aim of the experiment was to detect RF pulses from a cascade of charged neutrino particles caused by the interaction of neutrinos with lunar regolith. The experiment RESUN-A — part I of Project RESUN (Radio EVLA Search for UHE (Ultra High Energy) Neutrinos) — was designed for 50 hours of observation. Another part of the project (RESUN-B) was designed for 150 hours of observation. The diameter of the EVLA antenna system is 25 m. RESUN-A used only four antennas out of 27. The angular width of the spatial radiation pattern for each of the antennas was $\approx 0.5^\circ$. Each of the four antennas was an independent detector of pulses and was focused on the eastern part of the Moon, covering about a third of the limb, such that the array was not used as an ordinary interferometer.

The authors of the project, in view of the negative results of previous attempts to identify at least one event of lunar origin, are attempting to rethink the experience of previous research programs and make revisions where they think it necessary, or refine some dogmas of radio astronomical techniques. For example, the cross section of neutrino interaction with the lunar regolith,

$$\sigma(E_\nu) = 1.57 \times 10^{-31} \left(E_\nu\ [\mathrm{EeV}]\right)^{1/3} [\mathrm{cm}^2]\,,$$

was used to calculate the detector aperture. Correspondingly, the average range of neutrinos before the interaction is expressed as $\lambda_\nu = 35.7\ [\mathrm{km}] \times (E_\nu[\mathrm{EeV}])^{-1/3}$ [111, 112]. The authors are convinced that excess electrons in the cascade are the source of radiation and that their motion creates a Cherenkov pulse of the short duration $\tau = L_s/c$, where $L_s(E_\nu) = 1.64 + 0.08 \log(E\,[\mathrm{EeV}])$ [95, 99]. From this, they conclude that the pulse length for the characteristic energy is $\tau = 5$ ns (this seems to be obvious confusion, because the duration of emission for an ultrarelativistic particle not only is nonidentical to the duration of its motion but can even differ from the latter by several orders of magnitude). Further on, the authors of the project base their decision on the conclusions in papers [111, 112]. For example, they use parametric modeling (assuming zero attenuation in the regolith) to calculate the maximum electric field strength ($\theta = \theta_{\mathrm{Ch}}$) in Earth's neighborhood due to cascade particles beneath the lunar surface [64, 111, 112],

$$\mathcal{E}_{\max} = 0.51\left(0.2\,E\ [\mathrm{EeV}]\right) \frac{\nu}{\nu_0} \left[1 + \left(\frac{\nu}{\nu_0}\right)^{\alpha}\right]^{-1}, \qquad (11.1)$$

where ν is the frequency of observation, $\nu_0 = 2.23$ GHz, and $\alpha = 1.23$. At the level e^{-1}, the attenuation length of the electric field is $\lambda_\varepsilon = 18\ \mathrm{m}/(\nu\ [\mathrm{GHz}])$. The process of maximum interest is how the electromagnetic pulse crosses the regolith–vacuum interface. The authors of the project believe, on the basis of the results obtained in [113], that the attenuation of a pulse crossing the interface can be approximated by a constant factor $t_{\|} \approx 0.6$ without introducing significant errors. Therefore, the maximum field strength in free space can be written as $\mathcal{E}_{\mathrm{t}}^{\mathrm{c}}(E_s, \nu) = 0.6\,\mathcal{E}_{\max}^{\mathrm{c}}(E_s, \nu)$, where $\mathcal{E}_{\mathrm{t}}^{\mathrm{c}}$ and $\mathcal{E}_{\max}^{\mathrm{c}}$ are the respective maximum field strengths in the lunar regolith and free space and E_s is the energy of the shower. No more analysis of this very important issue was undertaken. We show in Section 12.4 by what factor the correctly calculated result may differ from this estimate under various conditions.

The issue of the selection of the trigger threshold σ_{t} is important for any detector. This threshold should be set such that the probability of triggering by statistical noise fluctuations during the time of observation be negligible. If we assume that the radio noise amplitude distribution obeys Gaussian statistics and the radio receiver maintains a linear state within the fluctuation voltage, then the probability of sampling a signal σ exceeding σ_{t} is given by

$$p(\sigma > \sigma_{\mathrm{t}}) = \frac{1}{\sqrt{2\pi}} \int_{\sigma_{\mathrm{t}}}^{\infty} \exp\left(-\frac{\sigma^2}{2}\right) \mathrm{d}\sigma = \mathrm{erfc}\left(\frac{\sigma_{\mathrm{t}}}{\sqrt{2}}\right). \qquad (11.2)$$

For example, let $\sigma_{\mathrm{t}} = 6$ (which in fact means that the signal-to-noise ratio is 6), and let the bandwidth of the radio receiver be $\Delta\nu = 100$ MHz. With the pulse length $\tau \approx 1/\Delta\nu$, the number of samples per second is 10^8. According to (11.2), the probability that one sample contains a signal with the amplitude σ_{t} is $1.973 \times 10^{-9} \ll 1$. Therefore, the probability of finding a pulse with the amplitude $\sigma_{\mathrm{t}} = 6$ on average every 5 s is ~ 1. Here, the signal amplitude is given in relative terms: $\sigma = U/U_{\mathrm{me}}$, where $U_{\mathrm{me}} = \sqrt{\langle U^2 \rangle}$ is the standard deviation, which can be found, for example, with the Nyquist formula for the amplitude of thermal noise at the known noise temperature T_{sys} of the system as a whole. The authors assume that $T_{\mathrm{sys}} = 120$ K under the experimental conditions at the frequency 1.45 GHz. For the threshold in the RESUN-A project, the authors selected $\sigma_{\mathrm{t}} = 4.23$. However, the coincidence system significantly lowered the threshold for triggering by thermal noise, and the overall probability of an accidental trigger over 45 h was 0.1.

To calculate the upper bound on the neutrino flux as a function of energy, we need to know the effective detector aperture, which is the sum of the products of the elements of the lunar area $\mathrm{d}s$ and the solid angle $\mathrm{d}\Omega$, and the quantity $\mathrm{d}\Omega$

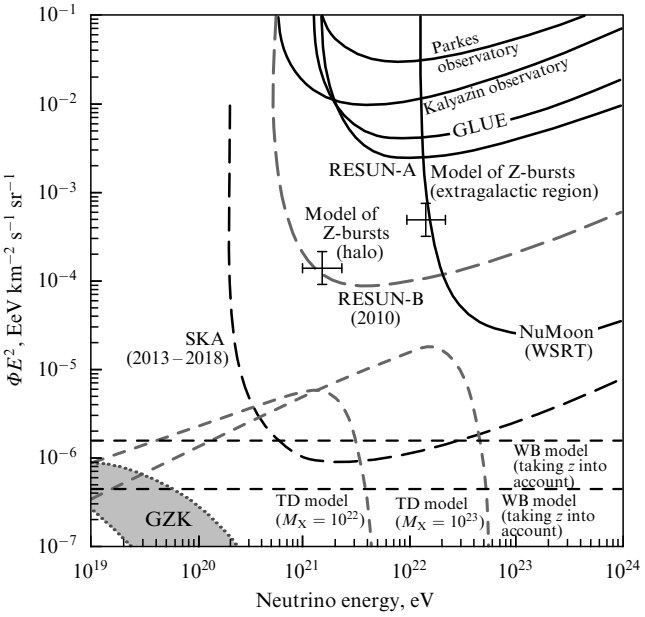

Figure 14. Upper bounds on the neutrino flux obtained in the projects RESUN-A and RESUN-B and calculated for the future SKA-class array.

should be such that the neutrinos within the angle $\Omega + d\Omega$ have the emergence angle on the lunar surface such that the telescope on Earth is covered by the radiation pattern. The calculation must use the fraction of the neutrinos satisfying this condition, which create the cascade disk at the right depth under the lunar surface (10–20 m).

The RESUN-A experiment with 45 h of live observation was completed in February 2008. During this time, no fourfold coinciding events were found at the threshold level higher than 3.98σ. The corresponding upper bound on the isotropic differential neutrino flux at a 90% confidence level in the energy range $21.6 < \log(E\ [\text{eV}]) < 22.6$ was $E^2\,dN/dE < 0.003$ EeV km^{-2} s^{-1} sr^{-1}. This last value is lower than the lowest among the published upper bounds for lunar experiments in this energy range; this data, in particular, confirms the upper bound for GLUE obtained in [1].

Figure 14 shows the upper bound on the neutron flux for RESUN-A as a function of the neutrino energy, together with the previously registered upper bounds reported for other lunar experiments. Also shown are limits for RESUN-B and the future SKA-class array [111, 112] with the effective area 1 km^2, observation frequency 200 MHz, and a 100 MHz bandwidth over 200 hours of observation, as well as the bounds predicted by the TD and WB models, both taking the redshift z into account and ignoring it. The authors of [109] expect that the second part of the RESUN-B project will test the model of Z-bursts, and the SKA project will test the model of topological defects.

The observation of the lunar limb in the RESUN-B experiment [110] was implemented using three subarrays of four antennas each over 25 sessions from August to December 2009. Signals with LC and RC polarizations in two 50 MHz frequency channels centered on frequencies 1385 and 1465 MHz were joined and digitized. No events with a fourfold coincidence were recorded over 200 h of observation with a threshold of 3.9σ. This corresponds to the upper bound on the differential neutrino flux $E\,dN/dE < 1$ km^{-2} y^{-1} sr^{-1} at a 90% confidence interval for isotropic sources with the energy exceeding $10^{21.2}$ eV and $E\,dN/dE < 0.1$ km^{-2} y^{-1} sr^{-1} for the energy $E > 10^{22.5}$ eV. The limit for the isotropic flux is lower by more than an order of magnitude than the previously published upper bounds for lunar searches; it is incompatible with the predicted flux for the model of Z-bursts. The RESUN-B experiment also established, with a 90% confidence level, the bounds on the differential fluxes from 41 active galactic nuclei inside a volume with a 50 Mps radius.

12. Does the absence of RF pulses of lunar origin signify the failure of the radio astronomy method?

"The absence of an RF pulse of lunar origin is a proof of inconsistency of the radioastronomical method." This is how one can formulate the issues with this technique, because quite a few attempts have been made to detect an RF pulse caused by a cascade shower beneath the lunar surface, but every attempt has produced negative results, and it continues to be unclear whether this is natural and inevitable (e.g., because no particles have such a high energy) or it is a consequence of systematic errors and shortcomings of the experiments. A situation of this sort reigned in the 1970s–1980s when at last it became clear that no attempts at implementing the method of radio detection in EAS would bring success, at least in the form available at the time. That field had also started with very optimistic papers [24–26]. However, the situation is different now, and the difference lies in the fact that already in the 1960s it became obvious that radio methods cannot fully compete with the traditional methods of EAS detection, especially with regard to the accuracy of measurements. In essence, the radio method was at best a rather partial alternative to the classical method. Nevertheless, we do not see right now any solid indication that in the energy range of $10^{21} - 10^{23}$ eV, any other technique is emerging for measuring particle fluxes that would compete with the radio astronomical one.

In this connection, it seems that the analysis of possible causes of failure would be especially timely; some of them are discussed in Sections 12.1–12.4.

12.1 Spectrum of RF pulses caused by cascade particles in the lunar regolith

In this section, we consider one of the possible errors connected with selecting the frequency range for the experiment discussed above (see Section 10.1). The choice of the frequency range for the registration of an RF pulse is one of the decisive factors in the radio astronomical method. What we need to know here is the energy spectrum of the RF pulse. Virtually all experiments now known use the results of numerical simulation and parameterization of the radiation intensity of cascade showers [31, 56 58] as a function of the frequency and emission angle. Such an approach can provide a high degree of accuracy if the contribution to radio emission by excess electrons is taken into account correctly. The spectrum of an individual electron on a finite segment of the path (i.e., the projection of the displacement of the electron onto the shower axis) is computed in [31, 56]. After this, field intensities on all tracks are summed; unfortunately, papers [31, 56] do not give more detailed instructions, while the publications cited above offer very little information about their methodology. The parameterization of spectral inten-

sities used for processing measurement results raises doubts, because these functions do not reflect the real processes in the cascade shower.

This path is fraught with errors. We consider this in more detail. Because the track of an individual electron is not infinitely long, the contribution to the emission is determined not only by the Cherenkov radiation but also by bremsstrahlung, because the motion is with acceleration, both at the start and at the end of the path. For example, we can write the expression for the energy spectrum of the radiation emitted by a point-like charge moving uniformly over a finite segment $[-L, +L]$ ($r \gg L$) at a velocity $v \sim c$, assuming that the observer is at a distance $R \gg L$ [114]:

$$|\mathbf{H}| \sim \left| \int_{-L}^{L} \exp\left[\mathrm{i}(\omega t - \mathbf{k}\mathbf{r}_0)\right] [\mathbf{n} \times \mathrm{d}\mathbf{r}_0] \right| \sim \sin\theta \, \frac{\sin(kLp)}{p} ,$$

where $\mathbf{H}$ is the magnetic field strength, $\mathbf{r}_0 = vt$, $\mathbf{n}$ is the unit vector along the direction of observation, and $p = 1 - \beta n \cos\theta$. For the intensity, we finally have

$$I(\omega) \sim H^2(\omega) \sim \left\{ \frac{\sin\left[(\omega/c)\, L(1 - n\cos\theta)\right]}{1 - n\cos\theta} \right\}^2 \sin^2\theta . \tag{12.1}$$

Obviously, if the observer sees the track at the Cherenkov angle (i.e., $1 - n\cos\theta \to 0$), then $I(\omega) \sim \omega^2$ and the energy increases infinitely as the frequency increases. If the algorithm of calculations has not been well designed, the calculated total spectrum may stretch up to very high frequencies. It is possible that the spectrum shown in Fig. 2 is a result of a calculation of just this variety. There is no basis to justify an increase in the intensity when the frequency increases to such high values. It is well known that spectra in real physical conditions typically fall off exponentially at high frequencies.

Any attempt to compute the spectral power of the RF pulse outside the interface yields very crude estimates. The cause of this is the paucity of information on the direction of arrival of particles, the state of the surface of the regolith–vacuum interface at the point where radiation emerges on the lunar surface, the total electron content in a unit-area column of the ionosphere on the surface of Earth, etc. Errors can be very large, and hence accurate knowledge of the cascade function to calculate the intensity of radio emission using software packages does not solve the problem of accuracy, at least at this stage. It would thus appear more expedient to use a radiation model in which the interconnections among all electric and kinematic parameters have a clear physical meaning and allow arriving at easily verifiable quantitative results.

This is indeed how the problem was formulated in [54]. The decision is not based on any hypotheses and does not go beyond the basic concepts of classical electrodynamics. All calculations were performed analytically, and they can be easily checked for grave errors — something that cannot be said about parameterizations (6.1), (6.2), (10.1), and (11.1). True, exponents and coefficients in (6.1) are obtained via numerical calculations (even phase changes with frequency are shown in Fig. 16 in [56]), but in the rest of the cases [i.e., (6.2), (10.1), and (11.1)], these quantities were changed for no apparent reason. The result of this was a set of spectra stretching over hundreds of gigahertz (Fig. 15). It is to become clear in what follows that a real cascade disk cannot produce such spectra in the lunar regolith. Moreover, we

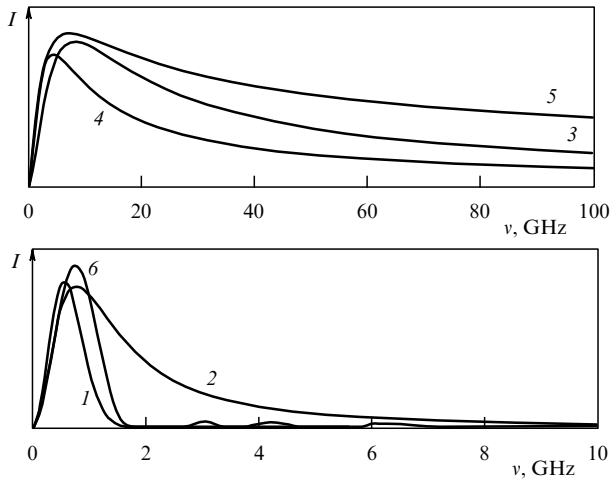

Figure 15. Spectral intensities plotted on different scales: curve *1* — Eqn (12.4), curve *2* — parameterization results in [56], curve *3* — GLUE, curve *4* — NuMoon, curve *5* — RESUN; curve *6* was obtained for a constant cascade function on the segment $[L, -L]$. Weak oscillations in the vicinity of frequencies 3, 4, and 6 GHz refer to curve *6*.

show that the characteristics of the energy spectrum of an RF pulse depend only on the size characterizing the system of charges (e.g., the cascade disk) and are almost independent of the type of the cascade function. Consequently, a highly accurate computation of the cascade function is not of great interest for conducting the experiment and calculating the particle flux, with the exception of situations in which the LPM effect has a strong impact. We demonstrate below that in the last case, too, only the spatial distribution of radiation changes significantly but the spectrum does not (the spectrum, as already mentioned, depends almost completely on the characteristic dimensions of the radiating system of charges). It is much more important to properly single out the segment of calculations that is associated with radiation. From this standpoint, paper [54] seems to be more flexible, because calculations there use the notion of the current modulation by the cascade function, which greatly simplifies the problem by removing the need to calculate the contribution of each individual track. In other words, it is advisable to parameterize the cascade function, not the radiation intensity. The problem of taking the phase into account is then greatly simplified.

A simplified version of the approximation of theoretical calculations in [115, 116] was used in [54] for the cascade function

$$N(E_0, \chi) = \frac{0.31}{\sqrt{\alpha}} \exp\left[\chi\left(1 - \frac{3}{2}\ln\frac{3\chi}{\chi + 2\alpha + 2x}\right)\right] ,$$

where χ is the shower depth in avalanche units and E_0 is the energy cascade. It is then used that in this expression, $x = \ln(r/r_{\mathrm{M}})$ (where r is the distance to the shower axis and $r_{\mathrm{M}} = 9.6\ \mathrm{g\,cm^{-2}}$ is the Moliére radius) is small in comparison with $\chi + 2\alpha$.

A direct check immediately confirms that the cascade function written in the form

$$N(x) = \frac{0.31}{\sqrt{\alpha}} \exp\left[\alpha - \frac{(x - \alpha z_0)^2}{D\alpha z_0^2}\right] , \tag{12.2}$$

where $D = 3$, is not significantly different quantitatively from that in [116] and differs by no more than 20–30% from the cascade function constructed from tabulated values of the parameters $\lambda_1(s)$, $\lambda_1'(s)$, $\lambda_1''(s)$, and $H_1(s)$, where s is the parameter of 'age' of the shower [117]. This approximation [48] gives a good representation of the original function on the segment of the path at whose ends the number of particles in the shower decreases by a factor of about three in comparison with the maximum (i.e., the radiation power on these end segments is reduced by an order of magnitude).

Expression (12.2) is more general than the one used for the same purpose in [54] and covers the energy range $E_0 = 10^{20} - 10^{23}$ eV. In (12.2), the cascade depth x is given in meters, $\alpha = \ln E_0/E_{\rm cr}$, $E_{\rm cr}$ is the critical energy (for the lunar regolith, $E_{\rm cr} = 0.4 \times 10^8$ eV), and z_0 is the avalanche unit of length, also in meters (for the lunar regolith, $z_0 = 0.13-0.14$ m). The quantity D is dimensionless: its value does not affect the number of particles at the maximum of a shower. Direct verification easily confirms that D influences only the effective length of a shower, i.e., establishes a segment on the path of a cascade shower on which the number of particles at its ends decreases by the required factor compared with the maximum.

It is easy to choose D such that the path length calculated using software packages that take the LPM effect into account [95, 99] equals $L(x) = 12.7 + (2/3)x$, where $x = \log_{10}(E\times 10^{-20})$ and the energy shower is given in eV, while the shower length is in radiation units.

The length of the shower in the lunar regolith for the energy $E = 10^{20}$ eV is calculated as ~ 1.7m.

The classical expression for the vector potential (at distances much larger than the size of the source) is

$$\mathbf{A}(\mathbf{r},\omega) = \frac{\mu_0 \exp(\mathrm{i}kr)}{4\pi r}\int_{V'} \mathbf{j}(\mathbf{r}',\omega)\,\exp(-\mathrm{i}\mathbf{k}\mathbf{r}')\,\mathrm{d}V';$$

it involves the spectral current density in the form [54]

$$\mathbf{j}(\omega,\rho) = \mathbf{v}\int_{-\infty}^{\infty}\delta(\mathbf{r}'-\mathbf{v}t)\,\exp(\mathrm{i}\omega t)\,\mathrm{d}q(t,\rho)\,\mathrm{d}t,$$

where $\mathrm{d}q(t,\rho) = \sigma(\rho,t)\,\mathrm{d}s$ is the charge of the disk element $\mathrm{d}s$ separated by the distance ρ from the shower axis and $\mathbf{r}'$ is the radius vector of an arbitrary point in space. The dependence on time is determined by cascade function (12.2). The above expression for the current density is physically more transparent than the sum of field strengths due to each electron track [56]. This creates the problem of taking the phase in each track into account; the error involved can be very high.

The charge distribution on the surface of a disk depending on time and the distance from the center is defined as a Gaussian distribution in the form

$$\sigma(\rho) = \frac{eN(x)}{2\pi\rho_1^2}\exp\left(-\frac{\rho^2}{2\rho_1^2}\right),$$

where ρ_1 is the mean square radius. With this radius, the circle covers about a half of the number of particles in the cascade disk. The time dependence is included in the cascade function ($x = vt$) because the relative number of excess electrons in any area element $\mathrm{d}s$ should be equal to that of the entire disk. The calculation of the spectral field strength $|\mathcal{E}(v,\theta)|$ and the radiation intensity $I(v,\theta) = \sqrt{\varepsilon}\,\varepsilon_0 c\,\mathcal{E}^2$ leads to the following result [54]:

$$|\mathcal{E}(v,\theta)| = \frac{0.15\sqrt{D\pi}\,\exp(\alpha)\,\mu_0 q\,\eta z_0}{2\sqrt{2}\,r}\,v \times \exp\left\{\frac{-\pi^2 v^2}{c^2}\left[D\alpha z_0^2(1-n\cos\theta)^2 + 2n^2\sin^2\theta\rho_1^2\right]\right\} \times \sin\theta\ [\mathrm{V\,m^{-1}\,Hz^{-1}}], \quad (12.3)$$

$$I(v,\theta) = \sqrt{\varepsilon}\,\varepsilon_0 c\left(\frac{0.15\sqrt{D\pi}\,\exp(\alpha)\,\mu_0 q\,\eta z_0}{2\sqrt{2}\,r}\right)^2 v^2 \times \exp\left\{-\frac{2\pi^2 v^2}{c^2}\left[D\alpha z_0^2(1-n\cos\theta)^2 + 2n^2\sin^2\theta\rho_1^2\right]\right\} \times \sin^2\theta\ [\mathrm{J\,m^{-2}\,Hz^{-1}}]. \quad (12.4)$$

Figure 15 plots the spectral intensity expressed on different scales: curve *1* — Eqn (12.4), curve *2* — result of the parameterization in [56], curve *3* — GLUE, curve *4* — NuMoon, and curve *5* — RESUN. The following features can be noted for the sake of comparison. The maximum on curve *1* [i.e., Eqn (12.4)] $I_{1\max} = 1.6 \times 10^{-30}$ J m^{-2} Hz^{-1} is at 0.55 GHz. The values of intensities at the same frequency for curves *2* and *3* are $I_2 = 1.2\times 10^{-30}$ J m^{-2} Hz^{-1} and $I_3 = 1.45 \times 10^{-30}$ J m^{-2} Hz^{-1}. However, for the frequency $v = 2.25$ GHz, which is typically used for observations, the intensities are $I_1 = 1.8 \times 10^{-36}$ J m^{-2} Hz^{-1}, $I_2 = 7\times 10^{-30}$ J m^{-2} Hz^{-1}, and $I_3 = 9 \times 10^{-30}$ J m^{-2} Hz^{-1}, i.e., the difference reaches close to five orders of magnitude. For all curves, the observation angle equals the Cherenkov angle. As the frequency increases, curve *5* remains almost parallel to the horizontal axis, i.e., the spectrum shows almost no falling off toward infinitely large frequencies. Obviously, this cannot be correct. However, this result has not been commented on in any manner in [109].

The authors of [56, 57, 95, 99] are of the opinion that the result of the parameterization (curve *3*) in form (10.1) is reliably justified in the experimental verification of the Askaryan effect, i.e., in the direct detection of radio emission in the laboratory [65]. The results of this particular particle accelerator experiment initiated all subsequent experimental work. Unfortunately, publication [65] gives no details relevant to the evaluation methodology. Nevertheless, important conclusions can be drawn on the basis of the material presented in [65]. The main one is that some results of the experiment were interpreted incorrectly and cannot be directly compared with real conditions.

For example, the functional diagram (Fig. 16) implies that each of the horn antennas was designed to measure only the spectrum of certain parts of the shower that corresponded to the radiation pattern of the horn. According to the description of the experiment, these antennas were oriented at the Cherenkov angle relative to the shower axis. If we rewrite expression (12.1) for the angle at which $1 - n\cos\theta = 0$, i.e., $I(\omega) \sim (\omega/c)^2 L^2 \sin^2\theta$, it becomes apparent that the intensity can increase to very high values as the frequency increases. Exactly the same situation is realized in [65], where the antenna 'sees' only a fraction of the shower. If the horn antenna were placed sufficiently far, such that the entire target could be squeezed inside the pattern, then the spectrum could be expected to resemble the curve for $\theta = 0.8$ in Fig. 2 in [118]. In addition, measuring the transverse dimensions of the shower could also help clarify the interpretation of the results.

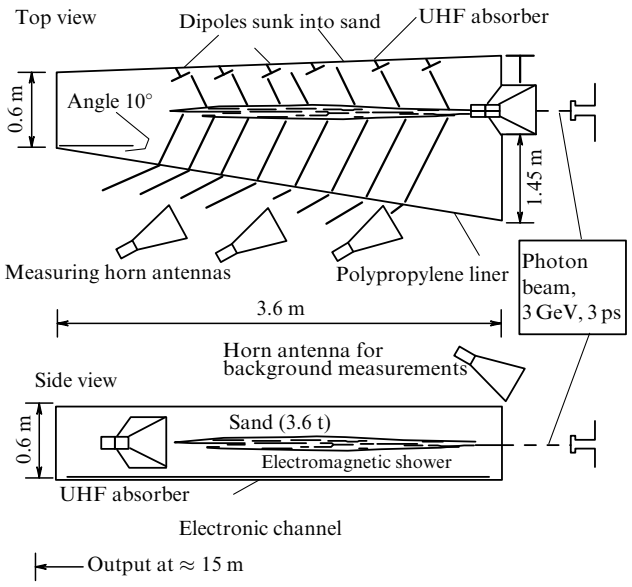

Figure 16. Functional diagram of the experiment for testing the Askaryan effect.

As regards measuring the field strength at the frequency 0.6 GHz, using half-wave dipoles (see the upper part of Fig. 16) at a distance less than the wavelength of the source is at best incorrect, especially when we recall that the size of the source is much greater than both one wavelength and the distance to these dipoles. Parameterized spectra [56, 57, 95, 99] do tend to fall off with increasing the frequency, but they do it very slowly. One suggestion can be that the parameterization in [56, 57, 95, 99] has not been performed with sufficient care and, as a result of possible errors, the spectra shown by curves 3–5 in Fig. 15 fail to decrease at high frequencies. By contrast, two factors are present in the theoretical determination of the spectrum in (12.3) and (12.4), one of them limiting the spectrum at the angles $\theta = \theta_{\mathrm{Ch}} \approx 0.942$:

$$\exp\left(-\frac{2\pi^2\nu^2}{c^2}\,2n^2\sin^2\theta\rho_1^2\right),$$

while the second forms the spectrum at frequencies lower than 0.55 GHz at non-Cherenkov angles:

$$\exp\left[-\frac{2\pi^2\nu^2}{c^2}\,D\alpha z_0^2(1-n\cos\theta)^2\right].$$

For example, if we substitute the data typical for EAS, $E_0 = 10^{17}$ eV, $\theta = 0.024$, $n = 1.0003$, $z_0 = 380$ m, $\rho_1 = 70$ m, and $\alpha = 21.6$, in (12.3) and (12.4), then the maximum of the spectrum is at the frequency 30 MHz, in good agreement with the known published experimental results (see, e.g., [33]). Furthermore, expansion (12.3) yields an expression in the range of low frequencies [118], which coincides with the parameterization in [119,120].

We next comment on how the spectrum depends on the cascade function type in observations at the Cherenkov angle. Estimates given below imply that this dependence is very weak. For example, spectra (6.1), (6.2), (10.1), and (11.1) correspond to observations at the Cherenkov angle. If we set $1 - n\cos\theta = 0$ in (12.4), then all that is left is the factor

$$\exp\left(-\frac{2\pi^2\nu^2}{c^2}\,2n^2\sin^2\theta\rho_1^2\right),$$

which carries no information on the cascade function except the characteristic size of the disk ρ_1. This, however, is merely a hint at complications of this sort. In fact, a simple transformation of (12.4) for a cascade function that is constant on the segment $[+L, -L]$, e.g., for a cubic body moving uniformly at a velocity $v \sim c$, yields the expression

$$I(k,\theta) \sim |\mathbf{B}|^2 = |\mathrm{rot}\,\mathbf{A}|^2 \sim \left|\frac{\sin\left[k(1-n\cos\theta)\,L\right]}{k(1-n\cos\theta)}\,\frac{\sin(kb)}{k}\,\frac{\sin(nkb\sin\theta)}{\sin\theta}\right|^2$$

(with $b = 2 \times 0.06$ m, $L = 0.8$ m, and $1 - n\cos\theta = 0$), which is plotted in Fig. 15 (curve *6*). Small oscillations in the frequency ranges at 3, 4, and 6 GHz refer to curve *6*. We see that curve *6* is very close in nature to curve *1* [see (12.4)], even though the motion over the mentioned finite-length path contains two end segments on which the acceleration is infinite and the spectrum could logically be expected to grow as in (12.1) as the frequency increases. The physical reasons for this are perfectly clear. The pulse duration τ is largely determined, as is the spectrum, by the characteristic dimensions of the body. The pulse duration for the cascade disk in the lunar regolith ($n = 1.7$) with the rms radius $R = 0.06$ m can be evaluated as $\tau \approx (2R/v)\,n\sin\theta_{\mathrm{Ch}} = 0.55$ ns. This is now the quantity that dictates the characteristic spectral composition.

12.2 Dispersion of RF pulses in the terrestrial ionosphere

The phenomenon of dispersion of RF pulses in the terrestrial ionosphere can be used for identifying signals of lunar origin. A signal of lunar origin, being very short before it enters the ionosphere, is strongly distorted after traversing it; its time length increases by an order of magnitude or more. Being sent through a correctly selected dispersion filter, this signal restores its shape and length. An analog dispersion filter is a device that usually resembles a delay line in which the propagation velocity of a harmonic signal depends on the frequency in a way dictated by the electron density distribution in the ionosphere. Unlike signals caused by lunar events, short RF pulses of local origin passing through this filter can only stretch in time. Consequently, the duration of the pulse to be analyzed is crucial for the selection criteria.

If the initial phase is restored in (12.3), we obtain an equation for the component harmonic of the RF pulse with the frequency ω, i.e., essentially an expression for a plane wave with a frequency-dependent amplitude:

$$\mathcal{E}(\nu,\theta) \sim \exp(\mathrm{i}kr - \mathrm{i}\omega t)\,\nu \times \exp\left\{-\frac{\pi^2\nu^2}{c^2}\left[3\alpha z_0^2(1-n\cos\theta)^2 + 2n^2\sin^2\theta\rho_1^2\right]\right\}. \quad (12.5)$$

Propagation through the ionosphere is accompanied, for each of an infinite number of harmonics, by the phase increment $\mathrm{d}\varphi = k\,\mathrm{d}r$ on a path $\mathrm{d}r$. The total phase increment at the point of location of the antenna (except for the term ωt) is

$$\varphi = \int_0^L \frac{\omega}{c}\,n\,\mathrm{d}r = \frac{\omega}{c}\left(L - \frac{40.5}{s\nu^2}\int_0^L N_{\mathrm{e}}(r)\,s\,\mathrm{d}r\right) = \frac{\omega}{c}\left(L - \frac{40.5}{\nu^2}\,\frac{N}{s}\right) = \frac{2\pi\nu}{c}\left(L - \frac{40.5N_1}{\nu^2}\right),$$

where L is the path traversed in the ionosphere, n is the refractive index [see (8.2)], and $N_1 = N/s$ is the number of

electrons in the full column of the ionosphere with the cross section $S = 1$ m^2.

In view of the data in [39], the experimentally determined quantity N_1 takes the characteristic value $N_1 \approx 5 \times 10^{16}$ m^{-2}. To find an expression for the field strength as a function of time at the point of location of the antenna, we need to add all harmonic components and take the new phase into account (with negative and positive frequencies):

$$\mathcal{E}(t,\theta) \sim \mathrm{Im}\left[\int_{-10}^{-\nu_1} \nu \exp\left\{-\frac{10^{18}\pi^2\nu^2}{c^2} \times \left[3\alpha z_0^2(1-n\cos\theta)^2 + 2n^2\sin^2\theta\rho_1^2\right]\right\} \times \exp\left\{-\left[2\pi\nu\left(\frac{6.75}{\nu^2}+t\right)\right]\right\} \mathrm{d}\nu\right] + \mathrm{Im}\left[\int_{\nu_1}^{10} \nu \exp\left\{-\frac{10^{18}\,\pi^2\nu^2}{c^2} \times \left[3\alpha z_0^2(1-n\cos\theta)^2 + 2n^2\sin^2\theta\rho_1^2\right]\right\} \times \exp\left\{-\left[2\pi\nu\left(\frac{6.75}{\nu^2}+t\right)\right]\right\} \mathrm{d}\nu\right], \quad (12.6)$$

where ν_1 is the minimum frequency that allows the expansion $n = \sqrt{1-(\omega_{\mathrm{cr}}^2/\omega^2)} \approx 1 - \omega_{\mathrm{cr}}^2/2\omega^2 = 1 - 40.5 \times N_{\mathrm{e}}\ [\mathrm{m}^{-3}]/(\nu^2\ [\mathrm{Hz}^2])$, with $\omega_{\mathrm{cr}}^2 = N_{\mathrm{e}}\, e^2/\varepsilon_0 m_{\mathrm{e}}$. For a typical average electron concentration $N_e \sim 10^{11}$ m^{-3}, we find $\omega_{\mathrm{cr}} \approx 3$ MHz, and hence the frequency ν_1 can be chosen to be 10 MHz, for example. Frequency and time in formula (12.6) are given in gigahertz and nanoseconds. The upper and lower integration limits (10 GHz) were selected according to the condition that increasing them further does not result in any appreciable changes in numerical integration. Figures 9a and 9c show the initial pulse of field strength (12.3) under observation at the Cherenkov angle ($\theta = 54°$) and the same pulse after passing through the ionosphere. Figures 9b and 9d show radio signals that were recorded when observing the pulse shown in Fig. 9a, at an angle of 70°. The length of the initial pulse (FWHM) observed at a 70° angle increased by a factor of five, while the field strength decreased 20-fold. After passing through the ionosphere, the length of the dispersed pulse increased to 1 ms.

To find the time dependence of the field strength for parameterizations (6.1), (6.2), (10.1), and (11.1), we need to know the phase–frequency characteristics for these expressions. Unfortunately, they are not given in the cited papers, with the exception of [56], where this dependence is given in graphic form within the interval 0–10 GHz, which is not enough for a correct recovery of the signal.

12.3 Violation of coherence of radio emission caused by inhomogeneities in the lunar regolith

We know that the Cherenkov angle and the total internal reflection angle are complementary to the right angle, and this fact imposes a strong constraint on the potential of the radioastronomical method. The intensity of radio emission above the lunar surface is high enough only when a particle travels from the regolith into the vacuum. For this, a particle has to pass through the mass of lunar matter and initiate a cascade in the immediate vicinity of the surface (see Fig. 4). Neutrinos are the best particles for this process. The necessary condition is that this interaction take place at a depth of no more than 10–15 m, because otherwise the radio emission of the cascade shower would be too strongly attenuated by absorption into the lunar matter. We also know that the lunar regolith results from crushing, mixing, and sintering lunar rocks exposed to impacts of meteorites and micrometeorites. Consequently, its aggregate state is very inhomogeneous. This layer may incorporate both large and small aggregations with different refractive indices, e.g., due to fluctuations in the density of rock. At high frequencies, of the order of 2–3 GHz, typical for applications of the radioastronomical method, this can lead to the destruction of coherence of the radiation even in the case of a relatively weak inhomogeneity of the medium.

Fluctuations of the refractive index in a layer of thickness d cause delays or advances of pulses (in comparison with the case of homogeneous media); to simplify the calculation, we assume that the refractive index is a random function of z' (z' is in the plane of the layer). The time delay (or advance) of a pulse in such a layer is equivalent to a change in the optical path length from an elementary source of length $\mathrm{d}z'$ to the observer [49]. The use of geometrical optics in these estimates is justified by the shortness of wavelengths used in radioastronomical methods. For example, at 2–3 GHz, the wavelength in the regolith is $\lambda \sim 6-9$ cm.

To determine how the intensity depends on the frequency and emission angle, it is convenient to use the model in which the size of the shower disk is infinitely small. From (12.5), we then obtain the radiation field at the observation point by introducing a phase factor $\exp(\mathrm{i}kdf(z'))$ that takes the thickness of the inhomogeneous layer $d = 10$ m into account. The function $f(z')$ is found in accordance with the values of the refractive index $n = f(z')$ selected by a random number generator in the interval from 1.69 to 1.71. With the parameters selected for the lunar regolith, the shower length is 2–3 m, and hence the maximum lies in the range $4.5 < z' < 5.5$. Consequently, it is sufficient to integrate over the elementary source in the range 0–10 m. Finally, we find that at large distances from the shower,

$$\mathcal{E}(\mathbf{r},\omega) \sim \mathbf{j}\,\frac{\exp(\mathrm{i}kn_0 r)}{r}\; ck\sin\theta \times \int_0^{10} \exp\left[-\frac{(z'-\alpha z_0)^2}{3\alpha z_0^2} - \mathrm{i}kz'(1-\beta n_0\cos\theta) + \mathrm{i}kdf(z')\right]\mathrm{d}z',$$

where $\beta = v/c \approx 1$. Figure 17 plots diagrams of the differential intensity $I(k,\theta)$ for different values of the wave number k ($k = 1$ corresponds to 50 MHz). The scale is identical on all plots. We see that there is virtually no increase in the intensity with increasing the frequency. It is of interest to compare the initial intensities. For the indicated values of k (10, 20, 30, 40, and 50) and $d = 0$ (i.e., with no inhomogeneity), the radiation flux density increases almost in proportion to k^2 [see (12.4) for $\rho_1 = 0$] and equals 1150, 4600, 10,400, 18,400, and 28,800 J m^{-2} Hz^{-1}. The curve of intensity as a function of angle θ (radiation pattern) for $d = 0$ is a unipolar pulse with the angular width at half-maximum equal to (for the respective values of k) 7.1°, 3.42°, 2.54°, 1.76°, and 1.41°.

Figure 17 shows that for $d = 10$ and $i = 100$, the increase in intensity with increasing k almost stops near $k = 10-15$, and the intensity does not exceed ~ 2000. The shape of the pulse is then completely destroyed (for the shape of the initial pulse, see Fig. 20, curve *2*), and the spatial distribution of radiation expands to an angle exceeding 60°.

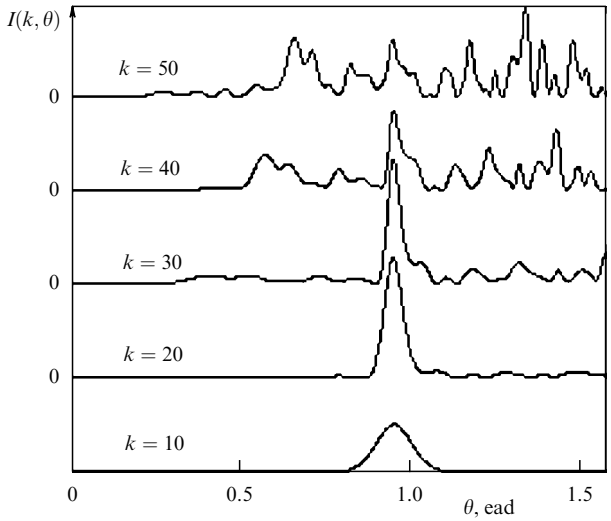

Figure 17. Differential intensities $I(k,\theta)$ of radiation as a function of the observation angle at the point of emergence from the inhomogeneous layer for different values of the wave number. The scales are the same for each curve.

These estimates indicate that heterogeneity can dramatically affect the formation of an RF pulse caused by a cascade shower in the lunar regolith. The fluctuation of the refractive index $\Delta n = \pm 0.01$, used in [49], is unlikely to match a real distribution. However, this result gives reason to suspect the role of some factors that continue to make it impossible to reliably detect even a single RF pulse due to a UHE particle. This issue has become a priority in view of the upcoming projects of lunar orbiters equipped with a particle radio detector on board. To avoid errors in such programs, it should be possible to carry out observations at relatively low frequencies. The frequency band no higher than $\sim 500-600$ MHz would seem to be optimal. As an additional argument, we can point to the data in [19], which show that the maximum of the radiation falls into precisely this interval.

We conclude this section with the following remarks. It may seem that electromagnetic beam scattering by inhomogeneities in the regolith is not without its positive sides. For instance, we consider a cascade induced by particles (e.g., neutrinos) propagating at an angle of a few degrees to the surface of the Moon in the vacuum–regolith direction. Even for $k = 10$ (~ 500 MHz), with a perfectly smooth surface and completely homogeneous layer, a large fraction of the electromagnetic wave experiences total internal reflection, and only a very small fraction of radiation emerges from below the surface. In the case of scattering by inhomogeneities, no rays whose incidence angle is greater than the Cherenkov angle $\theta_{\rm Ch} \approx 0.94$ undergo total internal reflection, and the radio signal can be recorded if the observation angle is favorable. However, the scattering process reduces the density of the radiation, which in turn leads to a decrease in the signal amplitude across the antenna load. This decrease can be estimated in view of the above results. For example, we choose a frequency characteristic of the radioastronomical method, ~ 2 GHz ($k = 40$). According to calculations, the angular 'thickness' of the cone is $\Delta\theta_0 \approx 1.76^\circ = 0.031$. It corresponds to the solid angle $\Delta\Omega_0 = 2\pi\,\Delta\theta_0 \sin\theta_{\rm Ch}$. Figure 17 shows that the angle $\Delta\theta_0$ increases due to inhomogeneities, to $\Delta\theta \approx 1$, and the solid angle corresponding to it is $\Delta\Omega \approx 1.8\pi$. Clearly, the flux density decreases by the factor $\Delta\Omega/\Delta\Omega_0 \approx 36$ and the signal amplitude by a factor of about six. The data given above imply that, for example, for the wave numbers $k = 40$ and $k = 10$, the ratio of the emission intensities is $I_{40}/I_{10} = 18400/1150 = 16$. This means that the transition from the observation frequency 500 MHz to 2 GHz increases the maximum intensity by a factor of 16 and that scattering by inhomogeneities reduces this value by 36. These simple geometric estimates lead to the conclusion that power reduction by approximately half (36/16) is completely compensated by the broadening of the radiation pattern by a factor of $1/0.031 \approx 32$. However, these optimistic calculations ignore the fact that the shower is treated in [49] as a material point — a feature that was not important for the principal conclusions of the paper. In a realistic case, the intensity at a frequency of 2 GHz is lower by approximately five orders of magnitude than at 500 MHz; this follows from the estimates in [54]. Therefore, the effect of increasing the probability of pulse detection in the case of scattering is essential only at very high energies, perhaps above 10^{25} eV.

12.4 Interaction between cascade shower radio emission and the vacuum–regolith interface

Attempts to record an RF pulse from a cascade caused by a UHE particle moving in the lunar regolith (see Sections 4–11) have failed to bring positive results for reasons remaining unknown. In all likelihood, there are several causes, and the negative result is in the end a consequence of superposed theoretical and experimental errors. We here see a stimulus for seeking the factors that would explain why such events continue to be undiscovered. We consider the attenuation of the radiation flux density owing to its transmission through the lunar regolith–vacuum interface.

The cascade disk forms in the immediate vicinity of the interface; the wavefront of the RF pulse is not planar: it forms as a result of coherent summation of elementary (point-like) sources of emission. The radio emission from a cascade shower that propagates in close proximity to the lunar surface was analyzed in [48] in order to clarify the influence of the regolith–vacuum transition region on the radiation field outside lunar regolith. The results in [48], which we discuss below, refer to the case of neutrinos emerging from the regolith onto the lunar surface, and to the case where a particle crosses the interface on its way from the vacuum into the regolith layer. This can be a neutrino or a charged particle.

We consider the main stages in solving this problem. The first step is to find the vector potential of the electromagnetic field of the cascade shower tilted at the angle $\theta = \pi/2 \pm \Delta\theta$ to the normal, taking the real transverse and longitudinal dimensions of the shower into account. This model assumes that the system of currents is caused by the motion of the charged disk at a speed that is nearly equal to the speed of light in the vacuum. The disk thickness in the lunar regolith is several millimeters, i.e., much smaller than the wavelengths considered here, and can thus be treated as infinitely small. The transverse size of the disk (its mean-square diameter) is close to 10–12 cm, and can therefore be taken into account when determining the field potential. The disk is then split into elementary platelets; we note that all the elements of this partition are coherent sources. Each point of the cascade disk is a source of spherical waves that can be expanded into plane waves using conventional methods. It is therefore possible to apply Fresnel's formulas for the calculation of the amplitudes

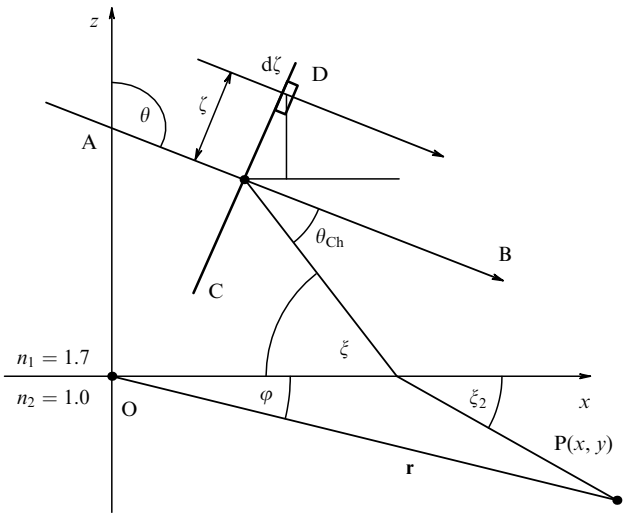

Figure 18. A cascade shower (AB) beneath the lunar surface (OX). D is one of the horizontal stripes (view of the transverse cut by the plane $y = 0$) on which all points emit with identical phases.

of refracted waves. These waves should be summed up at the observation point, taking their phases into account.

The ultimate goal in [48] was to find how the intensity of the refracted waves depends on the relative orientation of the cascade shower with respect to the interface. To achieve this, the angular interval $-0.3 < \Delta\theta < +0.3$ was split into 60 equal sub-angles, and for each sub-angle, the maximum emission intensity was determined from the cascade at the observation point at a distance much greater than the shower size. Then the results were plotted using the cubic interpolation of this data.

The normal to the surface in Fig. 18 points inward, into the Moon, and the direction of motion of neutrinos AB (and of the cascade disk CD) is at the angle $\theta = \pi/2 \pm \Delta\theta$ to it, where $\Delta\theta$ changes within $-0.3 < \Delta\theta < 0.3$. For $\theta = \pi/2 + \Delta\theta$, the cascade shower propagates through the regolith near the surface in the direction of the interface with the vacuum at a small angle $\Delta\theta$ to the horizon (Fig. 8 illustrates this case). The angles $\theta = \pi/2 - \Delta\theta$ correspond to a shower caused by a particle (e.g., a proton) that travels from the vacuum into the regolith and causes a cascade shower in the immediate vicinity of the point of crossing the interface.

The z axis coincides with the normal; its positive direction is the direction from the vacuum to the regolith. The xy plane is the lunar surface. The observation point $P(x, z)$ is in the vacuum in the xz plane, and its radius vector $\mathbf{r}(x, y, z)$ is at an angle φ to the x axis. When integrating over space, the coordinates of an arbitrary point in the medium are denoted by (x', y', z'). The excess charge of the shower with the energy $\sim 10^{21} - 10^{23}$ eV can be approximated in the vicinity of the maximum of the shower by formula (12.2).

The method used for taking the actual size of the cascade disk into account was the one employed in [54]. All points of the disk are coherent sources, and because the longitudinal size of the disk is much shorter than the transverse size, the phase difference at the observation point is dictated not by the thickness of the disk but by its transverse size. A narrow $\mathrm{d}\zeta$-wide strip parallel to the xy plane was selected on the disk; it was located at a distance ζ from the disk center (see Fig. 18). The current density produced by the motion of a narrow horizontal strip of the disk is a δ-function, i.e., it is in fact assumed that a $\mathrm{d}\zeta$-wide horizontal strip on the disk is a point-like charge q_b located in the xz plane. This assumption is justified by the fact that for any element of a horizontal strip (in fact, for point-like charges on it), the expansion of the potential with respect to plane waves is the same when written in the coordinates (x, z), while the phase difference on the path to the infinitely remote observer is almost exactly zero. Consequently, summing plane waves from each element of such a strip amounts to adding amplitudes with identical phases.

The equation of a straight line in the xz plane along which the center of the selected strip (i.e., the charge q_b) moves is written as

$$\mathbf{r}_0(\zeta, t)\colon\ x_0'(\zeta, t) = x_1 + vt\sin\theta - \zeta\cos\theta\,,$$

$$z_0'(\zeta, t) = z_1 + vt\cos\theta + \zeta\sin\theta\,.$$

The current density corresponding to this strip is then $\mathbf{j}(\mathbf{r}', \zeta, t) = \mathbf{v}q_\mathrm{b}\delta(\mathbf{r}' - \mathbf{r}_0(\zeta, t))$, where vt is the path covered by the disk over time t, $\mathbf{v}$ is the velocity of the cascade disk, $|\mathbf{v}| \approx c = 3 \times 10^8$ m s^{-1}, and the point (x_1, z_1) defines the position of the 'origin' of the shower.

The charge on each strip is modulated by the cascade function and can therefore be written in the form

$$q_\mathrm{b} \sim \frac{N(t)}{2\rho_1^2}\,\frac{\zeta\,\mathrm{d}\zeta}{\sqrt{\pi}}\left(\frac{\zeta^2}{2\rho_1^2}\right)^{-1/2}\exp\left(-\frac{\zeta^2}{2\rho_1^2}\right) = N(t)\,F(\zeta)\,. \tag{12.7}$$

If (12.7) is integrated over ζ from $-\infty$ to $+\infty$, we obtain the total charge on the disk at an arbitrary time. The Fourier component of the current density then has the form

$$\mathbf{j}(\mathbf{r}', \zeta, \omega) = \mathbf{e}_v\int_{-\infty}^{\infty} q_\mathrm{b}(\zeta, t)\,\delta\big[\mathbf{r}' - \mathbf{r}_0'(\zeta, t)\big]\exp(\mathrm{i}\omega t)\,\mathrm{d}t\,,$$

where $\mathbf{r}'$ is the radius vector of an arbitrary element of space $\mathrm{d}V'$ and $\mathbf{e}_v$ is the unit vector along the shower axis.

We can now set $x_1 = 0$ because a displacement of the shower parallel to the x axis can only change the phase at the point of observation but not the form of the expansion of a point-like source in plane waves. Then the Fourier component of the current density becomes

$$\mathbf{j}(\mathbf{r}', \zeta, \omega) = \mathbf{e}_v\int_{-\infty}^{\infty} q_\mathrm{b}(\zeta, t)\,\delta\big[x' - (vt\sin\theta - \zeta\cos\theta)\big]$$

$$\times\,\delta\big[z' - (z_1 + vt\cos\theta + \zeta\sin\theta)\big]\exp(\mathrm{i}\omega t)\,\delta(y')\,\mathrm{d}t\,.$$

The argument of the second δ-function vanishes for $t = (z' - z_1 - \zeta\sin\theta)/v\cos\theta$. Therefore, integration over time gives

$$\mathbf{j}(\mathbf{r}', \zeta, \omega) \sim \mathbf{e}_v\,\frac{F(\zeta)}{\cos\theta}\exp\left[-\frac{(z' - z_1 - \zeta\sin\theta - \alpha z_0\cos\theta)^2}{3\alpha z_0^2\cos^2\theta}\right]$$

$$\times\,\delta\big[x' - (z' - z_1 - \zeta\sin\theta)\,\tan\theta + \zeta\cos\theta\big]\,\delta(y')$$

$$\times\exp\left[\frac{\mathrm{i}\omega(z' - z_1 - \zeta\sin\theta)}{v\cos\theta}\right],$$

where $F(\zeta) = \big[\mathrm{d}\zeta/(\rho_1\sqrt{2\pi})\big]\,\exp\big[-(\zeta^2/2\rho_1^2)\big]$ [see expression (2)].

The spectral component of the vector potential of any system of currents, taking its self-retardation into account,

can be written as

$$\mathbf{A}(\mathbf{r},\omega)=\frac{\mu_0}{4\pi}\int_{V'}\frac{\mathbf{j}(\mathbf{r}',\omega)}{R}\exp\left(\mathrm{i}knR\right)\mathrm{d}V', \tag{12.8}$$

where $k=\omega/c$, $R=|\mathbf{r}-\mathbf{r}'|$, n is the refractive index of the regolith, and $\mathbf{r}$ is the radius vector of the observation point. The integration in (12.8) is in fact carried out over the region in which currents are nonzero. After the appropriate calculations, we arrive at the following expression for the spectral intensity:

$$J(r,k,\varphi)\sim\left|\int_0^{10}\int_{-0.2}^{0.2}\chi(x',\theta,\zeta,k)[\nabla\psi_1\times\mathbf{e}_v]\,\mathrm{d}x'\,\mathrm{d}\zeta\right|^2,$$
$$\psi_1=\frac{\exp\left(\mathrm{i}kn_1R_0'\right)}{R_0'}, \tag{12.9}$$

where

$$\chi(x',\theta,\zeta,k)=\frac{1}{\sin\theta}$$
$$\times\exp\left[-\frac{\zeta^2}{2\rho_1^2}-\frac{\left[(x'+\zeta\cos\theta)-\alpha z_0\sin\theta\right]^2}{D\alpha z_0^2\sin^2\theta}+\frac{\mathrm{i}k(x'+\zeta\cos\theta)}{\sin\theta}\right], \tag{12.10}$$

$$R_0'(\mathbf{r},\theta,\zeta)=\sqrt{(x-x')^2+\left[z-\left(\frac{x'}{\tan\theta}+z_1+\frac{\zeta}{\sin\theta}\right)\right]^2}. \tag{12.11}$$

If we set $\theta=\pi/2$, $n_1=n_2=1.7$, and $r\sim100-200$ m in (12.9)–(12.11) and take into account that $x=r\cos\varphi$ and $z=-r\sin\varphi$, then direct verification demonstrates that for different values of k, the spectral intensity is numerically identical to the results obtained in [54] for $D=3$:

$$J(\varphi,k)\sim|\mathbf{B}|^2=|\mathrm{rot}\,\mathbf{A}|^2$$
$$\sim k^2\exp\left[-\frac{3}{2}\,\alpha k^2z_0^2(1-n\cos\varphi)^2-k^2n^2\rho_1^2\sin^2\varphi\right]\sin^2\varphi\,. \tag{12.12}$$

We should keep in mind that the cascade function in [54] is more primitive, because the quantity $\alpha=10$ involved in it corresponds to only one energy value $E_0=10^{22}$ eV. Here, α is expressed in terms of the cascade energy as $\alpha=\ln E_0/E_{\mathrm{cr}}$ and for $E_0\sim10^{22}$ eV and $E_{\mathrm{cr}}=0.4\times10^8$ eV takes the value $\alpha\approx33$. Therefore, the quantity $\alpha^2/2=50$ in [54] coincides with the quantity $D\alpha/2\approx50$ in [48] and, consequently, the maximum of the spectrum is also found at the frequency $\sim$ 500–600 MHz.

If we assume that the value of $x'\cot\theta+z_1+\zeta/\sin\theta$ in (12.9)–(12.11) is negligible because it is small compared to the distance to the observer (and keep it only in the expression for the phase) and integrate over ζ and x' from $-\infty$ to $+\infty$, then (12.9) becomes identical to (12.12).

We next expand the field with intensity (12.9) in plane waves. Each of the point-like sources $\psi_1(x,z)=\exp\left(\mathrm{i}kn_1R_0'\right)/R_0'$ has the amplitude $\chi(x',\theta,k,\zeta)\,\mathrm{d}x'$; in the second medium, the field of a point-like source ψ_1 is expressed as a sum of plane waves, in accordance with the procedure in [121–123]:

$$\psi_2(x,z)=-\frac{\mathrm{i}kn_1n_2^2}{n_1^2}\int_{\pi/2}^{\mathrm{i}\infty}t_{\|}\exp\left(\mathrm{i}kn_1z_{01}\sin\xi-\mathrm{i}kn_2z\sin\xi_2\right)$$
$$\times J_0(kn_1x\cos\xi)\,\cos\xi\,\mathrm{d}\xi\,,$$

where ξ is the angle between the ray emerging from the point (x',z') and the x axis, $z_{01}=x'\cot\theta+z_1+\zeta/\sin\theta$,

$$t_{\|}=2n_2^2\left(n_2^2\sin\xi+\sqrt{n_1^2(n_2^2-n_1^2\cos^2\xi)}\,\right)^{-1}\sin\xi\,,$$

is the Fresnel coefficient, $J_n(z)$ is the Bessel function of order n, and $\sin\xi_2=\left[1-(n_1/n_2)^2\cos^2\xi\right]^{1/2}$ (see Fig. 18).

The spectral density of the total energy (energy per Hz and per m^2 over the entire duration of emission) in the second medium, $I_2(\varphi,\theta,k)$, is proportional to the squared sum of the amplitudes of elementary sources taking the phase lead into account. Similarly to (12.9), the field induction in the second medium $\mathbf{B}_2=\mathrm{rot}\,\mathbf{A}_2$ is given by

$$\mathbf{B}_2(\mathbf{r},\omega)\sim\int_0^{10}\int_{-0.2}^{0.2}\chi(x',\theta,\zeta)\,[\nabla\psi_2\times\mathbf{e}_v]\,\mathrm{d}x'\,\mathrm{d}\zeta'\,.$$

But because

$$\left|\nabla\psi_2\times\mathbf{e}_v\right|\sim\left|(\mathbf{e}_x\,b_1+\mathbf{e}_z\,b_2)\times(\mathbf{e}_x\sin\theta+\mathbf{e}_z\cos\theta)\right|$$
$$=\left|[\mathbf{e}_z\times\mathbf{e}_x]\,b_2\sin\theta+[\mathbf{e}_x\times\mathbf{e}_z]\,b_1\cos\theta\right|$$
$$\sim b_2\sin\theta-b_1\cos\theta\,,$$

we finally obtain

$$I_2(r,\varphi,\theta,k)\sim\left|B_2(r,k,\theta,\varphi)\right|^2$$
$$\sim\left|\int_0^{10}\chi(x',k,\theta)(b_2\sin\theta-b_1\cos\theta)\,\mathrm{d}x'\right|^2, \tag{12.13}$$

where

$$\frac{\partial\psi_2(x,z)}{\partial x}=b_1$$
$$=\mathrm{i}k^2n_2^2\int_{\pi/2}^{\mathrm{i}\infty}t_{\|}\exp\left(\mathrm{i}kn_1z_{01}\sin\xi+\mathrm{i}kn_2\,r\sin\varphi\sin\xi_2\right)$$
$$\times J_1\left[kn_1(r\,\cos\varphi-x')\cos\xi\right]\cos^2\xi\,\mathrm{d}\xi\,,$$

$$\frac{\partial\psi_2(x,z)}{\partial z}=b_2=-\frac{k^2n_1\,n_2^3}{n_1^2}$$
$$\times\int_{\pi/2}^{\mathrm{i}\infty}t_{\|}\exp\left(\mathrm{i}kn_1z_{01}\sin\xi+\mathrm{i}kn_2\,r\sin\varphi\sin\xi_2\right)$$
$$\times J_0\left[kn_1(r\cos\varphi-x')\,\cos\xi\right]\sqrt{1-\left(\frac{n_1}{n_2}\right)^2\cos^2\xi}\,\cos\xi\,\mathrm{d}\xi\,,$$

$z_{01}=x'\cot\theta+z_1+\zeta/\sin\theta$ and we use the substitution $x\to r\cos\varphi$, $z\to-r\sin\varphi$.

Two cases corresponding to the shower inclination angle $\theta=\pi/2\pm\Delta\theta$ need to be considered to present the results of calculations. These results were analyzed for two characteristic frequencies: $\nu\approx150$ MHz ($k=3$) and $\nu\approx500$ MHz ($k=10$). The upper bound ($k<10$) reflects the inexpediency of using the range of high frequencies in view of the low emission intensity [54]. Incidentally, the same conclusion was drawn in project [45] (where the working frequency range was

115–180 MHz), in which the authors pointed directly to the fact that the designers of GLUE-like experiments selected an unreasonably high frequency for observation (2.2 GHz).

I. $\theta = \pi/2 + \Delta\theta$. This case is encountered, for instance, when recording events with an energy of $10^{21} - 10^{22}$ eV in which neutrinos, having covered a path l (of about several dozen km) beneath the lunar surface can, with a certain probability, generate a cascade at a depth of 10–15 m. There are reasons to believe that in this instance, an RF pulse caused by such a cascade can be accessible to observation by radio telescope [35]. The angle between the trajectory and the lunar surface is $(\Delta\theta)_{\rm M} = \theta - \pi/2 \approx l/2R_{\rm M}$. For example, for the characteristic distance $l \approx 70$ km (the so-called interaction length for $10^{21} - 10^{22}$ eV neutrinos), the angle is $(\Delta\theta)_{\rm M} \approx 1^\circ$. At the observation frequencies $\nu \approx 2$ GHz ($k = 40$), which are commonly used for observation [38 46, 118], the half-width of radiation pattern (11) in homogeneous media is approximately 1.9°, and hence is nearly equal to $2(\Delta\theta)_{\rm M}$ (for $\alpha = 33$, which corresponds to the energy $E_0 = 10^{22}$ eV). The conclusion that in this case, the height of the intensity maximum of radiation that emerges from under the surface should be close to a similar maximum in a uniform medium is integrated into the techniques composing the radioastronomical method.

Figure 19a, on an identical scale, plots the maximum flux densities $I_{\max}$ in a beam arriving at the surface for showers directed in the regolith toward the regolith–vacuum interface at the angle $\theta = \pi/2 + \Delta\theta$ to the normal (for $k = 10$ and $k = 3$). These results significantly refine the conclusions accepted earlier. First, it is meaningless to increase frequency to values larger than $\nu \approx 500$MHz ($k = 10$). This is implied by the presented evaluations and follows from [54]. Second, Fig. 19a shows that the flux density of a refracted RF pulse does not stay constant but increases at larger inclination angles. For example, the intensity of radio emission for $k = 10$ (≈ 500 MHz) and $\Delta\theta = 0$ (i.e., for a horizontal shower) is weaker by a factor of approximately 10 than for the angle $\Delta\theta = 17^\circ$. At low frequencies ($k = 3$), this ratio is only ~ 3. For horizontal showers, $k = 10$ and $k = 3$, the intensities of the emerging radiation fluxes are almost the same.

This behavior is also partly understandable in terms of geometrical optics. In Figure 20, diagrams of spatial distribution of radiation are plotted in different scales for $k = 10$ in three situations: curve *1* corresponds to $\Delta\theta = 0^\circ$, $\Delta\varphi_{1/2} = 18^\circ$ (for the half-width of the diagram); curve *2* to $\Delta\theta = 17^\circ$, $\Delta\varphi_{1/2} = 10^\circ$; and curve *3* (uniform medium, $n = 1.7$) to $\Delta\varphi_{1/2} = 7^\circ$. The results presented here were obtained for showers with $\alpha = 33$ ($E_0 = 10^{22}$ eV), $z_0 = 0.14$ m, $\rho_1 = 0.06$ m, $r = 100$ m, and $D = 3$. Considerable broadening (and hence decreased flux density) of the transmitted RF pulse seems to be connected with the strong dependence $d\psi_{\rm r}/d\psi_{\rm i} = n_1 \cos\psi_{\rm r}/(n_2 \cos\psi_{\rm i})$ of the refraction angle $\psi_{\rm r}$ on the incidence angle $\psi_{\rm i}$ in the range $\psi \approx \pi/2$.

No dependence of parameters on the shower depth z_1 was found in the range $0 < z_1 < 5$. This was not checked at greater depths, $z_1 > 5$, because such testing would only be meaningful if the distance r from the shower to the observer were increased simultaneously. Furthermore, it is clear from general arguments that if such a dependence existed, it would have to manifest itself for $z_1 \leqslant \lambda$. In this case, the wavelength falls within this range.

II. $\theta = \pi/2 - \Delta\theta$. In this case, the cascade shower can be caused by a heavy strongly interacting particle (such as a proton) after it crosses the interface in the vacuum-to-regolith direction. Obviously, the angle $\Delta\theta$ should be such that the cascade disk (of the radius 5–6 cm) could fully develop in the

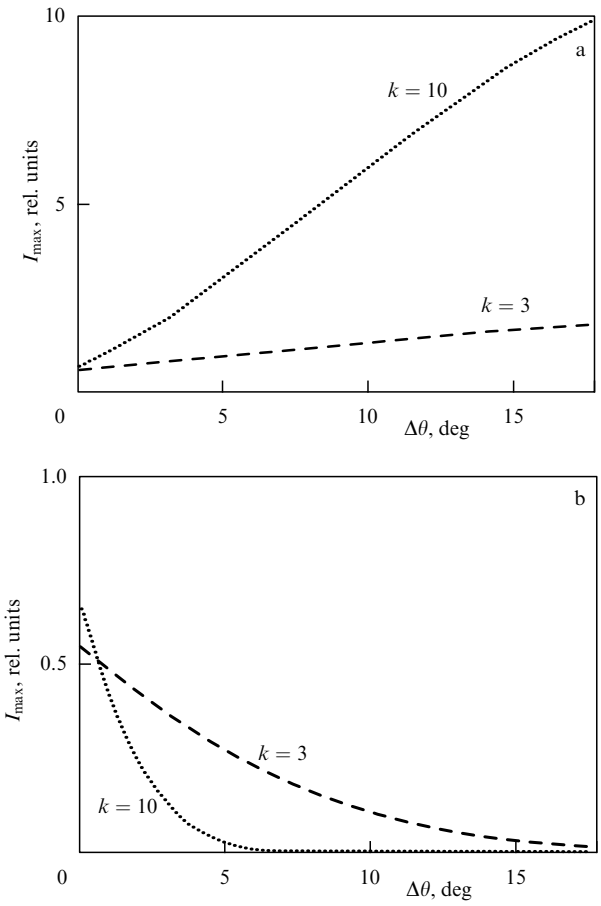

Figure 19. Maximum density of the radiation field as a function of the angle $\Delta\theta$: the shower propagating (a) in the regolith-to-vacuum direction and (b) in the vacuum-to-regolith direction. $\Delta\theta$ is the angle between the horizon and the direction of motion of the disk. All curves were plotted in the same scale.

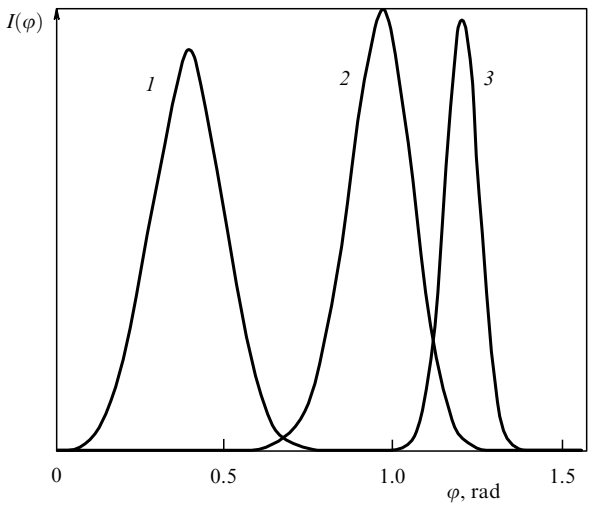

Figure 20. Curves *1* and *2* are plots of the radiation intensity distribution in the plane (x, z) for the respective inclination angles $\theta = \pi/2$ and $\theta = \pi/2 + 0.3$. Curve *3* is the intensity distribution in the emission field in a uniform medium with $n = 1.7$. The curves are plotted in different scales.

medium. Because a shower in the lunar regolith reaches a maximum after covering a path at least 4–5 m long, this condition is satisfied already at an angle $\Delta\theta \approx 1^\circ$, i.e., the disk does not 'reach' into the vacuum. Figure 19b shows maximum values of the flux density in refracted radiation for showers whose direction corresponds to the selected angles $\pi/2 - \Delta\theta$ plotted on the same scale (the same as in Fig. 19a).

Obviously, low frequencies are much preferable in this case for measuring particle fluxes because the detector has a bigger aperture for observations in this mode accompanied by a relatively small decrease in the amplitude.

Because the energy of an RF pulse is proportional to the shower energy squared, we can expect the 100–200 MHz frequency window to be the most promising as regards measuring UHE particle fluxes. Clearly, the insufficient power of the radio signal needs to be compensated for by increasing the effective area of the antenna. Projects of large antennas are being discussed at the moment, and some such facilities will start operations in the not so distant future, e.g., the LOFAR radio telescope for astronomical observation at low radio frequencies, 10–240 MHz. When the work of constructing LOFAR is completed, its effective area will be about 1 km^2 [124]. LOFAR will be the largest telescope until 2017, when the SKA radio telescope is planned for completion; its working frequency range will be from 100 MHz to 25 GHz and the effective area will be greater than 1 km^2 (see, e.g., [125]).

13. Conclusion. Sources and prospects of the radioastronomical method

Because the reader has already been introduced in Sections 1–12 to the basic ideas and results of measurements of UHE particle flux using radio telescopes, it can be useful to briefly recall the early history of this technique and its prospects. This section cites facts without which this review would be incomplete. First, we need to mention the studies preceding the development of the radioastronomical method. We refer here to the RAMAND (Radio Antarctic Muon And Neutrino Detection) project whose main features have already been published [34], and the ANITA (Antarctic Impulsive Transient Antenna) project, a direct descendant of RAMAND. Currently, the ANITA experiment has already obtained some results that are stimulating further work on the project. Furthermore, it must be pointed out that the currently discussed possibility of placing a radio detector in space is also a direct consequence of the results of research employing radioastronomical techniques; it seems that we may witness the realization of this project in the nearest future.

13.1 RAMAND and ANITA projects

Askaryan's work [24, 25] stimulated an intense research effort aimed at implementing the idea of a new type of detector of UHE cosmic rays. Theoretical estimates showed that excess electrons of EAS radiate coherently in the radio band up to 50 MHz. In accordance with the shower energy estimates in [24, 25], the power of a Cherenkov RF pulse is sufficient for detection with the simplest antennas.

The first experimental projects whose results were published in 1965 can be regarded as launching intense activities aimed at building experimental foundations of the emission mechanism and clarifying the feasibility of designing an effective radio detector. By approximately 1980, the inflow of research papers thinned out considerably because it became obvious by that time that in the energy range $10^{18} - 10^{19}$ eV, a new-type detector as such cannot compete with traditional methods of detecting EAS (i.e., with EAS facilities).

Attempts to realize Askaryan's idea persist, despite a certain disappointment of the 1970s–1980s. However, the direction of attack changed significantly. Some of the results showed that a radio detector of this type can successfully complement the existing UHE particle detectors. This started a new round of exploring the potential of combining surface and fluorescent particle detectors. For example, projects and experiments like CASA-MIA (Chicago Air Shower Array-Michigan Anti array) [126,127], LOPES (LOFAR PrototypE Station) [128–133], CODALEMA (COsmic ray Detection Array with Logarithmic ElectroMag-netic Antennas) [134–139], the Tian Shan experiment TREND (Tian Shan Radio Experiment for Neutrino Detection) [140–144], experiments at the Pierre Auger Observatory and AERA Project (Auger Engineering Radio Array) [145, 146], and CROME (Cosmic-Ray Observation via Microwave Emission) [147, 148] can be classified as efforts of this type. This trend became possible owing to a breakthrough in the development of electronic systems capable of fast and reliable processing of information flowing from a large antenna array.

However, the most striking embodiment of Askaryan's ideas was the RAMAND project proposed by V A Gusev, I M Zheleznykh, and M A Markov (RAS Institute for Nuclear Research). In RAMAND, the vast body of Antarctic ice was to play the role of a giant target [34]. The project of this radio detector with a volume of $10^9 - 10^{11}$ m^3 was based on the argument that the measured absorption of radio waves in ice in the frequency range $10^7 - 3 \times 10^9$ Hz is of the order of $(4-12) \times 10^{-3}$ dB m^{-1} [149]. This quantity is so minuscule that there seems to be a chance to record Cherenkov RF pulses arriving from a depth of up to 1 km using antennas placed on the surface of ice. For reliable detection of RF pulses, the neutrino energy had to be at least $10^{17} - 10^{18}$ eV. The idea of the project is as follows.

According to [24], the charge excess q in a shower amounts to $\sim 10\%$ of the total number of electrons and positrons, and therefore the total energy of the Vavilov–Cherenkov radiation in the frequency band $\Delta\omega$ can be written as

$$E = \frac{q^2}{c^2}\,\omega\Delta\omega l\left(1 - \frac{1}{\beta^2}\,n^2\right),$$

where n is the refractive index of ice and l is the distance traveled by the shower. For the characteristic values $\omega = 2\pi \times 10^9$ s^{-1}, $\Delta\omega = 0.1\omega$, and $l = 200$ cm, the energy of emission is $E = 3 \times (10^{-10} - 10^{-4})$ erg for the shower energy $10^{13} - 10^{16}$ eV. Radiation would pass through the annular region formed by the Cherenkov cone on the surface of the ice sheet. The area of this region depends on the depth at which the cascade was formed. Further evaluation led the authors of [34] to the conclusion that if antennas with an effective area of a few square meters and frequency bandwidth of more than 100 MHz each are placed every 100–200 m in an area of 3×3 km^2, then the effective volume of the detector for frequencies of the order of 1 GHz would be $\sim 10^{10}$ m^3.

A radio signal propagating upward from a cascade at a depth up to 1 km is to be received on the surface by antennas placed in the region of the Cherenkov cone. The authors of the project expected that detectors of this kind would allow

searching for nonextended sources of UHE neutrinos of galactic and extragalactic origin. Unfortunately, the economic and political instability of the 1990s prevented implementation of this project in Russia, and the scientific community gave this work the appreciation it deserved only 15–20 years later.

The NASA project ANITA is a natural extension of the idea behind RAMAND. This project differs from RAMAND in that the antennas designed to detect RF pulses are lifted to the altitude of 35–37 km with a specially designed balloon (see, e.g., [150]). The target volume is greatly increased by this modification while retaining a relatively small number of antennas. This modernization of the RAMAND idea inevitably led not only to positive consequences but also to negative ones. For example, while the RAMAND antenna array can be excellently protected against atmospheric and anthropogenic noise, this can only be achieved to a certain extent (and probably not as reliably) in the ANITA project by using some digital analysis of signals. However, on the whole, ANITA is a step forward on the way to detection of cosmic rays by radio techniques. Because the RAMAND and ANITA projects are not too different from the radioastronomical method of detection, it seems advisable to describe the ANITA project in more detail, all the more so as the data accumulated by now encourage further development of this method.

The ANITA detector is mounted aboard a balloon launched near McMurdo Station in Antarctica. A stratospheric vortex forces the balloon to circle the South Pole at an altitude of 35–37 km, scanning the ice surface of the order of 1.5×10^6 km^2. During the flight, ANITA records all nanosecond RF pulses in the frequency range 200–1200 MHz. The detection threshold is constrained by the intensity, ~ 10 nW, of the thermal radiation from the surface of the ice. The task assigned to ANITA was to discover linearly polarized Cherenkov RF pulses emitted from a cascade of UHE neutrinos in the ice shield of the continent. The characteristic target volume at a cascade depth of 0.5 km and observation altitude 37 km would be 0.7×10^6 km^3. With the neutrino energy 5×10^{18} eV, the cascade energy should be about 10^{18} eV. At this energy, the neutrino cross section reaches a value for which the length of flight in Earth's crust is on average 300 km. The mean cross section of neutrinos chosen for this evaluation at this energy, $\sigma_\nu = 0.34 \times 10^{-31}$ cm^2 (per nucleon), yields the upper bound on the flux (over 10 days of observation) equal to 2×10^{17} cm^{-2} s^{-1} sr^{-1}. This is comparable to the theoretically predicted flux for the energy 5×10^{18} eV.

The main tool of the ANITA experiment is an array of broadband horn antennas with the frequency range 0.2–1.2 GHz. The radiation pattern of one such antenna has the angular width 60° and a gain of about 9 dB at the frequency 300 MHz, and its gain is practically constant in the entire frequency range. The first antenna array, mounted in the upper part of the balloon, is cylindrically symmetric with a scanning angle of 2π; the array is composed of two levels of eight antennas in each. The antenna 'beams' intersect one another and overlap to create excess 'illuminance' in the horizontal plane. The second array consists of 16 antennas mounted in the lower part of the payload space of the balloon; it was designed for measuring the time delay due to the path difference from the source to these arrays. The value of this delay is necessary for determining the axial angle to the emission source. The absolute orientation of the azimuthal plane is set using solar sensors and the tilt of the entire container is measured using GPS. The signal from each antenna is split into two signals from the left and right circular polarizations, each of which is shared among four frequency channels and is then digitized. The digitized signals are stored in the buffer for 20 μs and are then forwarded to the trigger logic unit. Each time the trigger conditions are satisfied, the corresponding data is extracted from the buffer and stored, and is then sent to a station on the ground for further analysis.

The main requirements for the data sent for storage are for the RF pulse to be visible (1) by several antennas with overlapping fields of view; (2) in most frequency channels; (3) in both polarizations; and (4) simultaneously by all antennas. Triggering is blocked if a pulse is present in the antennas whose fields of view do not overlap. These requirements should reduce the rate of signal detection to ~ 1 event every several minutes.

NASA scheduled the launching of the balloon with full-scale ANITA detector for 2006. However, a trial flight was flown to obtain a complete picture of the operating conditions of detector units and other systems: the prototype ANITA-lite was launched on 18 December, 2003 and spent 18.4 days in flight, of which 10 days were over Antarctic ice [151]. The ANITA-lite detection unit recorded $\approx 113{,}000$ events at an average 'live' observation time of 40% of the total flight time. Of these events, ≈ 87.500 proved to be triple coincidences. The ANITA Collaboration conducted two independent analyses aimed at searching for pulses of about 10 ns duration. Among the signals selected for the final analysis, no RF pulses of neutrino origin were identified. The authors of [151] used the method developed in [69] to calculate model-independent bounds on the neutrino flux at a 90% confidence level. In some cases, these results improved earlier measurements, and, in particular, they eliminated the long-standing model of Z-bursts.

The next round of exploration using the ANITA-1 detector began on 15 December, 2006. The balloon with all equipment flew up close to the McMurdo Station and made three circumpolar flights over Antarctica [152]. The flight lasted 35 days and landed at a distance of 300 miles from the Amundsen–Scott station. Anomalous stratospheric conditions resulted in misalignment of the polar vortex, and hence the detector of ANITA-1 spent most of the time over the western region of Antarctica, where the ice sheet is smaller and thinner. Furthermore, two powerful radio transmitters in Antarctica, at McMurdo and Amundsen–Scott, happened to be in the horizontal field of view, such that the detector was exposed to electromagnetic interference at a high signal level. Nevertheless, the on-board electronics worked in the 'live' mode for 17.3 days at the altitude of 35–37 km above sea level. The total volume of the ice target was estimated as $\sim 1.6 \times 10^6$ km^3.

The detector of ANITA-1 is a system consisting of 32 four-rib horn antennas with linear polarization, each of which has a field of view of 50° and the working frequency range 200–1200 MHz [153]. The antennas of the detector, located in the upper and lower rings of the load-bearing container, were installed at the azimuthal interval of 22.5°, and the radiation patterns of all the antennas were tilted by 10° below the horizon in order to increase the sensitivity to the part of the volume that lies below the horizon. The total field of view of all the antennas covers the entire lower hemisphere down to the nadir. RF pulses (exceeding the ambient thermal

noise by about 5σ) received by at least four antennas of both the upper and lower rings were recorded and digitized for further analysis. The authors of [152] announced that they were unable to find any RF pulses that satisfied all the requirements built into the selection program (see above).

Using this result and the known exposure, they calculated the upper bound on the flux of neutrinos of all types: $E_\nu^2 F \leqslant 2 \times 10^{-7}$ GeV $\mathrm{m}^{-2}\,\mathrm{s}^{-1}\,\mathrm{sr}^{-1}$ for the energy range $10^{18.5} \leqslant E_\nu \leqslant 10^{23.5}$ eV. In addition, we read in [152] that among the analyzed pulses, there were six that revealed horizontal polarization and which could be classified by virtue of a number of attributes as generated in extensive air showers.

The second series of measurements with the ANITA detector (ANITA-II) began on 21 December 2008 and ended in January 2009. The detector was airborne for 31 days, of which 28.5 were 'live' time [154]. This flight was more efficient than the first. After elimination of thermal-noise pulses from the data, there were still 320,722 events, and only five of them had attributes of the expected signals. Two events were found in the channel with vertical polarization (Vpol) and three events in the channel with horizontal polarization (Hpol). RF pulses from the Hpol channel showed characteristic signs that allowed the authors of [154] to identify these events as caused by EAS with a geosynchrotron mechanism of radio emission. The origin of the two events with vertical polarization could not be established. A reconstruction of the arrival directions shows that these are two isolated events. The upper bound on the maximum flux of UHE neutrinos was practically the same in this series of measurements as the limits calculated for the ANITA-I experiment. Further analysis of the recorded data [155] showed that the number of events traceable to EAS was six, and a more sensitive analysis increased the number of such showers to 16 [156].

These events are randomly distributed around ANITA's flight path; they are not spatially correlated with the locations of the sources of anthropogenic noise, but they have identical profiles of radio pulses and frequency spectra. In each case, the measured polarization planes were found to be perpendicular to the local geomagnetic field, as was expected for synchrotron radiation. The reconstruction of the arrival directions of RF pulses corresponds, with two exceptions, to events on the ice surface. Satellites on orbits around Earth are eliminated in this case as potential sources of nanosecond pulses, because the observation of RF pulses that passed through the ionosphere is impossible without special anti-dispersion filters. The phase of the 14 events localized below the horizon is rotated by 180° in comparison with the phase of the two events above the horizon, which was indeed anticipated under the mirror reflection. The mean energy of these events, estimated to be $(1.5 \pm 0.4) \times 10^{19}$ eV, reaches the GZK threshold. The obtained data and semi-empirical calculations were used to calculate the observation angle relative to the true shower axis, namely $1.5^\circ \pm 0.5^\circ$. This angular accuracy is comparable to the accuracy of observations made by ground-based observatories.

The data obtained during the ANITA experiments allow drawing additional conclusions. Results of an extended search for RF pulses caused by the interaction of ultrarelativistic magnetic monopoles with Antarctic ice are presented in [157]. The fact that no such events were identified during 31 days of observation can be interpreted as a weak diffuse flux no stronger than 10^{-19} $(\mathrm{cm}^2\ \mathrm{s}\ \mathrm{sr})^{-1}$. This is a stronger estimate than those obtained for the energy range with the Lorentz factor $\gamma > 10^{10}$.

13.2 Lunar Orbital Radio Wave Detector (LORD) project

The factor that makes the method of detection of UHE particles using radio telescopes so attractive is the possibility of increasing the working area of the detector by many orders of magnitude. The Moon was regarded as a suitable target for the interaction of cosmic rays with matter, because the area of the visible lunar surface is close to 10^7 km^2. However, as noted above, attempts to identify RF pulses emitted from a cascade beneath the lunar surface were unsuccessful. It was natural to assume that this was due first of all to the remoteness of the Moon from the radio telescope and to the inability to identify the signal against the background of dominating radio noise of terrestrial origin. It was this factor that provided impetus for the idea of placing the detector as an artificial satellite on a lunar orbit. Therefore, any discussion of problems connected with the radioastronomical method should at least briefly touch on the results achieved in this field.

The radioastronomical method of detection of UHE cosmic rays can be radically upgraded if the antenna and the radio receiver are placed in the immediate vicinity of the Moon. This idea, first suggested by Askaryan [24 25], was elaborated in detail in Project LORD (Lunar Orbital Radio Detector) [158, 159]. To be quite fair, we need to mention that attempts to quantify the characteristics of the lunar detector were also made earlier [120, 160]. But the most complete and well-argumented estimates were presented in [158, 159]. The main advantage of the Moon as a target for cosmic rays lies first of all in its huge size. Furthermore, the very low intensity of radio noise of terrestrial origin, relative proximity to the source of RF pulses and, finally, lack of moisture in the top layer of the Moon are important additions to the initial list of favorable conditions which, taken together, cannot be recreated on Earth.

The main requirements that must be met for detection on the lunar orbit [158, 159] are as follows. Depending on the type and energy of cosmic particles, the altitude of the orbit is chosen in the range from 100 to 1000 km. Wide-angle antennas need to scan the lunar surface within the line of sight and record short (nanosecond) RF pulses. An important parameter of the detector is its aperture, which is determined in the end by the particle energy and observation time. A prescribed particle energy dictates the arrival angles and the surface area of that part of the Moon through which the particle travels and in which the cascade produced by the particle generates an RF pulse accessible for detection. Of course, detector aperture is also dependent on the radiation pattern of the antenna, on the selected observation frequency, and so on. To illustrate the potential of such a project, the authors of [158, 159] chose the observation frequency 0.5–1.0 GHz. Papers [158, 159] give calculated apertures for a number of values of the threshold field strength. For example, the total aperture for a cascade produced by a cosmic particle at high energies in the range $10^{21} - 10^{23}$ eV increases to values of the order of $10^5 - 10^6$ km^2 sr.

If no events of lunar origin are found over a certain time interval of observations, this 'null result' would allow setting an upper bound for the particle flux as a function of energy. The values obtained in Project LORD for a model-independent upper bound on the differential neutrino flux over the observation interval of one year will be much lower than the

limits established in earlier experiments. According to the estimates in [158], the rate of registration of the number of events due to cosmic rays and neutrinos in the model of Z-bursts should be of the order of 10^5-10^6 particles per year for an orbit at an altitude of 1000 km.

An updated version of Project LORD is discussed in [159]. The authors suggest a version of a light antenna with a large effective area based on the available technology of thin-film 'solar sail' space structures (LORD-10). An analysis shows that to increase the scannable area of the lunar surface, it is necessary to use a multibeam parabolic antenna about 10 m in diameter with several radiators. At observation frequencies of several hundred MHz, such a reflector will form a narrow radiation pattern with an angular width of the order of $3^\circ-4^\circ$ for each radiator. This antenna array should provide a high gain and large field of view of the lunar surface, as well as a high signal-to-noise ratio. The authors of [159] evaluated the product of the detector aperture and the exposure time, which is the most information-rich characteristic of the experiment. The data given in [159] implies that, assuming a two-year observation period, the capabilities of the LORD-10 experiment are at the level of the most advanced projects — ANITA, SALSA (SALt-dome Shower Array), and Auger, while the potential of the full-scale version of LORD [158] would be greatly superior.

References

1. Kulikov G V, Khristiansen G B *Zh. Eksp. Teor. Fiz.* **35** 635 (1958) [*Sov. Phys. JETP* **8** 441 (1959)]
2. Linsley J *Phys. Rev. Lett.* **10** 146 (1963)
3. Baltrusaitis R M et al. (Fly's Eye Collab.) *Nucl. Instrum. Meth. Phys. Res. A* **240** 410 (1985)
4. Linsley J, in *Extensive Air Showers. Proc. from the 8th Intern. Cosmic Ray Conf.* (1963) p. 77
5. Bird D J et al. (Fly's Eye Collab.) *Phys. Rev. Lett.* **71** 3401 (1993)
6. Ginzburg V L *Usp. Fiz. Nauk* **163** (7) 45 (1993) [*Phys. Usp.* **36** 587 (1993)]
7. Ginzburg V L *Usp. Fiz. Nauk* **166** 169 (1996) [*Phys. Usp.* **39** 155 (1997)]
8. Greisen K *Phys. Rev. Lett.* **16** 748 (1966)
9. Abbasi R U et al. (High Resolution Fly's Eye Collab.) *Phys. Rev. Lett.* **92** 151101 (2004); astro-ph/0208243
10. Abbasi R U et al. (High Resolution Fly s Eye Collab.) *Phys. Rev. Lett.* **100** 101101 (2008); astro-ph/0703099
11. Tsarev V A *Fiz. Elem. Chast. At. Yad.* **35** 186 (2004) [*Phys. Part. Nucl.* **35** 112 (2004)]
12. Gusev G A et al. *Kosmich. Issled.* **44** 22 (2006) [*Cosmic Res.* **44** 19 (2006)]
13. Ryabov V A, Tsarev V A, Tskhovrebov A M *Usp. Fiz. Nauk* **178** 1129 (2008) [*Phys. Usp.* **51** 1091 (2008)]
14. Bednyakov V A *Fiz. Elem. Chast. At. Yad.* **33** 1146 (2002) [*Phys. Part. Nucl.* **33** 583 (2002)]
15. Gangui A, astro-ph/0110285
16. Stanev T, astro-ph/0411113
17. Abraham J et al. (AUGER Collab.) *Nucl. Instrum. Meth. Phys. Res. A* **523** 50 (2004)
18. Abraham J et al. (The Pierre Auger Collab.) *Phys. Rev. Lett.* **101** 061101 (2008); arXiv:0806.4302
19. The Pierre Auger Collab. *Science* **318** 938 (2007); arXiv:0711.2256
20. Véron-Cetty M-P, Véron P *Astron. Astrophys* **455** 773 (2006)
21. Stecker F W et al. *Nucl. Phys. B Proc. Suppl.* **136** 433 (2004); astro-ph/0408162
22. Olinto A V et al., arXiv:0903.0205
23. Cronin J W, Gaisser T K, Swordy S P *Sci. Am.* **276** (1) 44 (1997)
24. Askar'yan G A *Zh. Eksp. Teor. Fiz.* **41** 616 (1961) [*Sov. Phys. JETP* **14** 441 (1962)]
25. Askar'yan G A *Zh. Eksp. Teor. Fiz.* **48** 988 (1965) [*Sov. Phys. JETP* **21** 658 (1965)]
26. Kahn F D, Lerche I *Proc. R. Soc. London A* **289** 206 (1966)
27. Jelley J V et al. *Nature* **205** 327 (1965)
28. Atrashkevich V B et al. *Yad. Fiz.* **28** 712 (1978)
29. Golubnichii P I, Filonenko A D *Pis'ma Zh. Tekh. Fiz.* **20** (23) 59 (1994) [*Tech. Phys. Lett.* **20** 960 (1994)]
30. Golubnichii P I, Filonenko A D *Pis'ma Zh. Tekh. Fiz.* **20** (12) 57 (1994) [*Tech. Phys. Lett.* **20** 499 (1994)]
31. Stanev T et al. *Phys. Rev. D* **25** 1291 (1982)
32. Filonenko A D, Chekh Yu N *Radiofiz. Radioastron.* **7** (2) 160 (2002)
33. Filonenko A D *Usp. Fiz. Nauk* **172** 439 (2002) [*Phys. Usp.* **42** 403 (2002)]
34. Gusev G A, Zheleznykh I M *Pis'ma Zh. Eksp. Teor. Fiz.* **38** 505 (1983) [*JETP Lett.* **38** 611 (1983)]
35. Dagkesamanskii R D, Zheleznykh I M *Pis'ma Zh. Eksp. Teor. Fiz.* **50** 233 (1989) [*JETP Lett.* **50** 259 (1989)]
36. Olhoeft G R, Strangway D W *Earth Planet. Sci. Lett.* **24** 394 (1975)
37. Alvarez-Muñiz J et al. *Phys. Rev. D* **74** 023007 (2006); astro-ph/0512337
38. Hankins T H, Ekers R D, O'Sullivan J D *Mon. Not. R. Astron. Soc.* **283** 1027 (1996)
39. Gorham P W, Liewer K M, Naudet C J, Technical Report (Pasadena, Calif.: Jet Propulsion Lab., California Inst. of Tech., 2000); astro-ph/9906504
40. Gorham P W et al., astro-ph/0102435
41. Gorham P W J et al. *Phys. Rev. Lett.* **93** 041101 (2004); astro-ph/0310232
42. Abranin E P et al. *Izv. Ross. Akad. Nauk. Fiz.* **65** 1670 (2001) [*Bull. Russ. Acad. Sci. Phys.* **65** 1818 (2001)]
43. Beresnyak A R et al. *Astron. Zh.* **82** 149 (2005) [*Astron. Rep.* **49** 127 (2005)]
44. Scholten O et al. *Nucl. Instrum. Meth. Phys. Res. A* **604** S102 (2009); arXiv:0810.3426
45. Buitink S et al., arXiv:0808.1878
46. Scholten O et al. *Phys. Rev. Lett.* **103** 191301 (2009); arXiv: 0910.4745
47. Gandhi R et al. *Phys. Rev. D* **58** 093009 (1998)
48. Filonenko A D *Zh. Eksp. Teor. Fiz.* **141** 447 (2012) [*JETP* **114** 392 (2012)]
49. Filonenko A D *Pis'ma Zh. Eksp. Teor. Fiz.* **91** 483 (2010) [*JETP Lett.* **91** 437 (2010)]
50. Mitsui K *Phys. Rev. D* **45** 3051 (1992)
51. Bugaev E V, Shlepin Yu V *Phys. Rev. D* **67** 034027 (2003); hep-ph/0203096
52. Alvarez-Muñiz J, Zas E, astro-ph/9806098
53. Alvarez-Muñiz J, Zas E, in *New Worlds in Astroparticle Physics. Proc. of the Second Intern. Workshop, Faro, Portugal, 3–5 September, 1998* (Eds A M Mourão, M Pimenta, P Sá) (Singapore: World Sci. Publ., 1999) p. 159; astro-ph/9902187
54. Filonenko A D *Pis'ma Zh. Eksp. Teor. Fiz.* **86** 339 (2007) [*JETP Lett.* **86** 287 (2007)]
55. Filonenko A D, Filonenko V A *Pis'ma Zh. Tekh. Fiz.* **34** (4) 8 (2008) [*Tech. Phys. Lett.* **34** 139 (2008)]
56. Zas E, Halzen F, Stanev T *Phys. Rev. D* **45** 362 (1992)
57. Alvarez-Muñiz J, Zas E *Phys. Lett. B* **411** 218 (1997)
58. Alvarez-Muñiz J, Zas E, in *Proc. of the 26th Intern. Cosmic Ray Conf., August 17–25, 1999, Salt Lake City, Utah, USA*, Vol. 1 (Eds D Kieda, M Salamon, B Dingus) p. 506; astro-ph/9906347
59. Alvarez-Muñiz J, Zas E, astro-ph/9706064
60. Shibata Y et al. *Phys. Rev. A* **44** R3449 (1991)
61. Takahashi T et al. *Phys. Rev. E* **50** 4041 (1994)
62. Yoshida S et al. *Astrophys. J.* **479** 547 (1997)
63. Alvarez-Muniz J, Zas E *Proc. 25th ICRC* **7** 309 (1996)
64. Gorham P W et al. *Phys. Rev. E* **62** 8590 (2000)
65. Saltzberg D et al. *Phys. Rev. Lett.* **86** 2802 (2001); hep-ex/0011001
66. Gorham P W et al. *AIP Conf. Proc.* **579** 177 (2001)
67. Gandhi R *Nucl. Phys. B Proc. Suppl.* **91** 453 (2000); hep-ph/0011176
68. Kraus J D *Radio Astronomy* (New York: McGraw-Hill, 1966) [Translated into Russian (Moscow: Sov. Radio, 1973)]
69. Lehtinen N G, Gorham P W, astro-ph/0309656
70. Lehtinen N G, Gorham P W *Phys. Rev. D* **69** 013008 (2004)
71. Fargion D, Mele B, Salis A *Astrophys. J.* **517** 725 (1999); astro-ph/9710029
72. Weiler T J *Astropart. Phys.* **11** 303 (1999); hep-ph/9710431
73. Katz U F, Spiering Ch *Prog. Part. Nucl. Phys.* **67** 651 (2012); arXiv:1111.0507

74. Blanco-Pillado J J, Vázquez R A, Zas E *Phys. Rev. D* **61** 123003 (2000); astro-ph/9902266
75. Yoshida S, Sigl G, Lee S *Phys. Rev. Lett.* **81** 5505 (1998); hep-ph/9808324
76. Fodor Z, Katz S D, Ringwald A *JHEP* (06) 046 (2002); hep-ph/0203198
77. Kalashev O E et al. *Phys. Rev. D* **65** 103003 (2002); hep-ph/0112351
78. Kalashev O E et al. *Phys. Rev. D* **66** 063004 (2002); hep-ph/0205050
79. Domokos G, Kovesi-Domokos S, Mikulski P T, hep-ph/0006328
80. Gelmini G, Kusenko A *Phys. Rev. Lett.* **84** 1378 (2000)
81. Vilenkin A, Shellard E P S *Cosmic Strings and other Topological Defects* (Cambridge: Cambrige Univ. Press, 1994)
82. Golubnichii P I, Filonenko A D, Yakovlev V I *Izv. Ross. Akad. Nauk Fiz.* **58** (12) 115 (1994)
83. Golubnichii P I, Filonenko A D *Ukr. Fiz. Zh.* **41** 696 (1996)
84. Filonenko A D *Zh. Tekh. Fiz.* **78** (9) 120 (2008) [*Tech. Phys.* **53** 1222 (2008)]
85. Braude S Ya, Men' A V *Usp. Fiz. Nauk* **109** 769 (1973) [*Sov. Phys. Usp.* **16** 284 (1973)]
86. Filonenko A D *Izv. Ross. Akad. Nauk Fiz.* **61** 543 (1997) [*Bull. Russ. Acad. Sci. Phys.* **61** 428 (1997)]
87. Filonenko A D *Pis'ma Zh. Eksp. Teor. Fiz.* **70** 639 (1999) [*JETP Lett.* **70** 649 (1999)]
88. Ginzburg V L *Rasprostranenie Elektromagnitnykh Voln v Plazme* (The Propagation of Electromagnetic Waves in Plasmas) (Moscow: Fizmatgiz, 1960) [Translated into English (Oxford: Pergamon Press, 1964)]
89. Shklovskii I S *Kosmicheskoe Radioizluchenie* (Cosmic Radio Waves) (Moscow: Fizmatgiz, 1956) [Translated into English (Cambridge: Harvard Univ. Press, 1960)]
90. Kaplan S A, Pikelner S B *Fizika Mezhzvezdnoi Sredy* (Physics of the Interstellar Medium) (Moscow: Nauka, 1979)
91. Kikoin I K *Tablitsy Fizicheskikh Velichin* (Tables of Physical Quantities) (Moscow: Atomizdat, 1976)
92. Beresnyak A R, astro-ph/0310295
93. Yamamoto T et al. (the Pierre Auger Collab.), arXiv:0707.2638
94. Smida R (the Pierre Auger Collab.), arXiv:1109.4743
95. Scholten O et al., astro-ph/0508580
96. Scholten O et al., astro-ph/0609179
97. Verbiest J P W et al. *Class. Quantum Grav.* **27** 084015 (2010); arXiv:0912.2692
98. Karuppusamy R, Stappers B, van Straten W *Publ. Astron. Soc. Pacific* **120** 191 (2008); arXiv:0802.2245
99. Scholten O et al. *Astropart. Phys.* **26** 219 (2006)
100. Alvarez-Muñiz J, Zas E *Phys. Lett. B* **434** 396 (1998)
101. Buitink S et al. *Astron. Astrophys.* **521** A47 (2010); arXiv:1004.0274
102. Scholten O et al. *Phys. Rev. Lett.* **103** 191301 (2009)
103. Gorham P W et al. (ANITA Collab.) *Phys. Rev. Lett.* **103** 051103 (2009)
104. Bahcall J, Waxman E *Phys. Rev. D* **64** 023002 (2001)
105. Protheroe R J, Stanev T *Phys. Rev. Lett.* **77** 3708 (1996)
106. ter Veen S et al. *Phys. Rev. D* **82** 103014 (2010); arXiv:1010.6061
107. Frank I M *Izluchenie Vavilova – Cherenkova* (Vavilov – Cherenkov Radiation) (Moscow: Nauka, 1988)
108. Abraham J et al. (Pierre Auger Collab.) *Phys. Lett. B* **685** 239 (2010)
109. Jaeger T R, Mutel R L, Gayley K G *Astropart. Phys.* **34** 293 (2010); arXiv:0910.5949
110. Jaeger T R, PhD Thesis (Iowa City: Univ. of Iowa, 2010)
111. James C W, Protheroe R J *Astropart. Phys.* **31** 392 (2009)
112. James C W, Protheroe R J *Astropart. Phys.* **30** 318 (2009)
113. Gayley K G, Mutel R L, Jaeger T R *Astrophys. J.* **706** 1556 (2009); arXiv:0904.3389
114. Landau L D, Lifshitz E M *Teoriya Polya* (The Classical Theory of Fields) (Moscow: Fizmatgiz, 1962) [Translated into English (Oxford: Pergamon Press, 1971)]
115. Rossi B, Greisen K *Rev. Mod. Phys.* **13** 240 (1941) [Translated into Russian: *Vzaimodeistvie Kosmicheskikh Luchei s Veshchestvom* (Interaction of Cosmic Rays with Matter) (Moscow: IL, 1948)]
116. Hayakawa S *Cosmic Ray Physics* (New York: Wiley-Intersci., 1969) [Translated into Russian (Moscow: Mir, 1973)]
117. Belen'kii S Z *Lavinnye Protsessy v Kosmicheskikh Luchakh* (Avalanche Processes in Cosmic Rays) (Moscow: Gostekhizdat, 1948)
118. Filonenko A D *Pis'ma Zh. Eksp. Teor. Fiz.* **89** 445 (2009) [*JETP Lett.* **89** 381 (2009)]
119. Alvarez-Muñiz J, Vázquez R A, Zas E *Phys. Rev. D* **62** 063001 (2000); astro-ph/0003315
120. Stål O et al., astro-ph/0509210
121. Vinogradova M B, Rudenko O V, Sukhorukov A P *Teoriya Voln* (Theory of Waves) (Moscow: Nauka, 1979)
122. Katsenelenbaum B Z *Vysokochastotnaya Elektrodinamika* (High-frequency Electrodynamics) (Moscow: Nauka, 1966)
123. Brekhovskikh L M *Usp. Fiz. Nauk* **38** 1 (1949)
124. Garrett M A et al., arXiv:0902.2534
125. Lazio J, arXiv:0910.0632
126. Rosner J L, hep-ex/9508011
127. Rosner J L, Wilkerson J F, hep-ex/9702008
128. Petrovic J et al. (LOPES Collab.) *J. Phys. Conf. Ser.* **39** 471 (2006); astro-ph/0611225
129. Falcke H et al. *Nature* **435** 313 (2005)
130. Huege T, Ulrich R, Engel R *Astropart. Phys.* **30** 96 (2008)
131. Apel W D et al. *Astropart. Phys.* **32** 294 (2010)
132. Apel W D et al. (LOPES Collab.) *Astropart. Phys.* **26** 332 (2006)
133. Haungsa A et al. (LOPES Collab.), arXiv:0811.1919
134. Ravel O et al. *Nucl. Instrum. Meth. Phys. Res. A* **518** 213 (2004); astro-ph/0306255
135. Ardouin D et al. *Nucl. Instrum. Meth. Phys. Res. A* **572** 481 (2007)
136. Lebrun D, in *Proc. of the 30th Intern. Cosmic Ray Conf. July 3 – 11, 2007, Mérida, Yucatán, Mexico* Vol. 4 (Eds R Caballero et al.) (Mexico City, Mexico: Univ. Nacional Autonoma de Mexico, 2008) p. 187
137. Riviere C et al. (CODALEMA Collab.), arXiv:0906.2720
138. Revenu B (for the CODALEMA Collab.), arXiv:0906.2832
139. Bellétoile A (for the CODALEMA Collab.), arXiv:1109.3579
140. Ardouin D et al. *Astropart. Phys.* **34** 717 (2011); arXiv:1007.4359
141. Ardouin D et al. *Nucl. Instrum. Meth. Phys. Res. A* **604** S85 (2009)
142. Carloganu C et al., in *44th Rencontres de Moriond, La Thuile, Italy, 2009*
143. Lamblin J et al., in *Proc. of the 30th Intern. Cosmic Ray Conf. July 3 – 11, 2007, Mérida, Yucatán, Mexico* Vol. 5 (Eds R Caballero et al.) (Mexico City, Mexico: Univ. Nacional Autonoma de Mexico, 2008) p. 921
144. Ardouin D et al., arXiv:0902.0730
145. van den Berg A M (for the Pierre Auger Collab.), arXiv:0708.1709
146. Huege T (for the Pierre Auger Collab.), arXiv:0906.4970
147. Gorham P W et al. *Phys. Rev. D* **78** 032007 (2008)
148. Gorham P W et al., arXiv:0705.2589
149. Bogorodsky V V, Bentley C R, Gudmandsen P E *Radioglyatsiologiya* (Radioglaciology) (Leningrad: Gidrometeoizdat, 1983) [Translated into English (Dordrecht: D. Reidel Pub. Co., 1985)]
150. Silvestri A et al. (ANITA Collab.), in *Neutrinos and Explosive Events in the Universe. Proc. of the 14th Course of the Intern. School of Cosmic Rays Astrophysics, Erice, Italy, 2 – 13 July 2004* (NATO Science Ser. II Math., Phys. and Chem., Vol. 209, Eds M M Shapiro, S Todor, J P Wefel) (Dordrecht: Springer, 2005) p. 297; astro-ph/0411007
151. Barwick S W et al. (ANITA Collab.) *Phys. Rev. Lett.* **96** 171101 (2006); astro-ph/0512265
152. Gorham P W et al. (ANITA Collab.), arXiv:0812.2715
153. Gorham P W et al. (ANITA Collab.) *Astropart. Phys.* **32** 10 (2009); arXiv:0812.1920
154. Gorham P W et al. (ANITA Collab.) *Phys. Rev. D* **82** 022004 (2010); arXiv:1003.2961
155. Gorham P W et al. (ANITA Collab.) *Phys. Rev. Lett.* **103** 051103 (2009)
156. Hoover S et al., arXiv:1005.0035
157. Detrixhe M et al. *Phys. Rev. D* **83** 023513 (2011); arXiv:1008.1282
158. Gusev G A et al. *Kosmich. Issled.* **44** 22 (2006) [*Cosmic Res.* **44** 19 (2006)]
159. Gusev G A et al. *Dokl. Ross. Akad. Nauk* **406** 327 (2006) [*Dokl. Phys.* **51** 22 (2006)]
160. Golubnichii P I, Filonenko A D *Kosmich. Nauka Tekhnol.* **5** (4) 87 (1999)